DOE Award Number EE0003134

Final Report

Institute for Sustainable Energy

Submitted By

Professor Ajay K Agrawal

Department of Mechanical Engineering
The University of Alabama, Tuscaloosa
Contact No.: 205-348-4964
Email: aagrawal@eng.ua.edu

Professor Paulius Puzinauskas
Department of Mechanical Engineering
The University of Alabama, Tuscaloosa

Professor Alan Lane
Department of Chemical and Biological Engineering
The University of Alabama, Tuscaloosa

October 31, 2014

Executive Summary

Alternate fuels offer unique challenges and opportunities as energy source for power generation, vehicular transportation, and industrial applications. Institute for Sustainable Energy (ISE) at UA conducts innovative research to utilize the complex mix of domestically-produced alternate fuels to achieve low-emissions, high energy-efficiency, and fuel-flexibility. ISE also provides educational and advancement opportunities to students and researchers in the energy field. Basic research probing the physics and chemistry of alternative fuels has generated practical concepts investigated in a burner and engine test platforms.

Research on Utilization of Alternative Fuels: Clean combustion of liquid biofuels was achieved (e.g., biodiesel and straight vegetable oil) by utilizing a novel fuel-injection concept relying upon aerodynamically created two-phase mixing near the injector tip. The performance of the fuel injector was characterized using high-speed imaging and time-resolved particle image velocimetry. Experiments were conducted with water as the baseline liquid and glycerol as the alternative fuel with extremely poor physical and chemical properties. Results show that the fuel injector is capable of atomizing both liquids and that much of the fuel breakup process occurs within the fuel injector. Combustion experiments in industrial scale burner were also conducted, and demonstrated clean and complete combustion over a range of flow conditions.

For automotive applications, we developed a novel combustion approach to shift the paradigm by dividing the complex engine flow and chemical processes into two steps: (1) an external step involving injection, atomization, and vaporization of liquid fuel(s), mixing of fuel and oxidizer, and subsequently, fuel reformation or partial oxidation to produce syngas fuel outside the engine cylinder, and (2) an internal step involving injection of syngas fuel into the engine cylinder containing ingested air, followed by low temperature combustion (LTC) based on homogeneously-charged compression ignition (HCCI) concept. A comprehensive computational fluid dynamics based models of the process was developed to predict the chemical processes and how they are affected by the fluid flow. An experiment to demonstrate the concept was designed and developed to demonstrate the feasibility of the concept.

Research has been conducted to develop and characterize key aspects of this concept including a fuel-flexible fuel reformer, a combustion-system flexible two-stroke research engine test platform, and procedures to isolate and coat catalysts on a porous bed for use inside the engine and fuel reformer to selectively increase the chemical activity.

Seminar Series and Technical Workshop: For outreach and education, a seminar series with distinguished speakers in the energy field was organized in Spring 2013 (speakers: Prof. Vigor Yang-Georgia Tech, Prof. A. Melis-UC Berkeley, Dr. M Razdan-Rolls Royce, Prof. M. Wooldridge-University of Michigan, Dr. A. Singhal-CFDRC, Prof. G Settles-Penn State University, Prof. D. Dunn-Rankin-UC Irvine, Dr. Mark Musculus – Sandia National Lab).

A workshop on Sustainable Fuels: Production and Combustion was held on July 29, 2014. Ten speakers from industry, government, and academia were invited to make the technical presentations. The information about the workshop was sent to universities in Alabama and the region, and to wider community through The Combustion Institute mail list. A website was created to participants to register for the workshop. A total of 75 people registered for the workshop. The workshop was very effective in bringing together researchers in the area. Participant organizations included: Southern Company, John Zink Hamworthy, Fives North America, CFD Research Corporation, Oak Ridge National Laboratory, US Department of

Agriculture, Auburn University, and Washington University. It covered fields of vehicular transportation, power generation, industrial transportation, and aviation.

Summary: Project has supported research of three engineering faculty members, one post-doctoral researcher, three graduate students, and two undergraduate students. The project resulted in seven conference papers, one doctoral dissertation, one MS thesis and three undergraduate honors research projects. Research has led to five external research proposals. It resulted in the creation of the Alabama Sustainable Energy Research Cluster, a new cluster-hire initiative in sustainable energy area at the University of Alabama.

Table of Contents

1.0 Task A: Research on Utilization of Alternative Fuels

1.1 Task A.1: Develop Experimental Database to Predict Emissions from Combustion Systems using Alternative Fuels (*Professor Ajay K. Agrawal*)

1.1.1 Overview

Under this task, research was conducted on three different but related topics, all relating to innovations and quantification of alternative fuel combustion. The key findings are summarized in this section, while complete publications are provided in the appendix.

1.1.2 Alternate Fuel Combustion

Alternate Fuel Combustor Operated on Glycerol and Methane (paper A.1 in Appendix A).

Disposal of glycerol, the byproduct from biodiesel production, is an emerging issue with the increasing interest in utilizing fuels produced from biomass. Glycerol and other industrial waste products with moderate amounts of stored chemical energy can be economically viable alternative fuels because of their low cost. Previous research has shown that glycerol is combustible, in spite of its high ignition temperature, by preheating the combustion zone with propane or methane. We have reported that glycerol with its extraordinarily high kinematic viscosity can still be finely atomized by the so-called flow blurring (FB) injector to produce clean flames with extremely low emissions at the combustor exit. In the present study, a fuel-flexible combustor with a FB injector is utilized to simultaneously burn liquid and gaseous fuels. Measurements of product gas temperature and CO and NO_x emissions are acquired at various axial and transverse locations inside a swirl-stabilized combustor to illustrate the flame structure. For a fixed heat release rate (HRR), methane and glycerol flow rates are varied to vary the percentages of HRR from each fuel and thus, the fuel mix. For a fixed fuel mix, the air-to-liquid mass ratio (ALR) through the injector is varied to investigate its effect on the flame structure. Results show low-emissions with combustion of glycerol without and with methane supply. The addition of methane improves glycerol combustion by improving fuel vaporization, fuel-air mixing, and fuel oxidation resulting in localized zones of higher product gas temperatures. CO emissions decrease and NO_x emissions increase when increasing the percentage of HRR from methane. Higher ALR improves atomization to form smaller droplets that vaporize rapidly and result in shorter primary reaction zone with higher local temperatures reducing CO emissions and increasing NO_x emissions. In spite of these differences, all fuel combinations result in complete combustion with extremely low CO and NO_x emissions at the combustor exit.

Measurements in a Combustor Operated on Alternative Liquid Fuels (paper A.2 in Appendix B)

Diminishing fossil fuel resources, ever-increasing energy cost, and the mounting concerns for environmental emissions have precipitated worldwide research on alternative fuels. Present study demonstrates low-emission combustion of diesel, biodiesel and straight vegetable oil (VO) is a dual-fuel burner employing flow blurring (FB) injector concept for fuel atomization. Measurements of temperature and CO and NOx emissions are acquired at various axial and radial locations within the combustor. A custom-designed thermocouple probe and a helium product gas sampling probe are employed to obtain the measurements. Infra-red images to depict combustor wall temperatures and visual flame images to demonstrated clean combustion are also presented. Results show that the FB injector ensured fine atomization of all three fuels irrespective of significant differences in their kinematic viscosity and surface tension properties.

1.1.3 Partial Thermal Oxidation of Fuel

Analysis of a Mesoscale Fuel Reformer with Heat Recirculation and Porous Surface Stabilized Flame (Paper A.3 in Appendix A)

Syngas, or synthetic gas, is composed primarily of hydrogen (H_2) and carbon monoxide (CO). Carbon monoxide and hydrogen store chemical energy, thus syngas can be used as a fuel source. Fuel reformation is the process used to convert an existing fuel source, such as methane or diesel, into synthetic gas. In this study, thermal partial oxidation is used for fuel reformation to eliminate the need for the catalyst. Thermal partial oxidation employs thermal energy to partially oxidize the fuel to produce syngas. The major drawback to this method of fuel reforming is the significant heat loss associated with the procedure. Further, fuel reforming at the mesoscale is difficult because of the short residence time available. In this study, a fuel reformer with a counterflow annular heat exchanger for heat recirculation and porous inert media to stabilize the flame is presented. These design features address the issue of major heat loss and make the process much more efficient. A detailed computational analysis is presented to evaluate design features and show thermal and combustion characteristics of the system. The analysis is based on conservation equations of mass, momentum, and species mass conservation in an axisymmetric domain. The computational analysis includes simulations under rich conditions at ambient pressure. Chemkin and Fluent software were integrated to simulate rich methane-air combustion at different equivalence ratios using a detailed chemical kinetic mechanism. Analysis reveals the effects of reactant inlet temperature and fuel reformer operating conditions on fuel to syngas conversion. Ultimately this study shows that thermal oxidation for fuel reforming can be a viable and efficient process.

Reforming Reactor System for Partial Oxidation and Autothermal Fuel Reforming (Paper A.4 in Appendix A)

A combustion system to reform long-chain hydrocarbons such as diesel or Jet-A fuel into syngas is presented. Heat recirculation concept based reactor is used to partially combust highly rich air-fuel mixture to yield product gas with very high CO and H_2 concentrations. Chemical equilibrium and perfectly stirred reactor models were used to simulate the rich combustion of n-heptane to obtain insight into CO and H_2 conversion efficiency at elevated temperatures (in excess of 1000°C) to sustain thermal partial oxidation. Experimental system developed uses preheated air, convective and conductive annular heat transfer, twin-fluid injectors, and porous inert media combustion to test the viability of partial oxidation reaction and autothermal fuel reforming without the use of a catalyst. The complete reforming reactor is 9.3 inches long and 4.6 inches in diameter. Preliminary experimentation on rich methane are carried out to demonstrate combustion at equivalence ratio of three indicating potential of the developed fuel reformer.

1.1.4 Quantitative Measurements in Non-reacting and Reacting Flows

Ultra High Speed Rainbow Schlieren Deflectometry for Statistical Description of Turbulent Low-Density Jets (Paper A.5 in Appendix A)

Rainbow schlieren deflectometry (RSD) integrated with ultra high-speed digital imaging system is used to characterize a turbulent low-density jet through statistical description of path-integrated measurements. Unlike deconvoluted measurements, statistics of deflectometric data are free from approximations and can be utilized as benchmark to compare and validate path-integrated quantities derived from large-eddy and/or direct numerical simulations. Deflectometry techniques allow non-intrusive measurements to probe difficult to access near-field region of the jet exit. The experimental system consists of a helium jet discharged vertically into ambient air from a round tube injector of 4 mm inside diameter (d) and jet exit Reynolds number of 4000. Rainbow schlieren apparatus was configured to cover the near-field axial range of 0 to 20d downstream of injector exit at pixel resolution of 124 μm, temporal resolution of 20 μs, and image acquisition rate of 50,000 frames per second to capture a wide range of turbulent structures. Deflectometric measurements are utilized to estimate integral length scales, integral time scales, and wavenumber spectra at different locations in the flow field. Results show characteristics of a developing turbulent flow in the axial direction with gradual establishment of order. Space-time cross-correlation functions show that the Taylor's hypothesis of frozen flow turbulence is strictly not applicable in the near-field. Two point cross-correlation functions in transverse direction represent high intensity fluctuations and possible noise source locations.

Ultra High-Speed Rainbow Schlieren Deflectometry For Turbulence Measurements in Jets and Flames (Paper A.6 in Appendix A)

Rainbow schlieren deflectometry (RSD) integrated with ultra high-speed imaging system is used to characterize turbulence in helium jet. The experimental system consists of a turbulent helium jet in air probed by rainbow schlieren deflectometry technique to acquire deflectometric data. Helium is discharged vertically into ambient air from a round tube injector of 3.65 mm diameter and jet inlet Reynolds number of 4000. Rainbow schlieren apparatus was configured to cover the near field axial range of 0 to 20 diameters downstream of injector exit at pixel resolution of 300 μm, image acquisition rate of 210,000 frames per second, and image exposure time of 4.7 μs to capture a wide range of turbulent structures. These deflectometric measurements are utilized along with spectral analysis algorithm (SAA) for reconstruction of statistics of local scalar field (helium mole fraction) and theoretical framework for cross-correlation based approach for velocity estimation is presented. Non-intrusive nature of RSD application allows probing the near field region of injector exit to characterize turbulence. Helium concentration statistics shows that flow mixing and energy cascading result into decreased gradients at downstream locations yielding lower peak mean and variance with increased radial extent. Ultra high-speed imaging integration with RSD looks interesting approach to gain critical velocity field information to complete statistical characterization of turbulence through scalar and velocity measurements.

1.2 Task A.2 Investigate Catalytic Partial Oxidation of Alternate Fuels (*Prof. Alan M. Lane*):

1.2.1 Overview

The role of the Lane group in the Department of Chemical Engineering was to develop a fuel-flexible Rh/γ-Al_2O_3 catalyst to produce a consistent feed of CO, H_2, and small hydrocarbons to an HCCI engine optimized for such a fuel. The partial oxidation reaction is

$$C_XH_YO_Z + O_2 + H_2O \rightarrow CO + H_2 + \text{small hydrocarbons}$$

While the engine was being modified, we investigated a promising catalyst originally invented in our laboratory for the selective oxidation of CO in a mixture with H_2 as a fuel cell feed.

A water-treatment technique was applied to a conventional Rh/γ-Al_2O_3 catalyst. Both standard and water-treated Rh/γ-Al_2O_3 catalysts were prepared and their catalytic performance was tested in the methane partial oxidation reaction. The results showed that the water-treated Rh/γ-Al_2O_3 catalyst shows higher CO selectivity and lower CO_2 selectivity between 300 and 600 ^oC, compared with standard-treated catalyst. The enhancement is attributed to the formation of well-dispersed smaller Rh nanoparticles.

We chose Rh-based catalyst because it has been well-investigated for this type of reaction and seem to be optimal. We chose methane as the fuel because it is relevant as an alternative to gasoline and diesel and because it tends to foul the catalyst less due to carbon deposition (coking) compared to higher hydrocarbons. A sample of catalyst is ready to be tested in the modified HCCI engine so that operation in the catalytic mode can be compared to the conventional mode.

1.2.2 Introduction

Production of synthesis gas (H_2 and CO gas mixture) by methane (CH_4) partial oxidation (MPO) is an important intermediate step in many existing energy conversion technologies, such as fuel cells and Fischer-Tropsch reaction [1-5]. Decreasing the reaction temperature and improving reaction efficiency has been a great challenge to researchers. One of the solutions is to develop high-efficiency catalysts. Our group in previous research [6-8] showed that treating a Pt/γ-Al_2O_3 catalyst at 500 ^oC in a humid reducing environment (H_2O/H_2) can significantly decrease the reaction temperature of catalytic CO preferential oxidation in H_2. This is due to the decreased particle size and increased stability of Pt and decreased CO chemisorption strength after this treatment. In subsequent research by others, a similar water-treatment technique for reducing reaction temperature was also investigated and confirmed [9,10].

In this work, we applied the same water-treatment to Rh/γ-Al_2O_3 catalysts and investigated its catalytic effects on the MPO reaction. The reaction products were analyzed by Mass Spectrometry (MS), and the catalyst morphology was characterized by Transmission Electron Microscopy (TEM). The results show that water-treated Rh/γ-Al_2O_3 catalyst can effectively decrease the size of Rh nanoparticles, and water-treated Rh/γ-Al_2O_3 catalyst shows higher CO selectivity and lower CO_2 selectivity in the temperature range of 300-600 ^oC.

1.2.3 Experiment

Catalyst preparation

Catalyst standard-treatment: 1 wt% Rh/γ-Al_2O_3 catalyst was prepared by the incipient wetness method. Alumina (γ-Al_2O_3, 150 m^2/g, acid type, ~0.25 mm, Alfa) was first calcined in

air at 500 ^{o}C for 2 hours to remove volatiles, and then impregnated using an aqueous solution of $Rh(NO_3)_2$ (Alfa). The catalyst was dried in a fume hood overnight, followed by calcining in air at 500 ^{o}C for 2 hours. The catalyst was finally reduced in H_2 at 500 ^{o}C for 2 hours, and cooled down with N_2 protection. This process is considered to be the standard-treatment of the catalyst, as shown in Fig. 1.

Catalyst water-treatment: Water treatment begins after the standard treatment of catalyst. The standard-treated catalyst (0.1 g) was wetted with 5 mL deionized (DI) water, and then reduced in H_2 for 1 hour at 500 ^{o}C with heating rate of 10 ^{o}C/min, and finally cooled down to room temperature with N_2 protection. This process is considered to be water treatment of the catalyst, as shown in Fig. 1.

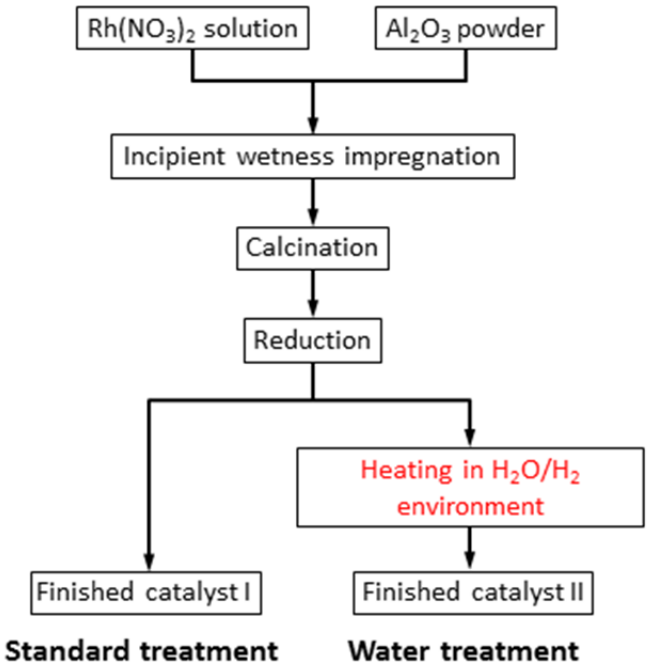

Fig.1. Rh/γ-Al_2O_3 catalyst preparation process: standard treatment and water treatment.

Catalyst testing and characterization

Figure 2 shows a schematic of MPO system for testing the above catalysts. A Hiden Catlab Microreactor with a vertical quartz tube (6 mm I.D.) was used for the reaction. The gas flow rates were controlled by mass flow controllers (MFC), and the reaction temperature was controlled by a programmable controller. The catalyst (0.1 g) was fixed inside the vertical reactor with quartz fibers. The gas flow rates of CH_4, O_2 and Ar were controlled to 40 ml/min, 20 ml/min and 20 ml/min, respectively. A mass spectrometer (Hiden QIC-20, MS) was used to analyze the reaction products, and Ar was used as an internal standard. A drier was located between reactor and MS to remove the water from the products, to prevent plugging of the MS capillary tube by water. The test conditions were between room temperature and 800 ^{o}C at 1 atm, and data was collected every 50 ^{o}C from 300 ^{o}C to 800 ^{o}C, as the initiation temperature of MPO with a Rh/γ-Al_2O_3 catalyst is around 275 ^{o}C [11].

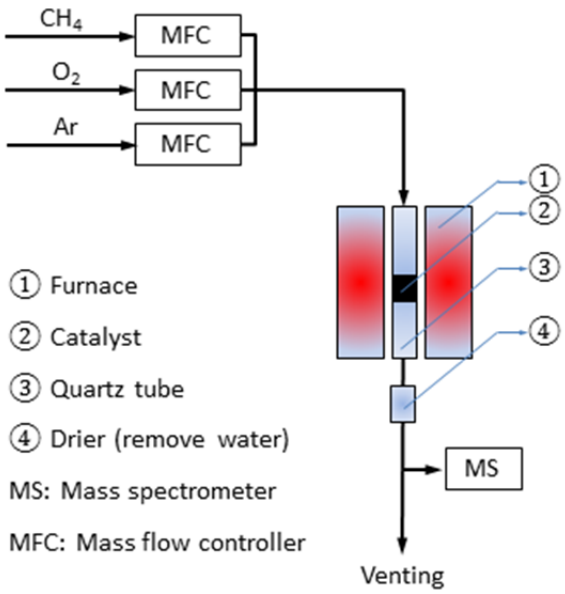

Fig. 2. A schematic of methane partial oxidation system.

The conversion of CH_4 and the selectivity of CO and CO_2 were calculated using the following formulas:

$$CH_4\ Conversion: \frac{CO_{out}+CO_{2\ out}}{CO_{out}+CO_{2\ out}+CH_{4\ out}} \quad (1)$$

$$CO\ Selectivity: \frac{CO_{out}}{CO_{out}+CO_{2\ out}+CH_{4\ out}} \quad (2)$$

$$CO_2\ Selectivity: \frac{CO_{2out}}{CO_{out}+CO_{2\ out}+CH_{4\ out}} \quad (3)$$

Transmission Electron Microscopy (TECHNAI FEI 20, TEM) was used to characterize the size and morphology of the catalysts. Each catalyst was ground in a mortar for 5 min, and then dispersed in methane with ultrasonication. The dispersion was dropped onto a copper TEM grid with a carbon substrate, and then dried for TEM characterization.

1.2.4 Results and discussion

Figure 3 shows the CH_4 conversion, CO and CO_2 selectivity of standard-treated ("S") and water-treated ("W") Rh/γ-Al_2O_3 catalysts in the MPO reaction. CH_4 conversion under both catalysts is similar in the temperature range of 300 - 600 ^oC. However, water-treated catalyst shows higher CO selectivity and lower CO_2 selectivity than standard-treated catalyst between 300 and 600 ^oC. The selectivity of CO and CO_2 under both catalysts becomes similar when the temperature is higher than 600 ^oC. This can be attributed to the MPO reaction reaching the thermodynamic equilibrium, and catalysts cannot change the reaction behavior.

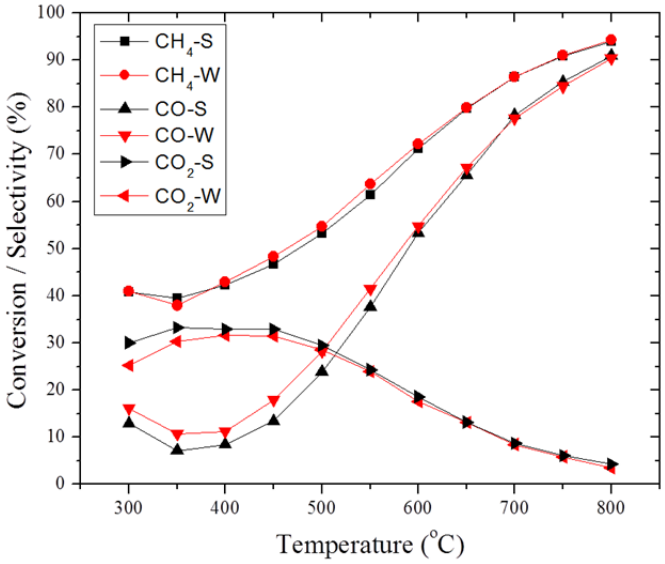

Fig. 3. The CH_4 conversion, CO and CO_2 selectivity of standard-treate d and water-treated 1 wt% Rh/γ-Al_2O_3 catalyts in methane partial oxidation reaction (S: standard-treated catalyst, W: water-treated catalyst).

The TEM images of standard-treated and water-treated catalysts are shown in Fig. 4a and Fig. 5a. The dark parts are Rh nanoparticles, and the brighter parts are γ-Al_2O_3 particles, as Rh has higher electron density than Al because of larger atomic number. The average size of the Rh nanoparticles in the water-treated catalyst is 4.7 nm (Fig. 5b), much smaller than that in standard-treated catalyst of 8.1 nm (Fig. 4b).

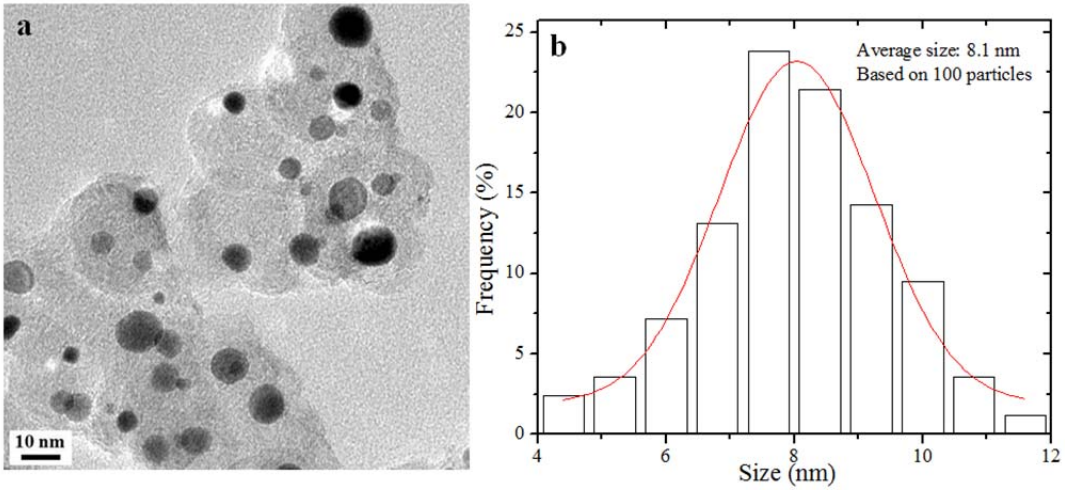

Fig. 4. Standard-treated 1 wt% Rh/γ-Al_2O_3 catalyst: (a) TEM image; (b) Rh nanoparticle size distribution.

The increased selectivity of CO and decreased selectivity of CO_2 with the water-treated catalyst could be attributed to smaller Rh nanoparticles on the alumina support, as they could provide larger surface areas and increase the contact area with reactants, thus prodiving higher reaction efficiency. Unpublished results [12] for Pt/γ-Al_2O_3 suggest that the chemisorption

strength of CO onto water-treated catalysts is significantly reduced, allowing more competitive adsorption of other reactants and products. These water-treatment mechanisms require more investigation.

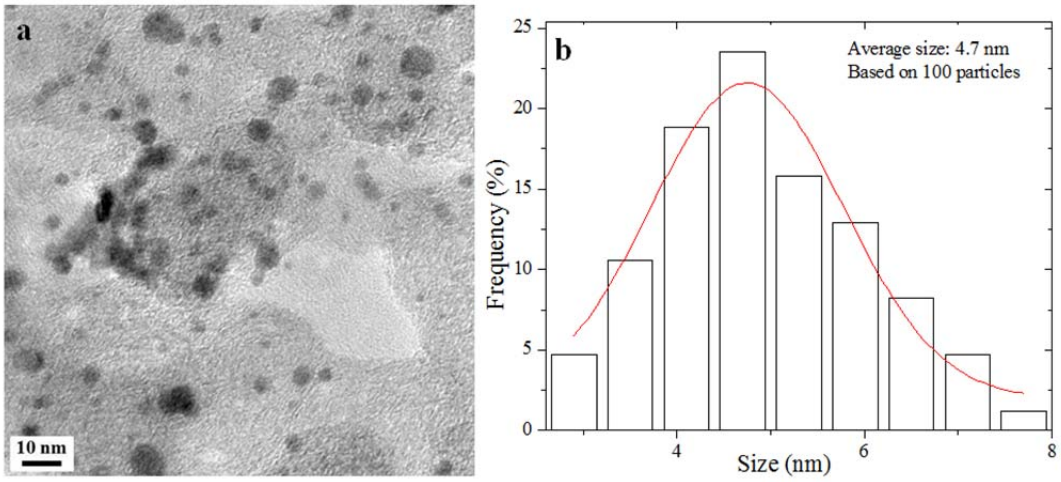

Fig. 5. Water-treated 1 wt% Rh/γ-Al_2O_3 catalyst: (a) TEM image; (b) Rh nanoparticle size distribution.

1.2.5 Conclusions

Both standard-treated and water-treated catalysts were tested for themethane partial oxidation reaction. Water-treated catalyst shows higher CO and CO_2 selectivity in the temperature range of 300-600 ^{o}C. The enhancement is attributed to the formation of well-dispersed smaller Rh nanoparticles after water treatment. Further research is needed to explore the mechanism of Rh nanoparticle size decreasing during the water treatment process.

Referenences

1. Khine, M. S. S., Chen, L. W., Zhang, S., Lin, J. Y. & Jiang, S. P. Syngas Production by Catalytic Partial Oxidation of Methane over $(La_{0.7}A_{0.3})BO_3$ (A = Ba, Ca, Mg, Sr, and B = Cr or Fe) Perovskite Oxides for Portable Fuel Cell Applications. *International Journal of Hydrogen Energy*, **38**, 13300-13308 (2013).
2. Liso, V., Olesen, A. C., Nielsen, M. P. & Kaer, S. K. Performance Comparison between Partial Oxidation and Methane Steam Reforming Processes for Solid Oxide Fuel Cell (Sofc) Micro Combined Heat and Power (CHP) System. *Energy*, **36**, 4216-4226 (2011).
3. Pinol, S., Morales, M. & Espiell, F. Hydrogen Production by a New Selective Partial Oxidation of Methane in Air Using Reducted $La_{0.5}Sr_{0.5}COO_3$-Delta as Catalyst for Fuel Cell Applications. *Journal of New Materials for Electrochemical Systems*, **11**, 119-124 (2008).
4. Li, B. *et al.* Synthesis Gas Production from Partial Oxidation of Methane over Highly Dispersed Pd/SiO_2 Catalyst. *Fuel*, **103**, 1032-1038 (2013).
5. Dai, X. P. & Yu, C. C. Direct Partial Oxidation of Methane to Synthesis Gas Using Oxygen Carriers in the Absence of Gaseous Oxygen. *Progress in Chemistry*, **21**, 1626-1635 (2009).

6. Son, I. H., Shamsuzzoha, M. & Lane, A. M. Promotion of Pt/Gamma-Al_2O_3 by New Pretreatment for Low-Temperature Preferential Oxidation of Co in H_2 for Pem Fuel Cells. *Journal of Catalysis*, **210**, 460-465 (2002).

7. Jo, M. C., Kwon, G. H., Li, W. & Lane, A. M. Preparation and Characteristics of Pretreated Pt/Alumina Catalysts for the Preferential Oxidation of Carbon Monoxide. *Journal of Industrial and Engineering Chemistry*, **15**, 336-341 (2009).

8. Son, I. H., Lane, A. M. & Johnson, D. T. The Study of the Deactivation of Water-Pretreated Pt/Gamma-Al_2O_3 for Low-Temperature Selective CO Oxidation in Hydrogen. *Journal of Power Sources*, **124**, 415-419 (2003).

9. Tomita, A., Shimizu, K., Kato, K., Akita, T. & Tai, Y. Mechanism of Low-Temperature CO Oxidation on Pt/Fe-Containing Alumina Catalysts Pretreated with Water. *Journal of Physical Chemistry C*, **117**, 1268-1277 (2013).

10. Tomita, A., Shimizu, K., Kato, K. & Tai, Y. Pt/Fe-Containing Alumina Catalysts Prepared and Treated with Water under Moderate Conditions Exhibit Low-Temperature Co Oxidation Activity. *Catalysis Communications*, **17**, 194-199 (2012).

11. Lopez-Fonseca, R., Jimenez-Gonzalez, C., de Rivas, B. & Gutierrez-Ortiz, J. I. Partial Oxidation of Methane to Syngas on Bulk Nial2o4 Catalyst. Comparison with Alumina Supported Nickel, Platinum and Rhodium Catalysts. *Applied Catalysis A-General*, **437**, 53-62 (2012).

12. Sun, I. H. Promotion of Platinum/gamma-aluminum Oxide for Preferential Oxidation of Carbon Monoxide in Hydrogen for PEM Fuel Cells by Cerium Promoter and by Preparation of Stable Platinum Nanoparticles Using a Water-pretreatment. Ph.D. Dissertation, The University of Alabam, 2003.

1.3 Task A.3 Investigate Low Temperature, Fuel-Flexible Combustion using Porous Inert Media: (*Prof. Paul V. Puzinauskas*):

1.3.1 Overview. This section describes the final status of Task 3. This 'Overview' subsection is followed by subsections describing the created test system in detail and the on-going efforts to complete the proposed and additional research utilizing the constructed system. The remainder of this 'Overview' subsection describes the objective and purpose of this task and provides a brief summary of its status.

1.3.2 Objective and Purpose. The first objective of this task was to construct and characterize a reciprocating-engine combustion system development platform. The second objective was to utilize this platform to explore how porous media may be used to facilitate low temperature combustion in reciprocating engines. The primary purpose of the platform is to conveniently facilitate exploration of advanced novel or experimental combustion-system concepts for reciprocating internal-combustion engines. To explore such concepts often requires significant modification to the combustion chamber geometry, which can impact the cooling and fuel and air-delivery systems in conventional water-cooled, four-stroke cycle engines. This may require complex re-engineering of the cooling systems and valve-train. To reduce this complexity, the platform developed in this effort is based on an air-cooled, two-stroke cycle motorcycle engine.

Status. This system has been completely constructed with the majority of the troubleshooting complete. This investigation will to explore the ability to use an air-cooled, two-stroke HCCI engine as range extender for an electric vehicle is also underway. These efforts are described in more detail in the On-going Activities section.

1.3.3 Test Platform Description. This subsection describes the design of the test platform and the associated modifications to the test engine and provides an overview of the efforts to characterize its function.

Test Platform Design. The test platform was constructed using a highly-modified crankcase-scavenged two-stroke cycle engine integrated with an AC-motor dynamometer controlled with a variable-speed AC motor drive. A separate air cart, based on an AC-motor driven supercharger, was constructed to supply pressure and temperature controlled intake air. These systems' details are provided in the paragraphs that follow.

A picture of the combustion-system development test platform is shown in Figure 3.1. A 1975 Yamaha 125[cc], air-cooled, crankcase-scavenged two-stroke cycle engine was used for the combustion development environment. As indicated above, the combustion chamber of this type of engine is inherently very simple and conveniently facilitates incorporation of advanced combustion concepts. Crankcase scavenging, however, is not the ideal method for achieving the intake pressurization necessary to execute the two-stroke cycle when studying the details of the combustion process. To understand the reason for this, it is necessary to understand how crankcase scavenging works.

Figure 3.1: Engine advanced combustion system development platform

Figure 3.2 shows the configuration and flow path of a crankcase scavenged, single-cylinder two-stroke cycle engine similar to the engine we used. In this configuration, the fuel and air enter into the engine crankcase as the piston ascends during the latter part of the compression stroke, and then are compressed as the piston descends in the cylinder during the early part of the expansion stroke. A reed valve at the entrance port prevents the charge from flowing back out the supply port as the crankcase pressure builds. After about ¾ of the expansion stroke, a transfer port opens allowing the compressed charge to enter the cylinder and push the exhaust gasses out of the cylinder. Once the piston reverses and travels far enough up the cylinder to cover both the transfer and the exhaust ports, the compression process begins. Because the charge is in contact with the moving parts of the slider-crank mechanism, two-stroke cycle engines using crankcase pressurization scavenging typically require lubricating oil to be mixed in with the fuel. Furthermore, since all the scavenging air used to force out the exhaust is fully mixed with fuel, any short circuiting from the transfer to the exhaust ports will result in very high unburned HC emission. This could overwhelm the effects of combustion system modifications we are studying and make them hard to quantify- in particular if exhaust emission measurements are being used for the quantification.

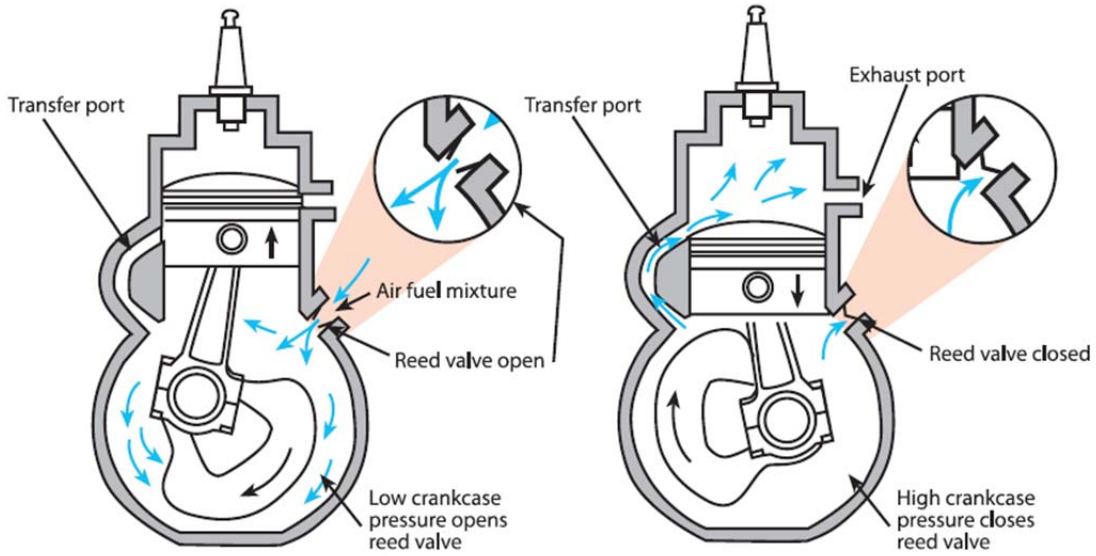

Figure 3.2: Crankcase scavenged two-stroke cycle flow path.

To eliminate the issues associates with the crank-scavenged configuration, our engine has been modified to follow a scavenging strategy used in direct-injected two-stroke cycle engines. The connection between the crankcase and the intake port made by the transfer port has been eliminated. Instead, externally pressurized air is supplied through newly machined intake ports directly into the cylinder. A picture of one of these ports integrated into the cylinder is shown in Figure 3.3. Two ports were integrated axisymmetric with the exhaust outlet. A symmetric, twin runner intake manifold was fabricated to route the air to the ports. The manifold runner has provisions to mount typical port fuel injectors. The cylinder head can also be easily modified to accommodate direct (into the cylinder) injectors. In either configuration, the injection timing can be adjusted to minimize or eliminate the presence of fuel in the any air that short circuits from the intake to exhaust ports during scavenging. This would ensure that the majority of UHCs measured in the exhaust would be attributable to incomplete combustion and not fuel short-circuiting. Achieving this is clearly more straightforward using direct injection, since injection can simply be delayed until both intake and exhaust ports are closed.

Figure 3.3: Modified intake port

As is evident in Figure 3.1, the engine is coupled to an AC dynamometer on top of a specially fabricated, heavy-duty table. The dynamometer is controlled by a solid-state variable-speed drive. The engine and dyno are spaced such that an in-line torque meter can be utilized to measure engine brake torque. Since most combustion-system studies will rely on indicated measurements from a combustion pressure measurement and analysis system, the in-line torque meter will not usually be necessary. Therefore, a conventional (non-torque sensing) shaft is usually used to couple the engine to the dyno. The crankshaft encoder and pressure transducer used for the combustion-pressure measurement system are evident in the figure. An oil tank, pump, cooler and filter are mounted under the main table surface. This oiling system is necessary since the crankshaft and reciprocating components are no longer lubricated by the fuel-air charge which was originally delivered to the crankcase. A flow-control valve is placed between the high-pressure output and the crankcase-mounted nozzle which sprays the friction surfaces with oil. The valve is used to adjust the flow to insure adequate lubrication without overfilling the crankcase.

In addition to quantifying cycle-resolved cylinder pressure and providing a suite of related calculations, the combustion pressure measurement and analysis system is used to control fuel injection and, when running in spark-ignition mode, ignition. The system includes digital I/O channels which can programmed to output digital signals timed at specific engine crank angle position. An amplifier-driver circuit was constructed to amplify these low-current outputs to enable driving fuel injector or ignition circuits. Currently the engine is configured for port-injection using gaseous fuel and spark-ignition.

Figure 3.4 shows the air cart developed to provide temperature controlled, pressurized scavenging air to the engine. The air cart consists of a roots positive-displacement blower driven by an AC motor powered with a variable speed drive, a charge-air to water heat exchanger and a feedback-loop charge air temperature control system with heating and cooling capability. The heating capability is provided by a heating element located in the hot-water tank. The hot water is circulated from the tank using an electric pump. A fluid level sensor and thermostat installed in the hot water tank insure the water and heating element do not overheat. The cooling capability is provided by cooled process water available in the ECL. The process water supply and return are coupled to the air cart through standard water hose connections and its circulation is driven by a pressure differential created across the supply and return by the main process water pump. A set of solenoid flow-control valves are actuated by a processes controller mounted to the cart to direct hot or cold water to the charge-air heat exchanger as needed to maintain the desired intake air temperature. The VSD used to control the motor driving the supercharger is completely independent from the engine dyno VSD; therefore, the pressure and temperature of the air entering the engine can be controlled completely independently from the engine speed or load.

Figure 3.4: Air pressurization and conditioning cart

Analysis and Testing. A CFD study was performed to characterize the flow behavior of the reconfigured engine. The initial CFD efforts utilized the numerical calculations available integrated within the SolidWorks solid mechanics design package which was used to design and incorporate the various components necessary for the conversion from crankcase scavenging. While it was convenient to keep the analysis in the CAD package, the SolidWorks CFD capability is limited and not capable of simulating moving boundaries such as those in a reciprocating engine. Therefore, the CFD analysis was ported to Ansys/Fluent in order to accommodate future efforts of multi-component (eg fuel and air) flows and moving engine parts. Figure 3.5 and Table 3.1 show steady Fluent results from a series of three where 111, 121 and 151 [kPa] intake pressures were used and exhaust pressure was maintained at 101 [kPa].

Table 3.1: Summary of CFD intake pressure study.

	Intake Pressure [kPa]		
	111	121	151
$\dot{m}\ \left[\frac{kg}{s}\right]$	0.036	0.053	0.088
$V\ \left[\frac{m}{s}\right]$	126	160	261
$P_{max}\,[kPa]$	110.6	120.0	148.4

As is expected, the in-cylinder pressure, mass flow rate through the engine and velocities increase with increased in intake pressure. The velocity intensity plots show the velocity gradients and therefore the associated shear also increase with intake pressure. Such increases in shear will increase the rate of mixing and result in

higher turbulence. The streamlines are not significantly altered with the 10 kPa increase to 121 [kPa], but at 151 [kPa], it is evident that the streamlines are less circular within the cylinder and tend to follow the contour of the combustion chamber shape. This is because the higher momentum associated with the higher velocities generated at higher intake pressure would require greater influence from the walls to change direction. In all cases, it appears any dead-space in the cylinder is limited, so complete scavenging should be possible at all boost pressures. While these result are largely intuitive, being able to quantify streamline velocities will help to optimize fuel injection timing by providing an estimate of the earliest injection possible to avoid fuel short circuiting to the exhaust port. This could be much more accurately defined modeling a separate injection process with a two (gas) component analysis with the piston boundary moving to represent actual engine motion. This could be the subject of future work.

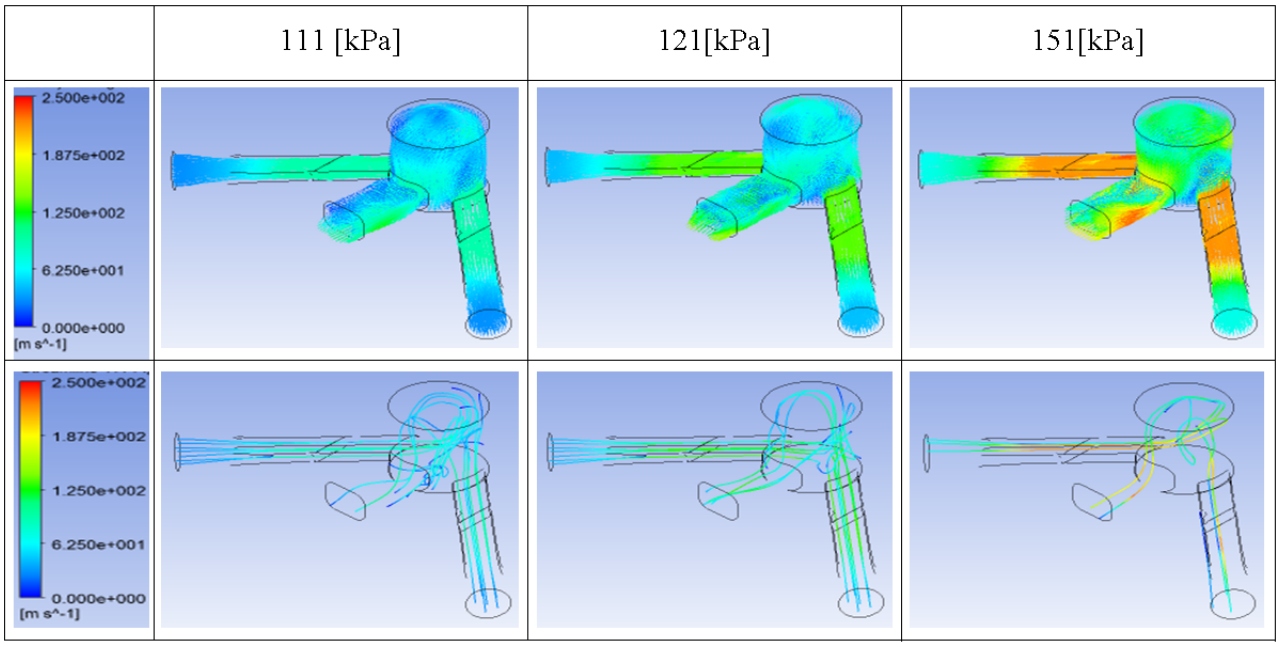

Figure 3.5: Fluent CFD simulation of flow through modified flow path.

1.3.4 Future plans.

Currently, two programs using this platform are underway. The first is the research task we proposed to pursue once the platform was completed and commissioned. This task involved investigating the effect of porous media on HCCI combustion. We expected to complete this investigation within the ISE program; however, significant delays associated with bringing UA's new state-of-the-art ECL on line resulted in a nearly two-year dead period from when our original laboratory was closed (where we started this project) and our new facility became fully operational. While we were able to refine and test

Figure 3.6: Fabricated cylinder head for low temperature combustion study.

some of the components of the platform during this time, our ability to run the engine and perform necessary measurements for research was limited. A custom cylinder head was constructed to achieve HCCI-capable compression ratios and incorporated provisions to mount the porous media. Figure 3.6 shows a photograph of this head. It is apparent from the photograph how simple this task was relative to doing something similar in a four-stroke cycle, water-cooled engine where valve-train and cooling jackets would significantly complicate the necessary modifications.

The second project utilizing this platform involves optimizing a two-stroke cycle engine to drive an electric generator used as a range-extender for an electric vehicle. Since such an engine doesn't have to operate over nearly the bandwidth of a conventional automotive engine, many of the shortcoming of the two-stroke cycle can be mitigated. This project is being carried out by students on UA's EcoCAR 3 program. EcoCAR 3 is the latest iteration of the Advanced Vehicle Technology Competition (AVTC) managed by Argonne National Laboratory and primarily funded by DOE and General Motors. This development effort is part of a larger innovation initiative incorporated into the competition.

2.1 Task B: Seminar Series and Technical Workshop

A seminar series that brought prominent speakers to the campus (see a flyer on the next page) was conducted. The seminars were well attended with typical attendance of 70 plus students, faculty, and staff from across campus.

A workshop on Sustainable Fuels: Production and Combustion was held on July 29, 2014. Ten speakers from industry, government, and academia were invited to make the technical presentations. The workshop program is attached at the end of this document. The information about the workshop was sent to universities in Alabama and the region, and to wider community through The Combustion Institute mail list. A website was created to participants to register for the workshop.

A total of 75 people registered for the workshop, and we had to close the registration because it building capacity limitations. The workshop was very effective in bringing together researchers in the area, and we expect that it will result in collaborative proposals and research to continue to fulfill the mission of the Institute for Sustainable Energy. Participant organizations included: Southern Company, John Zink Hamworthy, Fives North America, CFD Research Corporation, Oak Ridge National Laboratory, US Department of Agriculture, Auburn University, and Washington University. It covered fields of vehicular transportation, power generation, industrial transportation, and aviation.

Spring 2013 Seminar Series, SERC 1013, 2:00pm-3:00pm

Institute for Sustainable Energy &
Department of Mechanical Engineering
University of Alabama

COMBUSTION LABORATORIES
THE UNIVERSITY OF ALABAMA
LOW EMISSIONS • HIGH EFFICIENCY • FUEL FLEXIBILITY

February 7, 2013 Combustion Dynamics in Propulsion Systems

Vigor Yang, Williams R.T. Oakes Professor & Chair of School of Aerospace Engineering, Georgia Tech

Prof. Yang is Fellow of AIAA, ASME, and the Royal Aeronautic Society, and serves as AIAA Vice President for Publications. In this lecture, he will provide an overview of combustion instabilities in solid-rocket, liquid-rocket, gas turbine, and ramjet/scramjet engines addressing acoustic, fluid mechanics, and chemistry issues.

February 21, 2013 Using Photosynthesis to Make Fuels and Chemicals

Anastasios Melis, Professor of Plant & Microbial Biology, University of California, Berkeley

Prof. Melis is Fellow of American Association for the Advancement of Science, and recipient of US DOE Research Achievement Award. This talk will discuss the application of photosynthesis for the direct generation and release of fuels and chemicals, bypassing the need to harvest and process the respective biomass.

March 7, 2013 Leveraging the Best Features of The Next Generation of Fuels

Margaret Wooldridge, Arthur F. Thurnau Professor, Departs of Mech. & Aerospace Eng, University of Michigan

Prof. Wooldridge is Fellow of ASME, Society of Automotive Engineers (SAE), and past co-director of the Global Automotive and Manufacturing Program. This presentation will focus on her research on the effects of different fuels on ignition systems, spanning chemically controlled reactors to production internal combustion engines.

March 14, 2013 Gas Turbine Combustion: Present and Future Challenges

Mohan Razdan, Chief Engineer, Combustion and Casings, Rolls-Royce Corporation, Indianapolis

Dr. Razdan manages all aspects of combustion systems at Rolls-Royce, a world leader in the design, manufacturing, and service of aircraft engines. In this presentation, he will offer an industrial perspective on major challenges to developing advanced gas turbine combustors for aircraft engines.

April 4, 201 Science and Art of Visualizing Fluid Flows by Refractive Optical Techniques

Gary Settles, Distinguished Professor of Mechanical Engineering, Penn State University

Prof. Settles is the Director of the Penn State Gas Dynamics Laboratory since 1983 and is author of the text *Schlieren and Shadowgraph Techniques*. This presentation will discuss interesting applications of these techniques to study fluid flows phenomena as well as to create intriguing artwork.

April 11, 2013 Methane Hydrate Combustion

Derek Dunn-Rankin, Professor & Chair of Depart. of Mechanical Engineering, University of California, Irvine

Prof. Dunn-Rankin is an officer of International Combustion Institute Board, and has published over 300 papers in combustion and energy fields. This presentation will describe combustion of methane released from gas hydrates, ice-like crystalline solids found in large quantities on the seafloor and in the arctic permafrost.

April 15, 2013 Optical Diagnostics of In-cylinder Processes for Advanced Diesel Engines

Mark Musculus, Scientist, Combustion Research Facility, Sandia National Laboratory, Livermore, CA

Dr. Musculus received his PhD from the University of Wisconsin in 1998. In this seminar he will discuss his research focusing on science-based understanding of new, clean combustion strategies for high fuel-efficiency internal combustion engines using advanced optical and laser-based diagnostic techniques.

Technical Workshop on

Sustainable Fuels: Production & Combustion

Tuesday, July 29, 2014

- Institute for Sustainable Energy (ISE) conducts innovative science and technology research to utilize the complex mix of conventional, alternate, and opportunity fuels in energy efficient and environmentally sound manner.
- This ISE sponsored technical workshop is targeting researchers working on production, processing, & combustion of conventional, alternative, and opportunity fuels.
- Workshop is free to all participants, and limited travel funds are available for presenters. Poster presentations by students are encouraged.
- Workshop will be held in UA's new South Engineering Research Center (SERC), and it will include tours and demonstrations of Engines and Combustion Laboratories (ECL) and other research facilities.

Institute for Sustainable Energy

Department of Mechanical Engineering

University of Alabama

THE UNIVERSITY OF ALABAMA ENGINEERING

COMBUSTION LABORATORIES THE UNIVERSITY OF ALABAMA

LOW EMISSIONS • HIGH EFFICIENCY • FUEL FLEXIBILITY

Research on production, processing, and combustion of biofuels and opportunity fuels

Spend a day interacting with fuels/combustion/ alternative energy researchers

Invited talks, student poster presentations

Free Registration, meals, and materials

Facility tours and demonstrations at Engines and Combustion Laboratory (ECL)

CONTACT

Prof. AJAY K AGRAWAL

aagrawal@eng.ua.edu

(205) 348-4963/799-7129

Reception: July 28, 2014 (6:30pm onwards)

Workshop: July 29, 2014 (8:00 am - 5:00 pm)

Location: 1059 SERC

Technical Workshop on

Sustainable Fuels: Production and Combustion

Tuesday, July 29, 2014

Institute for Sustainable Energy

College of Engineering, University of Alabama

South Engineering Research Center (SERC 1013 and 1059)

***For Free Registration and Additional Details, visit*: http://ise.eng.ua.edu**

8:00 am **Registration and Networking Coffee with Continental Breakfast, SERC 1013**

8:40 am **Welcome Remarks, Dr. Joe Benson, Provost and Vice President for Academic Affairs**

8:50 am **Announcements and Overview of the Workshop, Prof. Ajay K Agrawal**

9:05 am **Next Generation Combustion Engines and Future Fuel Opportunities**

Robert Wagner; Fuels, Engines and Emissions Research Center, Oak Ridge National Laboratory, Knoxville, TN

New technologies coupled with advances in sensors and onboard computers will enable real-world implementations of new combustion concepts as well as new fuel pathways that blend the best characteristics of spark-ignition and compress-ignition engines for maximum efficiency with lowest possible emissions. A detailed discussion of related research and relevant background on ORNL will be provided in this presentation.

9:40 am **21st Century Energy Sources**

Chad Hewitt; Fuel Services, Southern Company Generation, Birmingham, AL

Coal has been the backbone of America's energy needs.
Will natural gas become America's next base load fuel?
What role does Nuclear, Biomass, Wind, and Solar play?

10:15 am **Challenges in Deploying a Biofuel Industry in the Southern U.S.**

Steven E. Taylor; Professor and Head, Dept of Biosystems Engineering, Auburn University, AL

The southern U.S. has the ability to produce more than half of the advanced biofuels needed by our nation. While there have been significant R&D investments in biofuels, challenges remain to deployment of a sustainable "drop-in" biofuels industry based on lignocellulosic biomass feedstocks. This presentation will discuss these challenges and selected efforts underway by Auburn University and its partners to address them.

10:50 am **Development of Sustainable Fuels and Efficient Combustion Technologies through Experiments, Modeling and Simulations**

Ranjan S. Mehta; CFD Research Corporation, Huntsville, AL

CFDRC is active in development of combustion models that can be applied to bio-derived fuels in a computationally efficient manner. This presentation will briefly describe these activities and also present our outlook on emerging technologies for sustainable fuels and combustion technology.

11:25 am **Industrial Combustion Applications with Different Fuels**

Charles E. Baukal; John Zink Hamworthy Company, Tulsa, OK

This presentation will be a survey of industrial combustion applications including metals (e.g., ferrous and non-ferrous), minerals (e.g., glass and cement), chemicals and petrochemicals (e.g., heaters and furnaces), and power generation (e.g., boilers). A wide range of gaseous fuels, oxidizers, burners, temperatures, and combustors will be discussed. The diversity of the applications shows the varied needs and requirements in different industries.

12:00 noon to 1:00 pm **LUNCH**
3rd Floor Terrace Facing Science and Engineering Quad, SERC

1:00 pm – 2:00 pm
Poster Session &
Engine and Combustion Lab (ECL) Tours
Small groups will rotate through poster session and lab tours
Please re-convene in SERC 1059 for the afternoon presentations

2:00 pm Biodiesel: Fuel Properties, Its "Design" and a Source of "Designer" Fuel
Gerhard Knothe; U.S. Department of Agriculture, Peoria, IL
This presentation will give an overview of biodiesel fuel properties for different fatty acid alkyl esters and how they affect the biodiesel mixture as well as discuss components of biodiesel that lead to a fuel with improved properties, "designer" biodiesel. Optimized biodiesel could be based on enrichment in palmitoleic or decanoic acids. Although facing agronomic issues, a potential source of biodiesel enriched in decanoic acid is cuphea oil.

2:35 pm Staged, Pressurized Oxy Combustion for Cost-Effective Carbon Capture
Richard L. Axelbaum; Washington University, St. Louis, MO
This talk focuses on fossil fuel combustion to understand the formation of pollutants, such as soot, and then using this understanding to develop novel approaches to eliminating them. In particular, global concerns over carbon dioxide emissions are addressed by developing oxy combustion for cost effective carbon capture and storage (CCS).

3:10 pm National Carbon Capture Center for Near Zero Emissions
John Socha; Project Manager, National Carbon Capture Center, Wilsonville, AL
Offering a world class neutral test facility and a highly specialized staff, the **National Carbon Capture Center** *accelerates the commercialization of advanced technologies to enable coal-based power plants to achieve* **near-zero emissions.**
Current projects involving chemical looping technology, Fischer-Tropsch coal to liquids catalyst, and Pressure Swing Adsorption unit will be discussed.

3:45 pm Well-to-Wheel Analysis of Direct & Indirect use of Natural Gas in Passenger Vehicles
Scott Curran; Fuels, Engines and Emissions Research Center, Oak Ridge National Laboratory, Knoxville, TN
This presentation discusses the well-to-wheels energy and emissions costs from different natural gas to transportation fuel pathways and compares the results to conventional gasoline vehicles and electric vehicles using the US electrical generation mix. Results show the dependency on the combustion efficiency of natural gas in stationary power can outweigh the inherent efficiency of electric vehicles.

4:20 pm Practical Challenges for the Industrial Burner Industry
John Nowakowski; Fives North American Combustion, Cleveland, OH
Industrial combustion applications often need to accommodate multiple fuels when there are by-products or co-products of processes elsewhere in the facility, such as when various gases are recovered during thermally enhanced oil recovery operations. This presentation shares such challenges and practical approaches for considering the tradeoffs.

4:55 pm Vote of Thanks
5:00 pm – 6:30 pm Social Hour; Poster Session; Optional Lab Tours

Institute for Sustainable Energy (ISE)
College of Engineering, University of Alabama

Goals: Alternate fuels offer unique challenges and opportunities as energy source for power generation, vehicular transportation, and industrial applications. Institute for Sustainable Energy (ISE) at The University of Alabama (UA) conducts innovative research to utilize the complex mix of domestically-produced alternate fuels to achieve low-emissions, high energy-efficiency, and fuel-flexibility. ISE also provides educational and advancement opportunities to students and researchers in the energy field.

Alternative Fuels: We have developed strategies to achieve clean combustion of liquid biofuels (biodiesel, bio-oils, etc) by utilizing a novel fuel-injection concept relying upon aerodynamically created two-phase mixing. This concept consists of a fuel tube and an exit orifice separated by a small gap. The atomizing air mixes with fuel upstream of the fuel-tube tip to create a two-phase flow. Through the injector orifice, the two-phase flow is subjected to a rapid pressure drop, leading to expansion and breakup air bubbles and yielding spray with fine droplets. This fuel injector concept offers the intriguing prospect of cleanly combusting relatively crude liquid biofuels for power generation and automotive applications. Thus, fuel processing steps required to convert biomass into liquid biofuels with precisely controlled physical and chemical properties can be greatly simplified to reduce the overall cost and emissions.

Fuel-Flexible Combustion Systems: For automotive applications, we have developed a novel combustion approach to shift the paradigm by dividing the complex engine flow and chemical processes into two steps: (1) an external step involving injection, atomization, and vaporization of liquid fuel(s), mixing of fuel and oxidizer, and subsequently, fuel reformation or partial oxidation to produce syngas fuel outside the engine cylinder, and (2) an internal step involving injection of syngas fuel into the engine cylinder containing ingested air, followed by low temperature combustion (LTC) based on homogeneously-charged compression ignition (HCCI) concept. Research has been conducted to develop and characterize key aspects of this concept including a fuel-flexible fuel reformer, a combustion-system flexible two-stroke research engine test platform, and procedures to isolate and coat catalysts on a porous bed for use inside the engine and fuel reformer to selectively increase the chemical activity.

Prof. Ajay K Agrawal, aagrawal@eng.ua.edu
Prof. Paul Puzinauskas, ppuzinauskas@eng.ua.edu;
Prof. Alan Lane, alane@eng.ua.edu

Patents: None

Publications (listed in order of placement in Appendix A)

- Lulin Jiang, Ajay K Agrawal, and Robert P Taylor, 2013, "Alternate fuel combustor operated on glycerol and methane," 8th US National combustion meeting 2013, Salt Lake city, UT, USA.
- Lulin Jiang, Pankaj S Kolhe, Robert P Taylor, and Ajay K Agrawal, 2012, "Measurements in a Combustor Operated on Alternative Liquid Fuels," 50th AIAA Aerospace Sciences Meeting including the New Horizons Forum and Aerospace Exposition, Nashville, Tennessee, January 9th – 12th, 2012.
- Thompson W.C., and Agrawal, A.K., 2013, "Analysis of a mesoscale fuel reformer with heat recirculation and porous surface stabilized flame," 8th US National combustion meeting 2013, Salt Lake city, UT, USA.
- Thompson W.C., Hershman D., and Agrawal, A.K., 2012, "Innovative Reforming Reactor System for Partial Oxidation and Autothermal Fuel Reforming," Spring Technical Meeting of the Central States Section of the Combustion Institute April 22–24, 2012.
- P.S. Kolhe, and A.K. Agrawal, 2013, "Ultra high speed rainbow schlieren deflectometry for statistical description of turbulent low density jets," 8th US National combustion meeting 2013, Salt Lake city, UT, USA.
- Kolhe P.S. and Agrawal, A.K., 2012, "Ultra High-Speed Rainbow Schlieren Deflectometry for Turbulence Measurements in Jets and Flames," Spring Technical Meeting of the Central States Section of the Combustion Institute April 22–24, 2012.

Appendix A: Publications

8th U. S. National Combustion Meeting
Organized by the Western States Section of the Combustion Institute
and hosted by the University of Utah
May 19-22, 2013

Alternate Fuel Combustor Operated on Glycerol and Methane

Lulin Jiang, Ajay K. Agrawal and Robert P. Taylor

Department of Mechanical Engineering, University of Alabama,
Tuscaloosa, Alabama 35401, USA

Abstract

Disposal of glycerol, the byproduct from biodiesel production, is an emerging issue with the increasing interest in utilizing fuels produced from biomass. Glycerol and other industrial waste products with moderate amounts of stored chemical energy can be economically viable alternative fuels because of their low cost. Previous research has shown that glycerol is combustible, in spite of its high ignition temperature, by preheating the combustion zone with propane or methane. We have reported that glycerol with its extraordinarily high kinematic viscosity can still be finely atomized by the so-called flow blurring (FB) injector to produce clean flames with extremely low emissions at the combustor exit. In the present study, a fuel-flexible combustor with a FB injector is utilized to simultaneously burn liquid and gaseous fuels. Measurements of product gas temperature and CO and NO_x emissions are acquired at various axial and transverse locations inside a swirl-stabilized combustor to illustrate the flame structure. For a fixed heat release rate (HRR), methane and glycerol flow rates are varied to vary the percentages of HRR from each fuel and thus, the fuel mix. For a fixed fuel mix, the air-to-liquid mass ratio (ALR) through the injector is varied to investigate its effect on the flame structure. Results show low-emissions with combustion of glycerol without and with methane supply. The addition of methane improves glycerol combustion by improving fuel vaporization, fuel-air mixing, and fuel oxidation resulting in localized zones of higher product gas temperatures. CO emissions decrease and NO_x emissions increase when increasing the percentage of HRR from methane. Higher ALR improves atomization to form smaller droplets that vaporize rapidly and result in shorter primary reaction zone with higher local temperatures reducing CO emissions and increasing NO_x emissions. In spite of these differences, all fuel combinations result in complete combustion with extremely low CO and NO_x emissions at the combustor exit.

1. Introduction

Disposal of glycerol, the byproduct from biodiesel production, is an emerging issue with the increasing interest in utilizing fuels produced from biomass. About 1 kg of crude glycerol is generated for 9 kg of biodiesel produced [1]. Even though pure glycerol finds applications in food, cosmetics and pharmaceutical industries, it is too costly for biodiesel producers to refine crude glycerol into high purity glycerol. Therefore, glycerol generated during biodiesel production is often considered a waste product causing environmental problems. Conversion of glycerol into value added products and chemicals has been studied in recent years. For instance, glycerol could be blended with gasoline to recover some of its chemical energy in the form of an alternative fuel [2]. Glycerol is an attractive feedstock for producing chemicals such as 1, 3-propanediol with end uses into corterra polymers, UV-Cured coatings, solvents and anti-freeze, etc [3, 4]. Using Enterobacter

Aerogenes HU-101 to convert glycerol into fuels such as hydrogen and ethanol has been studied for future portfolio of alternative fuels [5]. While the previous research offers routes to convert glycerol into useful products, significant cost and energy is still required. For example, anaerobic digestion of glycerol recovers only 11.93 MJ/kg out of around 16 MJ/kg energy in glycerol [6].

Previous research has shown that glycerol is combustible, in spite of its high ignition temperature and high kinematic viscosity at the room temperature. Thus, direct combustion of glycerol can be an economically viable solution to effectively utilize glycerol to meet our energy needs. Recently, McNeil et al. [7] tested glycerol combustion in a compression ignition engine by supplying air at above 90°C and glycerol at around 144°C to decrease viscosity and overcome the high ignition temperature characteristic of glycerol. The results showed low emissions of CO, NO_x, and particulates, and low emissions of carbonyl such as acrolein from glycerol operation than equivalent engines operating on diesel or biodiesel fuel. Glycerol fuel also improved the stability over the engine operation increasing catalyst efficiency and lowering the chance of catalytic degradation. Direct combustion of glycerol resulted in 2.3 time greater heat recovery than the anaerobic digestion process. This study suggested that engine operation with glycerol would comply with the strictest emission standards for many years to come such the proposed 2015 Tier 4 Californian Emissions Standards.

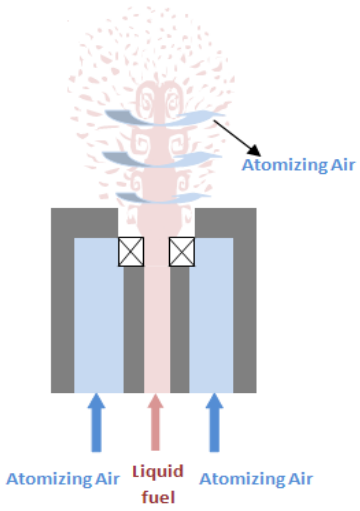

Fig. 1 Diagram of siphon air atomizing nozzle.

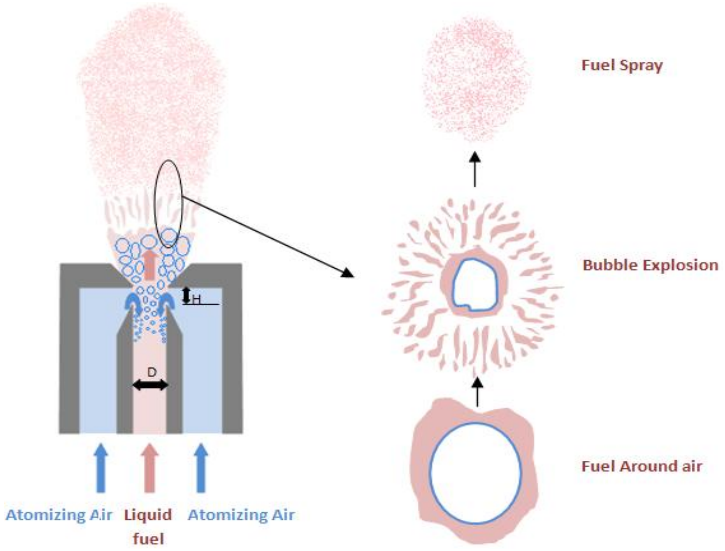

Fig. 2 Working principle of the flow blurring injector

For continuous flow applications such as gas turbines and burners, previous research has shown that glycerol can be successfully combusted. Metzger [8] used a Delavan Siphon type SNA Air-Blast (AB) atomizer to form glycerol spray at room temperature using pressurized air. A liquid fuel pump was used to pump the glycerol and a much higher flow rate of air was necessary compared to that needed to atomize kerosene or diesel. Likewise, Myles et al. [9] used an air-assist atomizer (Delavan model 30609-3) to create glycerol spray. In this study, glycerol was preheated to 93°C and atomizing air was preheated to 150°C before the two fluids were supplied to the fuel injector. Preheating glycerol can dramatically decrease its viscosity to levels similar to conventional fuel oils, which is highly beneficial to create a fine spray. However, AB injector is not ideal for glycerol and other highly viscous fuels because of the high energy input required to supply large amounts of pressurized air for atomization; Figure 1 shows the working principle of AB atomizer, whereby high velocity airflow is introduced from the injector to destabilize the shear layer of the fuel jet, which

can result in a spray with fine droplets. However, the shear layer instabilities are suppressed by high kinematic viscosity of the fuel, which limits the ability of the AB injector to produce a fine spray [10].

Another kind of fuel injector, flow-blurring (FB) injector, was used by Benjamin et al. [10]. Gañán-Calvo [11] first reported that for a set atomizing air flow rate, the FB injection concept created "five to fifty times" more fuel surface area than a plain-jet AB atomizer. This injection method utilizes two-phase flow concept to create the spray. The injection principle shows in Figure 2 [12] consists of a fuel tube and an exit orifice both of diameter, D and a gap of height H between the fuel tube tip and the orifice. If the ratio H/D is less than 0.25, the atomizing air bifurcates as it reaches the gap between exit orifice and the fuel tube tip. A portion of the air flows into the fuel tube, while the rest leaves the injector through the orifice. The turbulent two-phase flow created inside the fuel tube, then leaves the injector through the orifice. Significant decrease of pressure in the orifice cases air bubbles to expand and break apart the surrounding liquid into fine droplets. Previous studies have shown that FB injector provides finer spray with lower energy input since it incurs a lower pressure drop in the atomizing air line [13-14]. Liquid fuel atomized by FB atomizer burns in lean premixed (LPM) mode and thus yields lower CO and NOx emissions [12, 15-16]. Previous research by our group has proven that in spite of high kinematic viscosity, glycerol can be finely atomized by FB injector. Glycerol has a high ignition temperature and has to be combusted in the combustion zone with very high temperature to get stable flame. In spite of these challenges, very low emissions at the combustor exit have been reported when using glycerol with FB atomizer [17].

Prior studies have demonstrated combustor operation with glycerol including emissions reported at the exit plane only. In this research, a similar alternative fuel combustor with FB injector is used with the purpose of documenting gas temperature and emissions at various axial and radial locations inside the combustor to illustrate the flame structure. For a fixed heat release rate (HRR), different amounts of glycerol and methane are introduced to simultaneously combust both fuels. For a fixed fuel mix and total air flow rate, the effect of the air-to-liquid mass ratio (ALR) on the flame structures is investigated by varying the atomizing air flow rate. The following sections describe the experimental section following by results and conclusions.

2. Experimental setup

Fig. 3(a) shows the schematic of the experimental setup. After passing through filters and water traps, the compressed air is separated into primary air and atomizing air lines. Primary air enters the mixing channel through the plenum filled with marbles to breakdown large vortical structures. Methane is introduced into the mixing channel, and the fuel-air mixture or primary air pass through a section filled with steel wool to further homogenize the flow. This flow is introduced into the combustor through a swirler with axial curved vanes at 30 degree angle with respect to the transverse plane and swirl number of approximately 1.5. The fuel injector consists of a central fuel port with sidewise fuel inlet attachment and multiple openings around the peripheral region to introduce the atomizing air. Liquid fuel enters the injector via tubing connected with the injector holder and atomizing air is supplied from the bottom of the injector holder. The FB injection concept is implemented by placing a spacer of width $H = 0.25D$ between the fuel tube tip and injector discharge orifice as shown in Fig. 2. In this study, D = 0.5 mm and $H = 0.375$ mm.

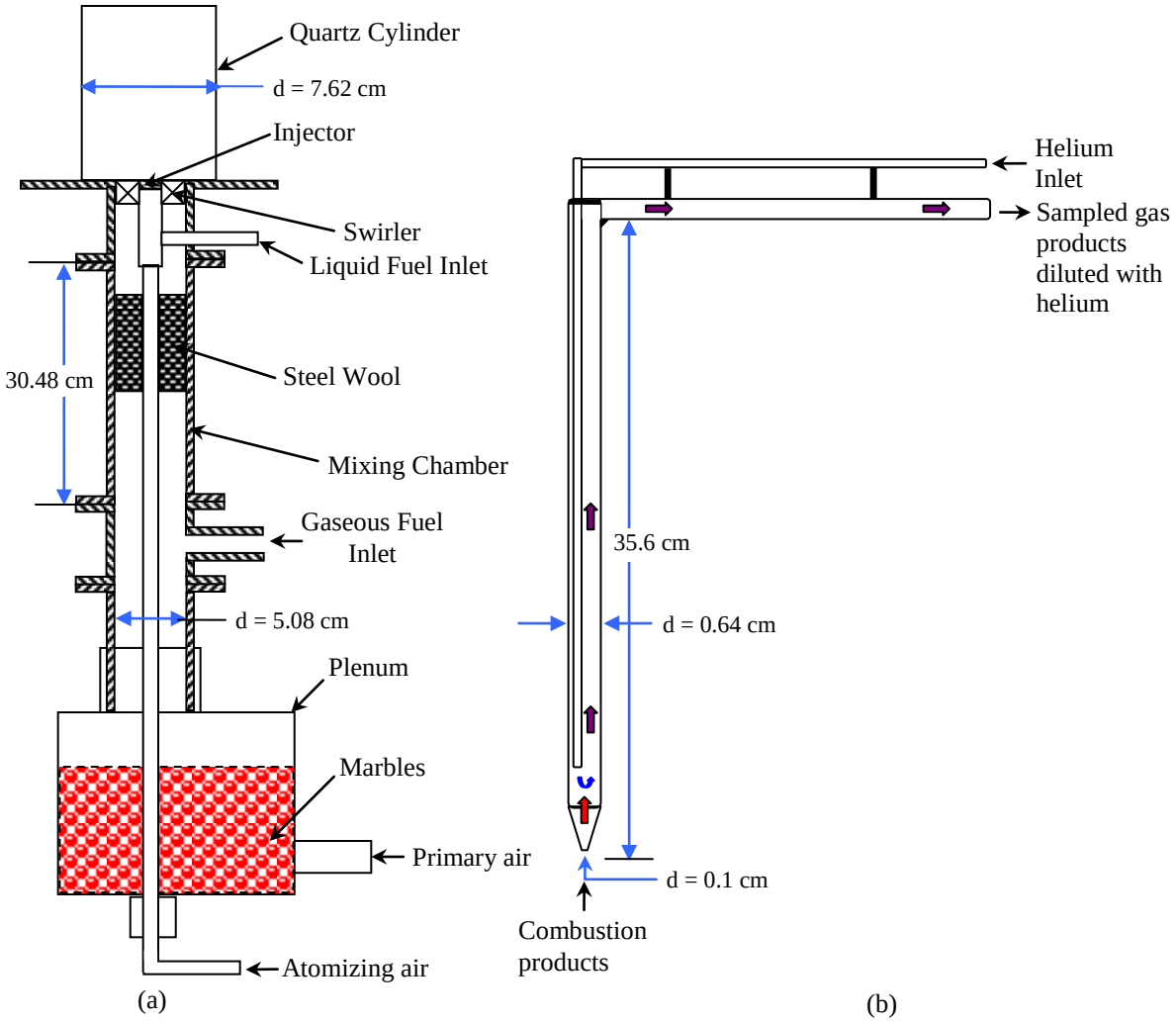

Fig. 3 (a) Experimental Setup Schematic and (b) Helium cooled sampling probe.

Mass flow rates of air and methane are controlled by Sierra Smart Track 2 Series 100 mass flow controllers with accuracy of ± 1% of the reading. Liquid fuel is supplied by a Cole Parmer high performance peristaltic metering pump (Model 7523-90) with an accuracy of ± 0.25% of the reading.

For characterizing the combustion products, R-type thermocouple insulated by ceramic tubes to minimize axial heat conduction was used to measure gas temperatures up to 2000 K. The thermocouple wire diameter was 0.25 mm and the bare bead diameter was 1.5 mm. The thermocouple temperature correction for radiation was estimated by using bead emissivity of 0.2 and air properties to approximate properties of the combustion products. The temperature distribution on the external surface of the quartz combustor was measured by an infrared camera (FLIR-T620) calibrated for temperature up to 2000 K. Free convection coefficient of 12 W/m^2-K for air was used to calculate the heat loss through the outside wall of the combustor. The CO and NOx emissions were measured using a Nova model 376WP gas analyzer with accuracy of ± 2 ppm. For enabling accurate measurements inside the flame zone, an in-house built, helium-cooled emission probe illustrated in Fig. 3(b) was utilized. This probe is made of two coaxial quartz tubes that enable mixing of combustion products and helium in the outer tube. Helium with its high specific heat

capacity reduces the temperature of the sampled combustion products to quench reactions near the probe tip. The helium flow rate is controlled by a needle valve to ensure that it does not exit through the probe tip to adversely affect the flame structure. The helium concentration in the sampled products was approximately 20% (by volume), and it was measured by a real-time Airsense High Speed Multi-component Gas Analyzer with accuracy of ± 2%. The sampled data were corrected for helium dilution and are reported as such. Gas temperatures and emissions measurements were taken at 10 axial planes with 11 transverse data at each axial plane. Transverse coordinate is defined as y-axis with the center at the axis of the combustor axis. Axial coordinate is defined as z-axis with the flow direction as the positive direction, and origin located at the dump plane of the combustor.

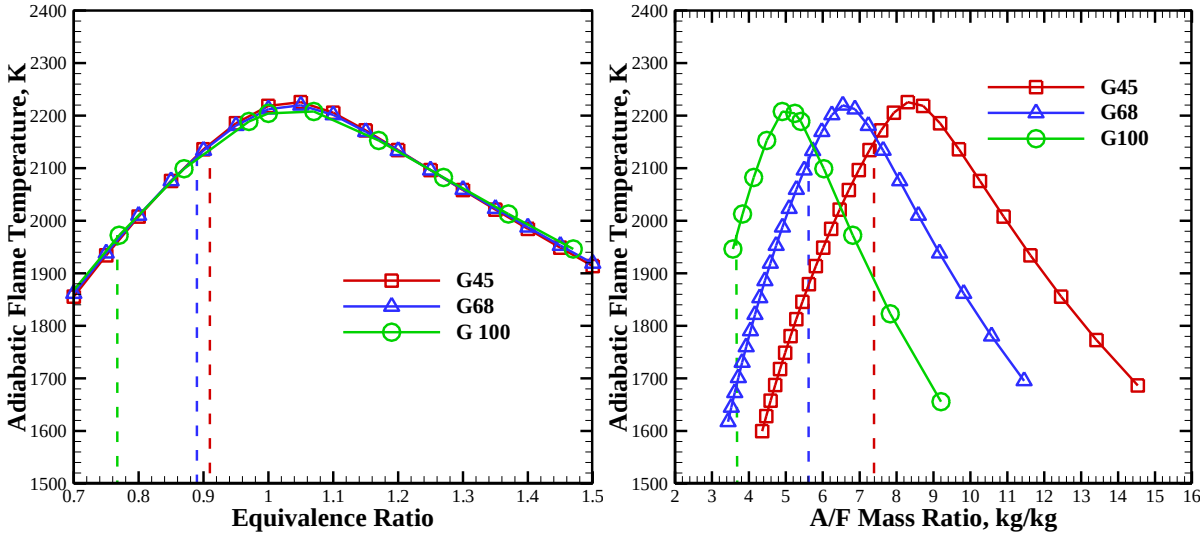

Fig. 4 Adiabatic flame temperatures as the function of (a) equivalence ratio and (b) air to fuel mass ratio.

The experiment is started with pure methane combustion to preheat the system and then, glycerol is gradually introduced into the combustion system through the FB injector. The total airflow rate, including primary airflow rate through the swirler and atomizing air through the injector, is kept constant at 150 standard liters per minute (slpm). For HRR = 7.9kW, the effect of air to liquid mass ratio is investigated for ALR = 1.47 and 2.23, for two fuel mixes, G45 and G68, where G45 signifies that 45% of the HRR is from glycerol and the rest is from methane. G100 case with HRR = 7 kW is also investigated for ALR = 1.13, which pertains to the cleanest glycerol flame conditions. G45, G68 and G100 fuel mix represents equivalence ratio of 0.91, 0.89 and 0.77, respectively. The Chemkin-pro software was used to compute the adiabatic flame temperature (T_{ad}) at equilibrium for the experimental conditions listed above, shown in Fig. 4. The computed T_{ad} is 2147 K, 2122 K and 1972 K, respectively, for G45, G68 and G100. Note that T_{ad} represents temperature achieved with complete combustion without heat loss from the combustor wall. However, the quartz combustor used in the present study results in unavoidable heat loss, which can be significant. In addition, the local flame temperature in the liquid fuel flame is related to the local equivalence ratio determined by fuel atomization processes affecting fuel droplet diameter, fuel pre-vaporization, and fuel-air mixing processes, which vary greatly throughout the combustor.

3. Results and discussions

3.1. Effect of Methane Addition

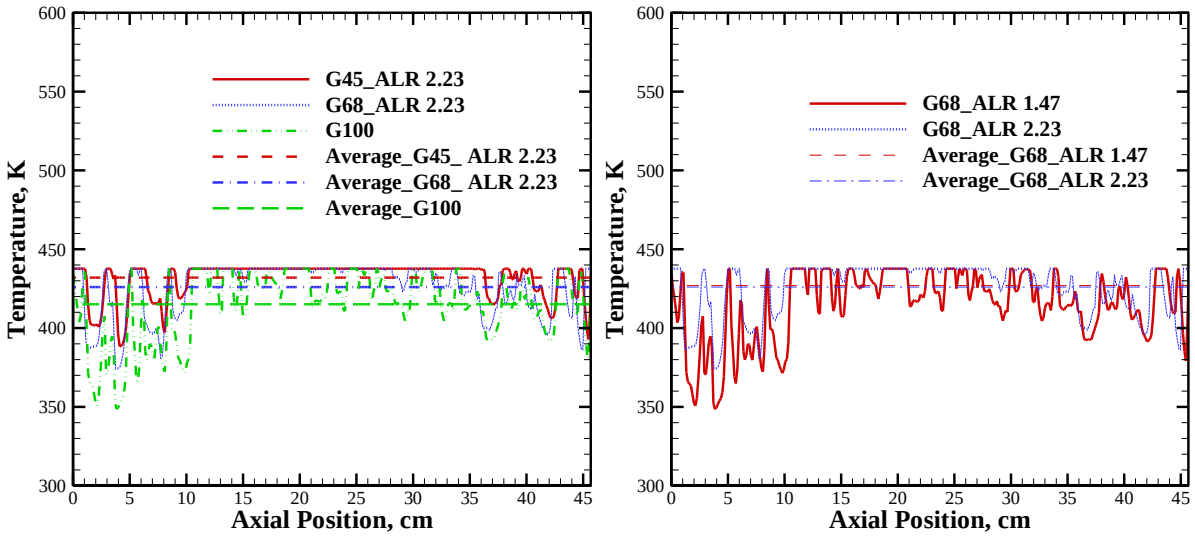

(a) (b)

Fig. 5 Surface Temperatures of the insulated combustor for (a) fuel composition and (b) ALRs.

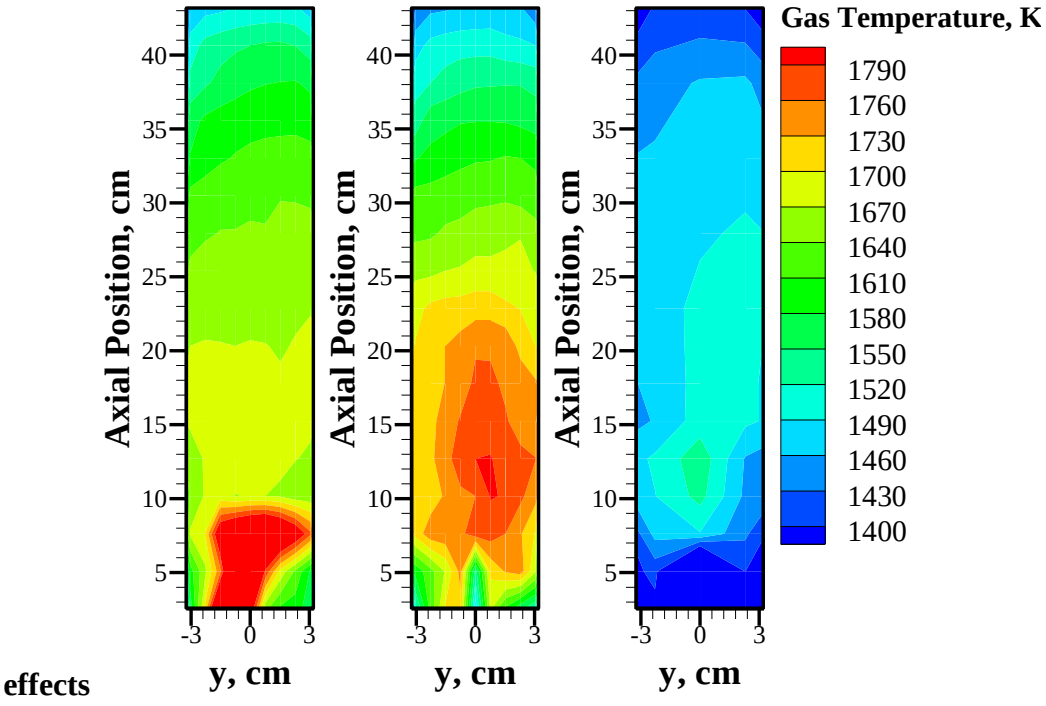

effects

(a) (b) (c)

Fig. 6 Gas temperature contour inside the combustor for (a) G45_ALR 2.23, and (b) G68_ALR 2.23 (c) G100.

Fig. 5(a) shows the axial profile of the surface temperature of the insulated combustor for G45, G68, and G100 flames. The average surface temperature is 432 K and 426 K respectively for G45, G68 flames and slightly lower (415) K for G100 flame. This plot helps in estimating heat loss from combustor to surroundings. Mean surface temperature close to the injector where fuel pre-vaporization and fuel-air mixing take place is slightly lower. The mean surface temperature is higher for z between 10 cm and 35 mm and it similar for all the three cases indicating relatively minor effects of the fuel mix. For z > 35 cm, the decrease in wall temperature is indicative of the heat loss to the ambient by natural convection and radiation.

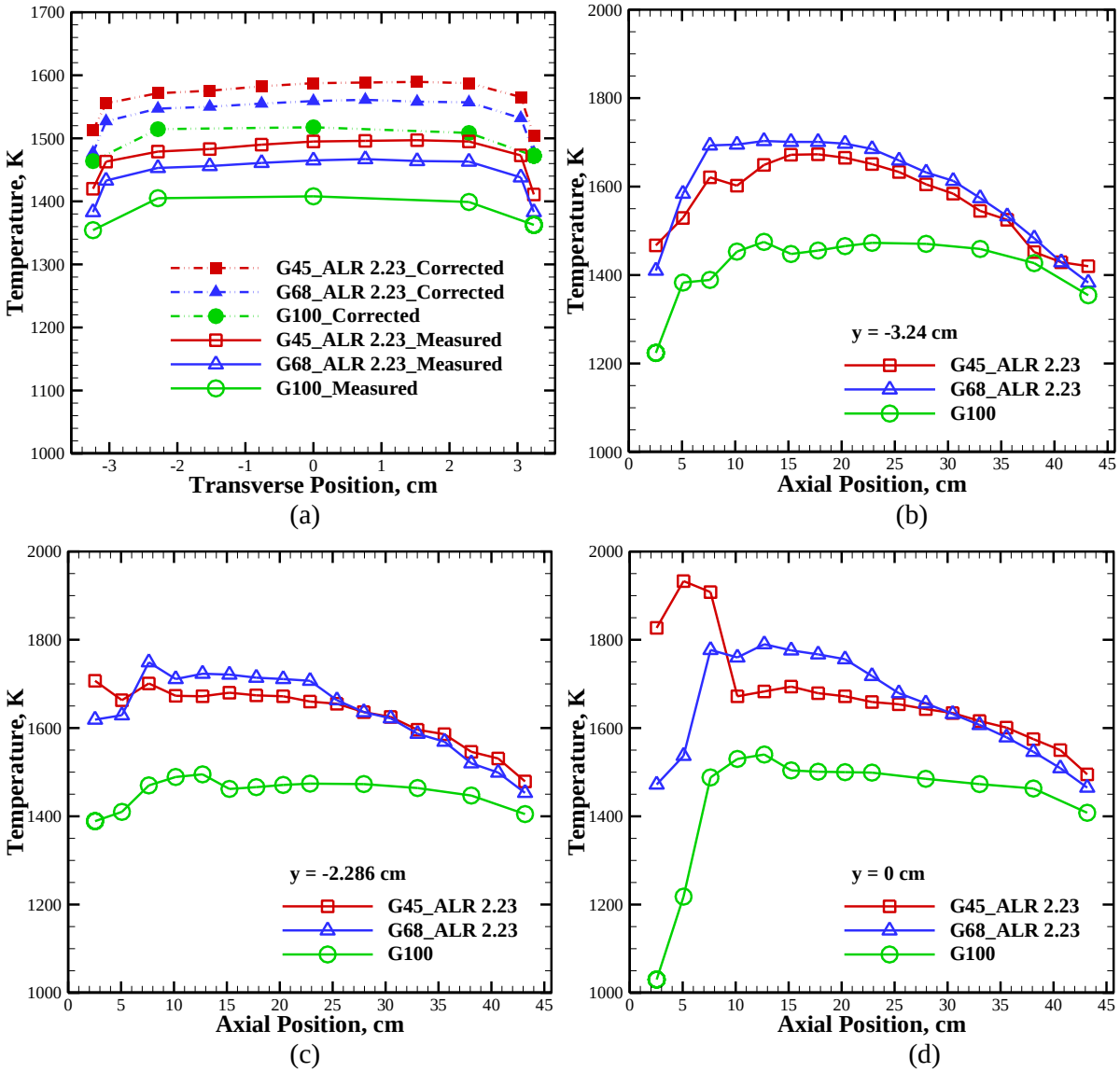

Fig. 7 Gas temperatures in the combustor for different fuel composition.

Fig. 6 shows contours of temperatures (uncorrected) inside the combustor for the flames with different fuel fix. For G45 flame, the reaction zone is closer to the injector exit where the temperature is highest. The reaction zone shifts downstream for G68 flame and a rather distributed reaction zone is observed for the G100 flame. These differences in the reaction zone location are attributed to the residence time needed to fully vaporize the liquid fuel. Methane combustion is expected to improve vaporization of glycerol spray, which results in a shorter reaction zone. In

contrast, G100 flame requires a greater distance to fully vaporize and combustion the fuel, which results in a longer, but low temperature reaction zone. Downstream of the reaction zone, the product gas temperature decreases because of the heat loss to the ambient as discussed above.

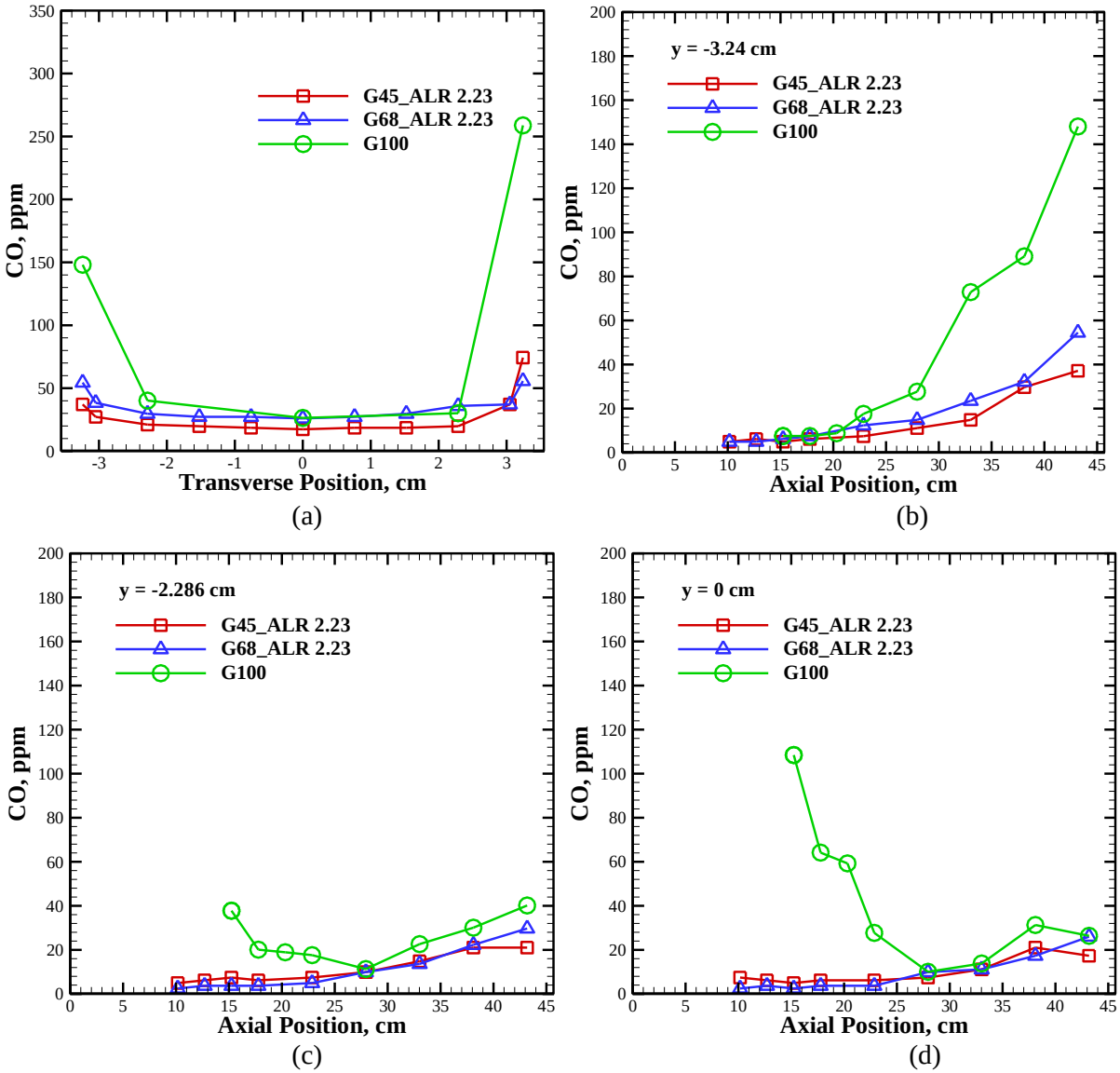

Fig. 8 CO concentrations in the combustor for different fuel composition.

Fig. 7(a) illustrates transverse profiles of product gas temperature at the combustor exit plane. Both uncorrected and radiation-corrected temperature data are presented, with corrections ranging from 90 K to 110K. Profiles show slightly higher temperature in the center of the combustor and temperature decreasing towards the wall because of the heat loss. For G45 and G48 fuel mixes, the HRR is the same (7.9 kW) which results in similar exit temperature profiles signifying complete combustion and/or minor effects of fuel mix on combustion. For G100, the HRR is slightly smaller (7.0 kW) and hence, product gas temperature at the combustor is also smaller than the previous two cases. Figs. 7(b)-(d) show axial profiles of gas temperature at three radial locations in the combustor. For G68 and G100 flames, a lower temperature is observed in the near injector region where fuel pre-vaporization zone and fuel-air mixing take place. Peak temperatures are observed in

the reaction zone where majority of the heat is released. At locations closer to the combustor exit, heat loss from the combustor exceeds any heat release by secondary reactions and thus, the temperature decrease in the flow direction. Matching axial profiles indicate that the differences in the fuel mix are confined to the near injector region, and that the fuel combust similarly with good glycerol pre-vaporization and fuel-air mixing. As discussed before, G45 and G68 flames are more intense compared to the G100 flame with an extended reaction zone. For G45 and G68 flames, heat released from methane combustion increases the temperature in the near field and provides thermal feedback for faster pre-vaporization of glycerol.

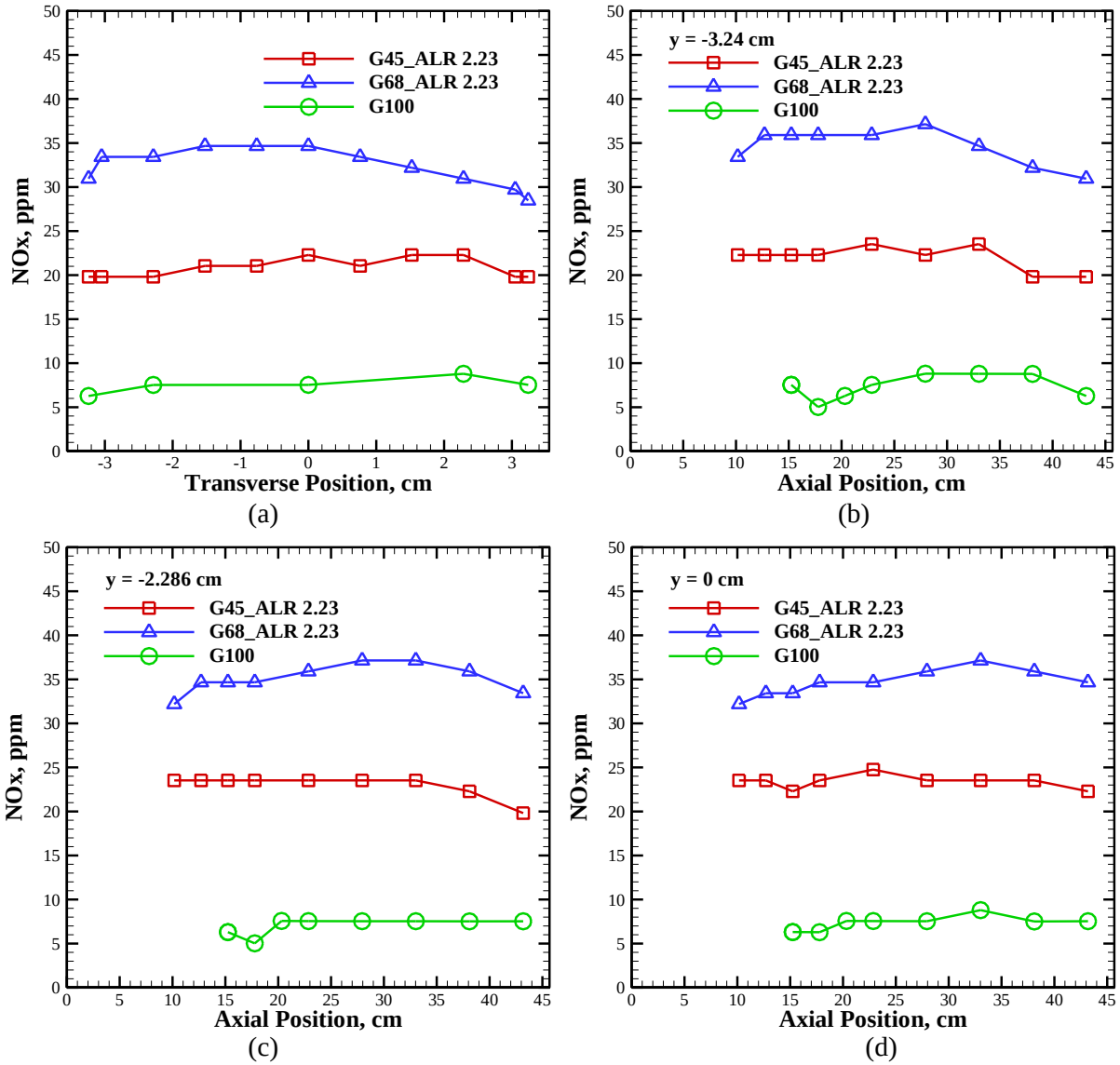

Fig. 9 NOx concentrations in the combustor for different fuel composition.

Fig. 8(a) compares the radial profiles of CO emissions at the combustor exit. For all three flames, the CO emissions in the 2-digit ppm range which is very low. Emissions are lowest in the center region and they increase near the wall where thermal quenching would take place. For G100 flame, much higher CO emissions near the wall could result from larger droplet hitting the wall and combusting only partially. Figs. 8(b)-(d) show axial profiles of CO emissions at several transverse locations in the combustor. G45 and G68 flames show extremely low CO emissions throughout the

combustor, which is consistent with the reaction zone located closer to the injector exit. G100 flame has generally higher CO emissions at the combustor center CO emissions, decreasing in the flow direction where oxidation reactions take place. However, CO emissions at y = -3.24 cm or near the wall increase in the flow direction, suggesting that larger droplets reaching the combustor periphery might not undergo complete combustion. This situation can be avoided by utilizing thermal feedback from combustion of small amounts methane introduced in the combustor. In any case, results demonstrate that with FB injector it is possible to cleanly burn glycerol without heating or pre-processing it.

Fig. 9(a) shows the radial profile of NO_x emissions at the combustor exit plane and Fig. 9(b)-(d) show the axial profiles of NO_x emission at various transverse locations for the three flames. Emissions samples were taken between z = 10 cm and combustor exit plane. NO_x emissions, favoring the high temperature mechanism, are higher for flames with methane as part of the fuel than those from the single fuel (glycerol) combustion. Local NO_x emissions from G45 flame are lower than those from G68 flame. This result is explained by the shorter high temperature reaction zone of the G45 flame. For G100 flame, the reaction extends the length of the combustor however reaction zone temperatures are also lower. Thus, the resulting NO_x emissions for G100 flame are much lower than those from methane containing G45 and G68 flames. Still, the NO_x emission levels are very low for all three flames, and demonstrate the fuel flexible nature of the FB injector.

3.2. Effect of Air to Liquid Mass Ratio (ALR)

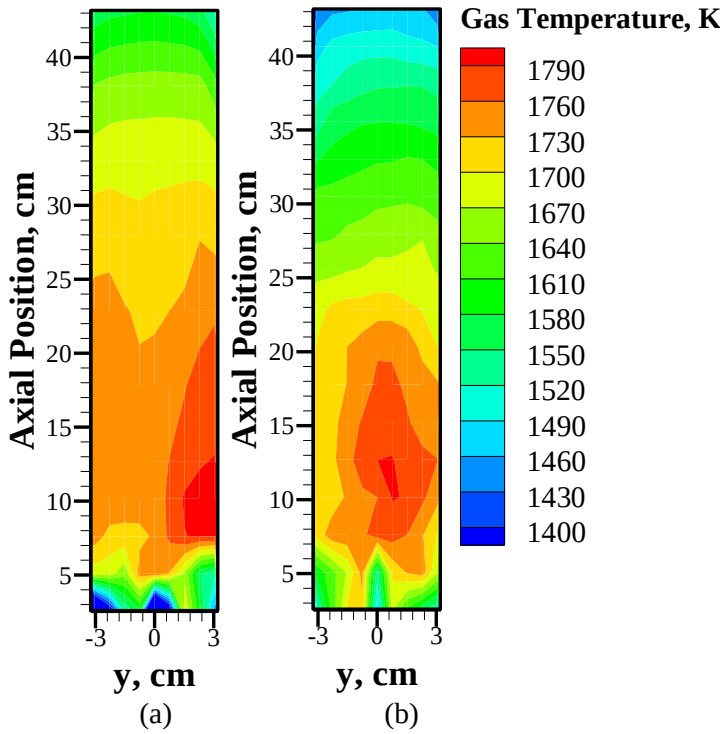

Fig. 10 Gas temperature contour inside the combustor for (a) G68_ALR 1.47 and (b) G68_ALR 2.23.

ALR does not affect the mean surface temperature of the combustor for G68 flames for fixed HRR as shown in Fig. 5(b). Fig. 10 shows contours of temperatures (uncorrected) inside the combustor for G68 flames with different ALRs. The reaction zone for ALR = 2.23 flame is shorter

and closer to the injector exit compared to the ALR = 1.47. This result is the direct outcome of the fuel-atomization, pre-vaporization, and fuel-air mixing processes, which are more effective for the higher ALR case. Consequently, reactions occur earlier in the high ALR flame releasing heat near the injector which further improves fuel pre-vaporization in return. Downstream of the reaction zone, temperature decreases in the flow direction because of heat loss from the combustor wall.

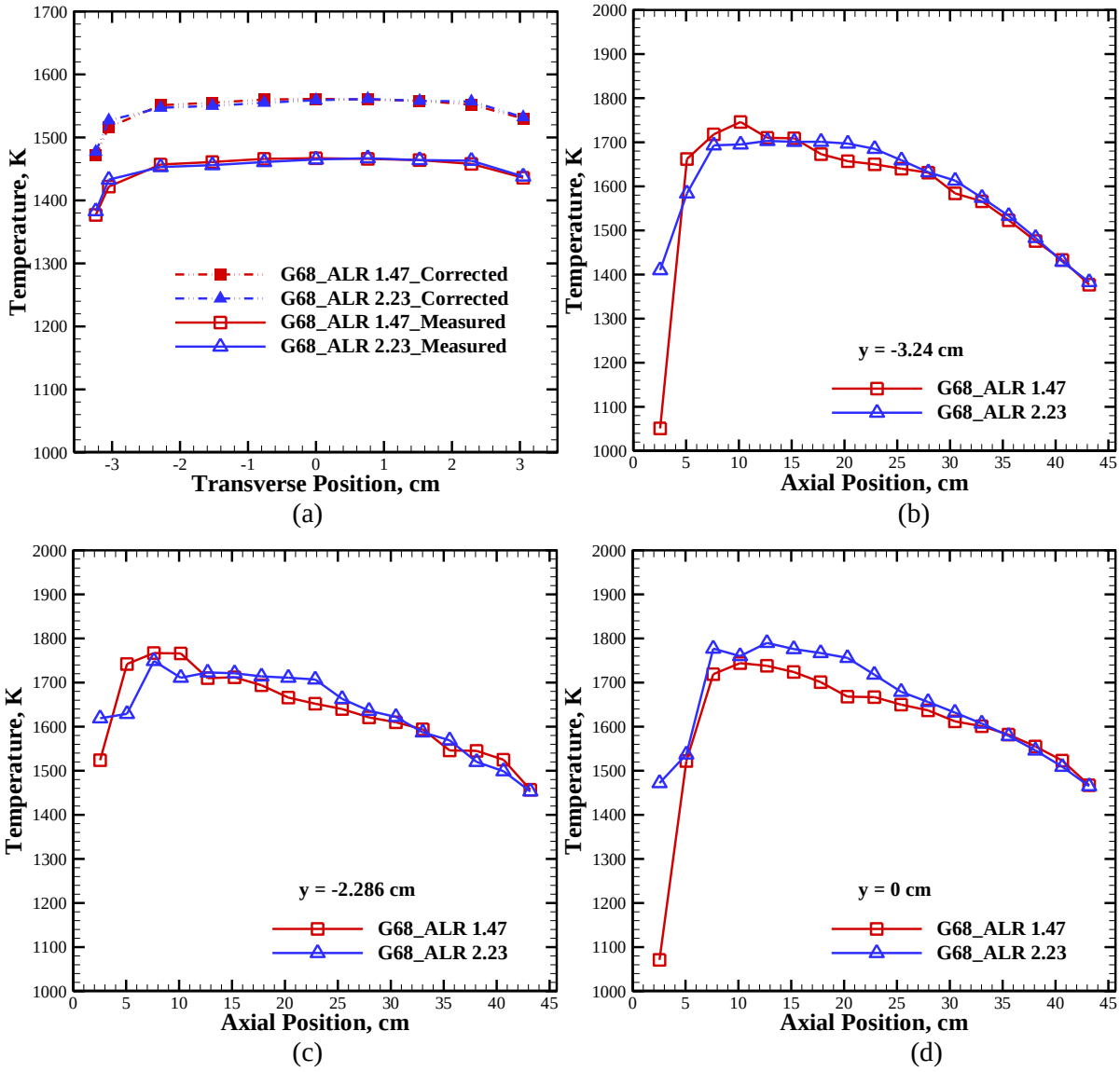

Fig. 11 Gas temperatures in the combustor for different ALRs with the same fuel composition.

Fig. 11(a) illustrates the effect of ALR on transverse profiles of uncorrected and radiation-corrected gas temperature; note that the temperature correction is about 94 K for both cases. Axial profiles of gas temperature in Figs. 11(b)-(d) show higher gas temperature in the very near field Z < 5 cm for higher ALR case compared to lower ALR case, indicating faster vaporization for the former case. In contrast, near the wall, slightly higher temperature is observed for the ALR = 1.47 flame. The likely reason is the greater number of larger droplets associated with the low ALR reaching the wall and combusting in diffusion mode. In general, differences in temperature distribution within the combustor have negligible effect on product gas temperature at the combustor exit.

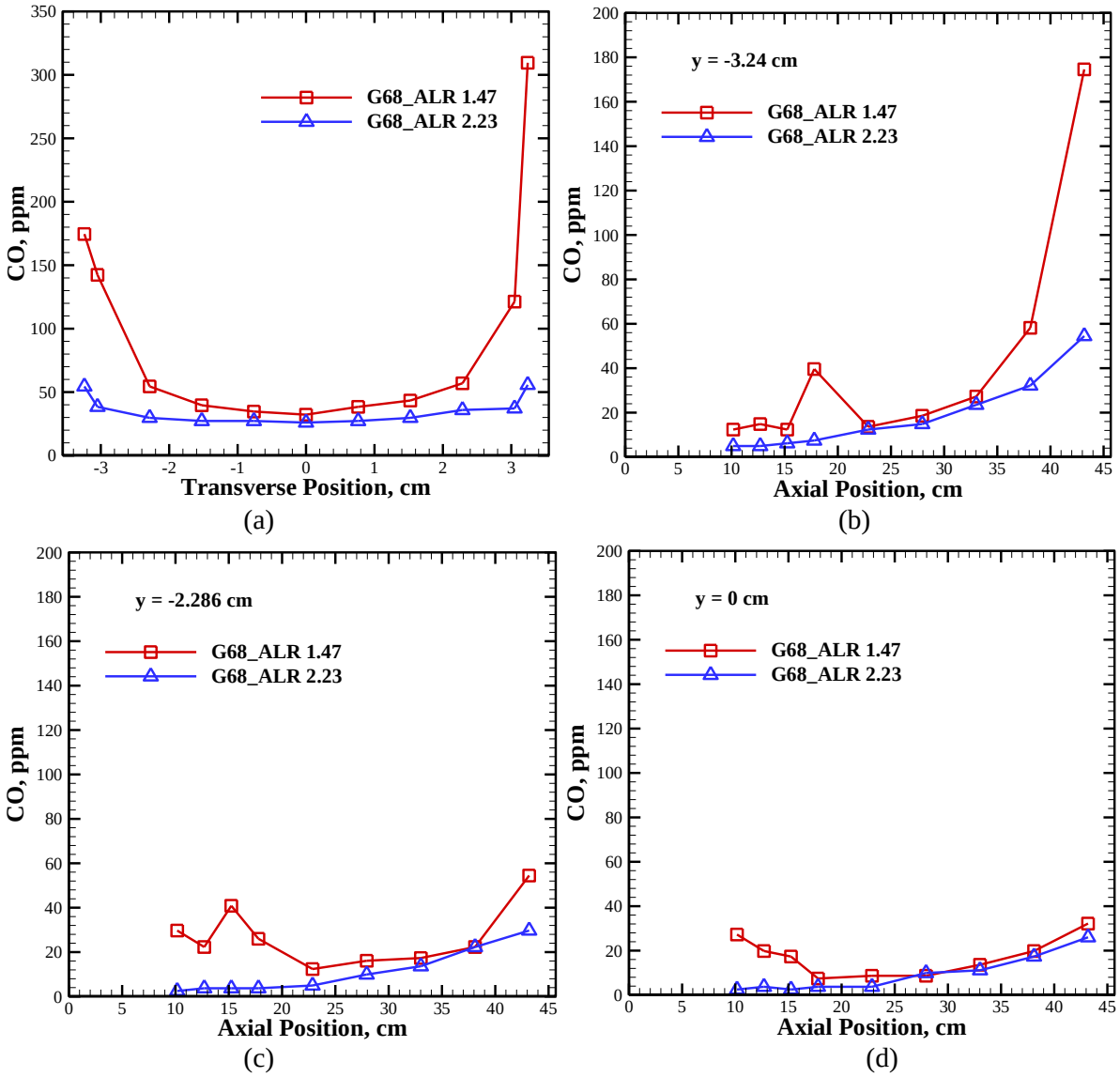

Fig. 12 CO concentrations in the combustor for different ALRs with the same fuel compostion.

Fig. 12(a) compares the radial profiles of CO emissions at the combustor exit to reveal the ALR effect for G68 flames. For both ALRs, CO emissions are low in the center region and increase towards the wall as discussed previously. For ALR = 1.47, CO emissions near the wall are much higher than those in the center region indicating larger droplets reaching the wall and burning partially and/or in diffusion mode. Fig. 12(b)-(d) show axial profiles of CO concentrations at different radial locations for the two flames. For both cases, CO concentrations from the two ALRs are low. CO concentrations for high ALR flame are lower mainly because of the higher local gas temperatures. For all cases, the spacially-averaged CO levels are low.

Fig. 13(a) shows the ALR effect on the radial profile of NO_x emissions at the combustor exit plane and Fig. 13(b)-(d) show the axial profiles of NO_x emission at various transverse locations for different ALRs. NO_x emissions are relatively higher for the higher ALR case, which is consistent with temperature measurements. Finer droplets produced for higher ALR case are vaporized fast and mix quickly with air to release heat in a relative intensified region with higher local temperatures. Overall, for both ALRs, NO_x emissions are low indicating good atomization by FB

injector. Further improvements in emissions performance could be achieved by optimizing geometric parameters (D and/or H) of the injector.

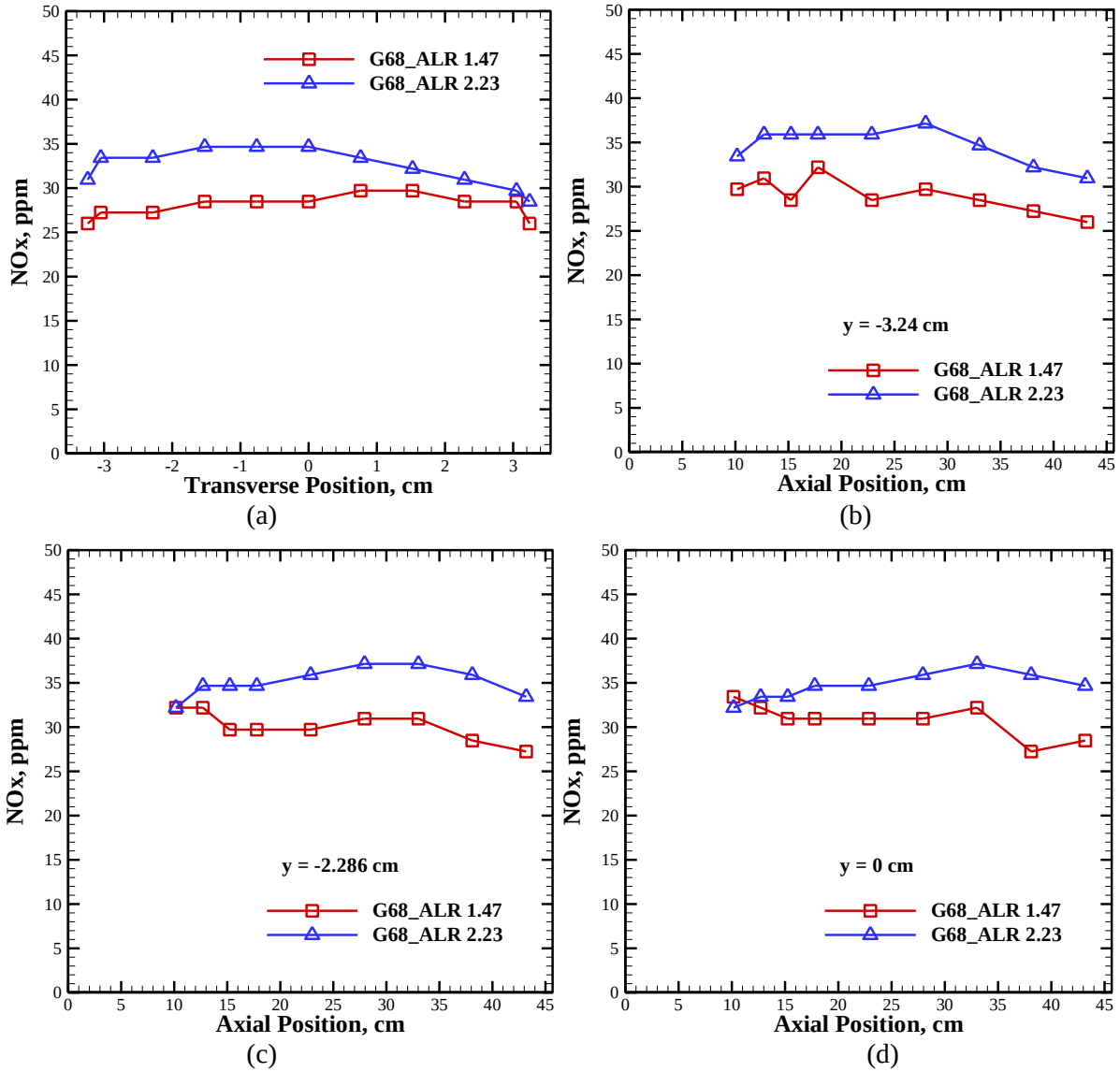

Fig. 13 NOx concentrations in the combustor for different ALRs with the same fuel compostion.

3.3. Droplet size and lifetime characteristics

As discussed above, all of the flames investigated with FB injector are clean producing low CO and NOx emissions. Introduction of methane in the combustor improves pre-vaporization of glycerol droplets produced by the injector. Detailed measurements by Simmons et al [10] using a Phase Doppler Particle Analyzer (PDPA) showed that glycerol droplets produced by FB atomizer have flow-weighted Sauter Mean Diameters (SMD) of 35μm and 40 μm at z = 10 cm, respectively for G48 and G68 flames. These results are introduced to further evaluate the evaporation time and the critical diameter (D_c) of the droplets using a simple droplet lifetime model [18]. The critical diameter is defined as the maximum diameter of the droplet which can completely evaporate in the pre-vaporization and fuel-air mixing zone near the injector orifice. The axial velocity of 12 m/s previously measured for most of the droplets is utilized to predict D_c for the three fuels [18]. The

length of the pre-vaporization and fuel-air mixing zone of 10 cm, according to the gas temperature contours in Fig. 6 and Fig. 10, is chosen for the approximate evaluation. For G45 flame, the temperature in the glycerol vaporization zone is as high as 1600 K to 1800 K as shown in Fig. 6. In G68 flame, the temperature varies from 1000 K to 1800 K as shown in Fig. 10.

Fig. 14 illustrates the maximum diameter of the glycerol droplets that would evaporate completely in the pre-vaporization for the present study. Evidently, for G45 flame, droplets of around 35 µm, containing most of the fuel mass, are smaller than the critical droplet diameter D_c. Thus, complete pre-vaporization of most of glycerol can be expected to occur before combustion in the near field. For G68 flame, when pre-vaporization zone temperature is below 1280 K, droplets of 40 µm diameter could not evaporate completely. From Fig. 10, it is evident that methane combustion results in reaction zone temperature of up to 1800 K, which is sufficient to completely pre-vaporize glycerol droplets. This simple analysis suggests that glycerol droplets with most of the fuel mass would pre-vaporize and burn in premixed combustion mode to yield low CO and NOx emission.

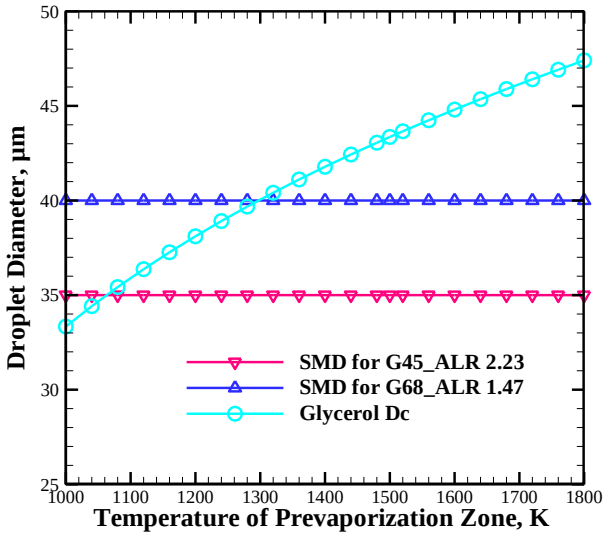

Fig. 14 Critical droplet diameters based on the prevaporization zone length (PZL) of 10 cm at droplet RMS axial velocity of 12m/s.

4. Conclusions

In this study, low-emission combustion of glycerol/methane has been achieved by utilizing a fuel-flexible FB injector to yield fine droplets of highly viscous glycerol. Heat released from methane combustion further improves glycerol pre-vaporization and thus its clean combustion. Methane addition results in an intensified reaction zone with locally high temperatures near the injector exit. Reduction in methane flow rate elongates the reaction zone, which leads to higher CO emissions and lower NO_x emissions. Similarly, higher ALR improves atomization and fuel pre-vaporization and shifts the flame closer to the injector exit. In spite of these internal variations, all fuels produced similar CO and NO_x emissions at the combustor exit. Results show that FB concept provides low emissions with the flexibility to utilize gaseous and highly viscous liquid fuels that are difficult to atomize using conventional techniques.

Acknowledgments

This research was supported by the US Department of Energy Award EE0001733.

References

[1] Dasari, M.A., P.P. Kiatsimkul, W.R. Sutterlin, and G.J. Suppes, "Low-pressure hydrogenolysis of glycerol to propylene glycol," *Applied Catalysis A: General*, Vol. 281, No. 1-2, 2005, pp. 225-231.

[2] Demirbas, A., "Conversion of biomass using glycerin to liquid fuel for blending gasoline as alternative engine fuel," *Energy Conversion and Management*, Vol. 41, No. 16, 2000, pp. 1741-1748.

[3] Naresh Pachauri, Brian He, "Value-added Utilization of Crude Glycerol from Biodiesel Production: A Survey of Current Research Activities", *ASABE Meeting Paper No*. 066223, Portland, Oregon, 2006.

[4] Wang, K., M.C Hawley, and S.J. DeAthos, "Conversion of glycerol to 1,3-propanediol via selective dehydroxylation," *Industrial and Engineering Chemistry Research*, Vol. 42, No. 13, 2003, pp. 2913-2923.

[5] Ito, T., Y. Nakashimada, K. Senba, T.Matsui, and N. Nishio, "Hydrogen and ethanol production from glycerol-containing wastes discharged after biodiesel manufacturing process," *Journal of Bioscience and Bioengineering*, Vol. 100, No. 3, 2005, pp. 260-265.

[6] López, J., Santos, M., Pérez, M. and Martín, M., "Anaerobic digestion of glycerol derived from biodiesel manufacturing," *Bioresour. Technol.*, Vol. 100, 2009, pp. 5609–5615.

[7] McNeil, John, Day, Paul and Sirovski, Felix, "Glycerine from biodiesel: The perfect diesel fuel," *Process Safety and Environmental Protection*, Vol. 90, No. 3, 2012, pp. 180-188.

[8] B. Metzger, "Glycerol Combustion," *M.S. Thesis*, Mechanical Engineering Dept., North Carolina State University, 2007.

[9] Myles D. Bohon, Brian A. Metzger, William P. Linak, Charly J. King and William L. Roberts, *Proceedings of the Combustion Institute*, Vol. 33, 2010, pp. 2717–2724.

[10] Simmons, B.M., "Atomization and Combustion of Liquid Biofuels," *Ph.D. Dissertation*, Mechanical Engineering Dept., Univ. of Alabama, Tuscaloosa, AL, 2011.

[11] Alfonso M. Gañán-Calvo, "Enhanced liquid atomization: From flow-focusing to flow-blurring," *Applied Physics Letters*, Vol. 86, No. 21, AIAA, Sevilla, Spain, 2005, pp. 2141-2142.

[12] Lulin Jiang, Pankaj S. Kolhe, Robert P. Taylor, and Ajay K. Agrawal, 2012, "Scalar Measurements in a Combustor Operated on Alternative Liquid Fuels", *51st AIAA Aerospace Sciences Meeting Including the New Horizons Forum and Aerospace Exposition*, January 9-12, Nashville, Tennessee.

[13] Simmons, B.M., Panchasara, H.V. and Agrawal, A.K., "A comparison of air-blast and flow blurring injectors using phase Doppler particle analyzer techniques," *ASME Conference Proceedings*, 2009 (48838), pp. 981-992.

[14] Simmons, B.M. and Agrawal, A. K., "Spray characteristics of a flow blurring atomizer," *Atomization and Sprays*, Vol. 20, No. 9, 2010, pp. 821-825.

[15] Panchasara, H., Sequera, D., Schreiber, W. and Agrawal, A.K., "Combustion performance of a novel injector using flow-blurring for efficient fuel atomization," *Journal of Propulsion and Power,* Vol. 25, No. 4, 2009, pp. 984-987.

[16] Benjamin M Simmons and Ajay K. Agrawal, "Flow Blurring Atomization for Low-Emission Combustion of Liquid Biofuels," *Combustion Science and Technology,* Vol. 184, No. 5, pp. 660-675.

[17] Benjamin M. Simmons, Pankaj S. Kolhe, Robert P. Taylor, and Ajay K. Agrawal, "Glycerol Combustion using Flow-Blurring Atomization," *the 2010 Technical Meeting of the Central States Section of The Combustion Institute*, Champaign, Illinoi, 2010.

[18] Turns, S.R., *An Introduction to Combustion Concepts and Applications*, 2nd ed., McGraw-Hill Higher Education, USA, 2000, pp. 376-378.

Measurements in a Combustor Operated on Alternative Liquid Fuels

Journal:	*50th AIAA Aerospace Sciences Meeting Including the New Horizons Forum and Aerospace Exposition*
Manuscript ID:	Draft
luMeetingID:	1964
Date Submitted by the Author:	n/a
Contact Author:	Agrawal, Ajay

Measurements in a Combustor Operated on Alternative Liquid Fuels

Lulin Jiang[1], Pankaj S Kolhe[2], Robert P Taylor[3] and Ajay K Agrawal [4]
The University of Alabama, Tuscaloosa, AL, 35487

Diminishing fossil fuel resources, ever-increasing energy cost, and the mounting concerns for environmental emissions have precipitated worldwide research on alternative fuels. Present study demonstrates low-emission combustion of diesel, biodiesel and straight vegetable oil (VO) is a dual-fuel burner employing flow blurring (FB) injector concept for fuel atomization. Measurements of temperature and CO and NOx emissions are acquired at various axial and radial locations within the combustor. A custom-designed thermocouple probe and a helium product gas sampling probe are employed to obtain the measurements. Infra-red images to depict combustor wall temperatures and visual flame images to demonstrated clean combustion are also presented. Results show that the FB injector ensured fine atomization of all three fuels irrespective of significant differences in their kinematic viscosity and surface tension properties.

I. Introduction

The limited fossil fuel resources and the dramatically increasing demand for energy have become major issues for our modern world leading to discovery and exploration of ways to utilize alternative fuels to replace the conventional nonrenewable fuels. Biodiesel is one of the most common, domestically produced alternative biofuels to satisfy part of energy needs. Biodiesel can easily replace diesel fuel in existing combustion devices because of similar fuel properties[1-5]. Biodiesels are produced through the transesterification process of triglycerides from source oils such as vegetable oils (VO) and/or animal fats. Transesterification of source oil into biodiesel decreases the kinematic viscosity by almost an order of magnitude as shown in Table 1. The low viscosity biodiesel can be finely atomized by existing fuel injection systems, e.g., an air-blast (AB) injector, and thus to achieve relatively clean combustion with low emissions of carbon monoxide (CO), nitric oxides (NOx), and particulate matter (PM). Previous research shows reductions in CO and PM emissions of biodiesel blends compared to those from diesel[6-7]. However, many reports show that with existing fuel injection systems, the NOx emissions of biodiesel are higher than those of diesel[8-11]. Production of biodiesel from source oils via transesterification consumes substantial energy and generates glycerol as byproduct. Therefore, present study focuses on utilizing an efficient atomization injector to burn biodiesel more cleanly as well as directly combust straight VO (soybean oil in this study) with clean combustion to enhance the economic and environmental benefits of utilizing liquid biofuels.

Table.1 Physical properties of diesel, biodiesel and vegetable oil.

Property	Diesel	Biodiesel	Vegetable Oil
Density [kg/m^3], 25°C	834.0 ± 9.2	880.0 ± 8.3	925.0 ± 8.6
Kinematic Viscosity [mm2/s], 25°C	3.88 ± 0.02	5.61 ± 0.02	53.74 ± 0.22
Low Heating Value (LHV) [MJ/kg]	44.6	37.66	37
Auto-ignition Temperature[°C]	260	177	406
Vaporization Temperature [°C]	160-370	100-170	327 °C
Surface Tension at 25 °C [mN/m]	28.2 ± 0.6	31.1 ± 0.6	30.1 ± 0.6

[1] Graduate Assistant, Mechanical Engineering Department, ljiang5@crimson.ua.edu, AIAA Student Member.
[2] Post Doctoral Researcher, kolhe001@crimson.ua.edu, and Senior AIAA member.
[3] Professor, Mechanical Engineering Department, btaylor2@eng.ua.edu.
[4] Robert F. Barfield Endowed Chair Professor, aagrawal@eng.ua.edu, Associate Fellow of AIAA.

The working principle of AB injector illustrated in Fig. 1 involves introducing high velocity air through the injector to create shear layer instabilities, which break-up the fuel flow into droplets[12]. The shear layer instabilities are suppressed by high kinematic viscosity, which limits the ability of the AB injector to produce a spray with fine droplets for fuels such as VO[13]. Recently, Gañán-Calvo (2005) reported the concept of flow blurring (FB) injection claimed to create "five to fifty times" more fuel surface area than a plain-jet AB atomizer[14]. The FB injection concept is based on aerodynamically creating two-phase flow near the injector exit as shown in Fig. 2. The FB injector consists of a fuel tube and an exit orifice both of inside diameter, D. The fuel tube exit and orifice are separated by gap, H. For H < 0.25D, the atomizing air mixes with fuel upstream of the fuel tube tip to create a two-phase flow. Through the injector orifice, the two-phase flow is subjected to rapid decrease in pressure, leading to expansion and breakup air bubbles yielding spray with fine droplets. Previous detailed phase Doppler particle analyzer (PDPA) measurements show that the FB injector produces finer spray than that produced by an AB injector at the same atomizing air and liquid mass flow rates. Compared to AB atomizer, the FB injector requires lower energy input since it incurs a lower pressure drop in the atomizing air line[15-16]. For a given overall equivalence ratio, heat release rate (HRR) and atomizing air-to-liquid fuel ratio (ALR), FB atomization in a swirl-stabilized combustor resulted in three to five times lower CO and NOx emissions in diesel and kerosene flames compared to those with AB atomization[17]. In addition, lower CO and NOx emissions of diesel, biodiesel were reported at the exit plane of a combustor with FB injector compared to combustion with AB injector[18]. Emissions measurements at the exit plane of the combustor have also demonstrated clean combustion of VO with FB atomizer[18].

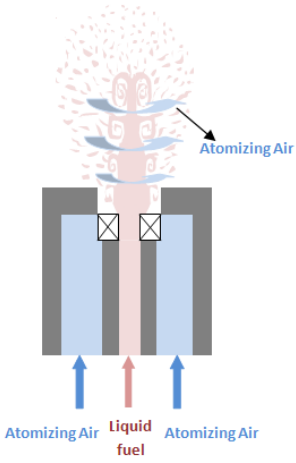

Figure 1. Working principle of air blast injector.

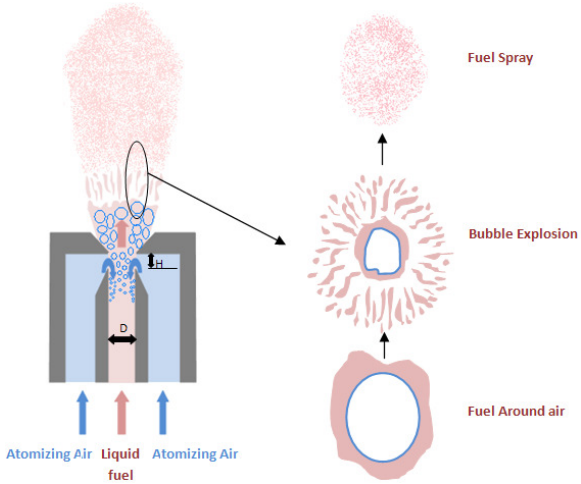

Figure 2. Working principle of the flow blurring injector.

II. Objectives

The objective of this research is to compare the combustion performances of diesel, biodiesel and straight VO through measurements of flame temperatures, CO and NOx emissions, and surface temperatures of the quartz combustor. Custom-designed thermocouple and gas sampling probes are utilized to obtain measurements at several axial and radial positions to compare the performance for a fixed heat release rate. Experimental setup, results and discussion and conclusions are presented in the following sections.

III. Experimental Setup

Figure 3 shows the schematic of the experimental setup. Primary air enters into the mixing pipe connected to the plenum with marbles in it to breakdown large vortical structures. Methane is introduced into the mixing pipe during startup, and the fuel-air mixture or primary air pass through a section filled with steel wool to further homogenize the flow. A swirler with axial curved vanes at 30 degree angle and the swirler number of approximately 1.5 is used to promote secondary atomization, enhance fuel-air mixing, and improve flame stabilization in the combustor. Fuel injector consists of a central fuel port with sidewise fuel inlet attachment and multiple holes around the peripheral region to introduce the atomizing air. Liquid fuel enters the system via tubing connected with the injector holder and atomizing air is introduced from the bottom of the injector holder. The FB injection concept to gain fine atomization is implemented by introducing a spacer of width H = 0.25D between the fuel tube and injector exit orifice as shown in Figure 2. In this study, the fuel tube and injector orifice ID is 1.5 mm, which required H = 0.375 mm.

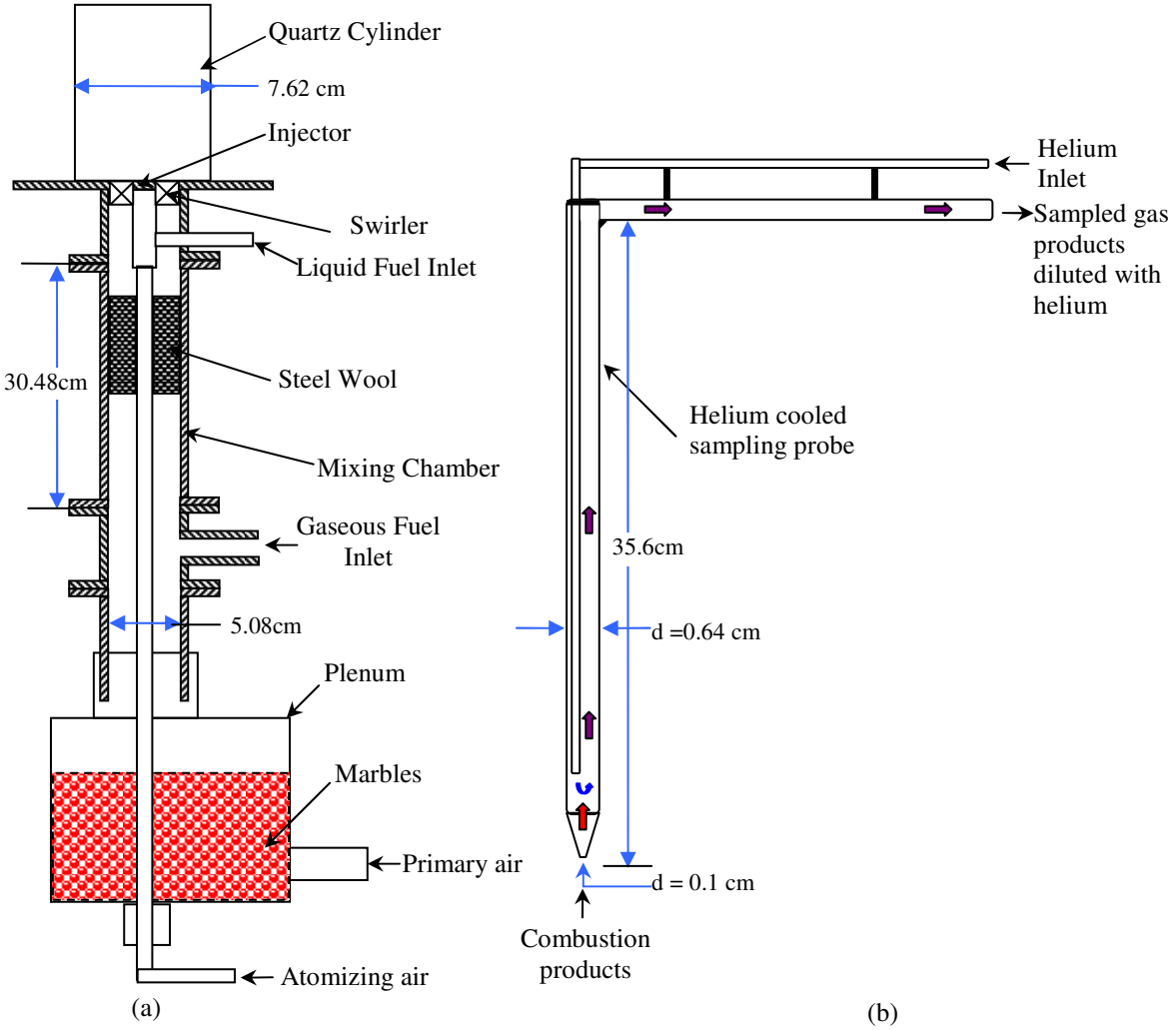

Figure 3. (a)Experimental Setup Schematic and (b) Helium cooled sampling probe

Compressed air is supplied by an air compressor and moisture in air is eliminated while air travels through filters and water traps. Then air is separated into primary air and atomizing air flow lines to meet the experimental requirements. Mass flow rates of air and methane are controlled by Sierra Smart Track 2 Series 100 mass flow controllers with accuracy of ± 1%. Liquid fuel is pumped by a Cole Parmer high performance peristaltic metering pump (Model 7523-90) with an accuracy of ± 0.25%.

The CO and NOx emissions are measured using a Nova model 376WP gas analyzer with accuracy of ± 2 ppm. For enabling accurate measurements inside the flame zone, an in-house built, helium-cooled emission probe illustrated in Fig 3b was utilized. This probe is made up of two coaxial quartz tubes that enable mixing of combustion product and helium in the outer tube. Helium with its high specific heat capacity cools down the sampled combustion products to quench reactions near the probe tip. The helium flow rate is controlled by a needle valve to ensure that it does not exit through the probe tip to adversely affect the flame structure. The helium concentration in the sampled products was approximately 20% (by volume), and it was measured by a real-time Airsense High Speed Multi-component Gas Analyzer with accuracy of ± 2%. The sampled data were corrected for helium dilution and are reported as such. A type-R thermocouple probe insulated by ceramic tubes to minimize axial heat conduction was used to measured temperature up to 2000 K[8]. The temperature data are reported without correcting for radiation. The temperature distribution on the external surface of the quart combustor was measured by an infrared camera (FLIR-T620) calibrated for temperatures up to 2000 K.

Experiment was started with methane combustion to preheat the combustor and thus, to supply heat to evaporating fuel spray when operation was gradually switched to liquid fuel combustion. The total airflow rate, including primary air through the swirler and atomizing air through the injector, was kept constant at 150 standard liters per minute (slpm). For comparison, the heat release rate (HRR) and air to liquid mass ratio (ALR) were kept constant; HRR = 7 kW and ALR = 3.0. The fuel flow rate is 11.3, 12.7 and 12.3 ml/min, respectively, for diesel, biodiesel and vegetable oil with respective equivalence ratio of 0.77, 0.76 and 0.79. The Chmkin-pro software was used to compute the adiabatic flame temperature (T_{ad}) at equilibrium for the experimental conditions listed above. Diesel fuel was represented by a four-component model denoted as DF1[19]. Biodiesel composition was taken from gas chromatography-mass spectroscopy measurements for soybean biodiesel[20]. The VO was represented using a five-component model[21]. Figure 4 shows that the calculated T_{ad} versus equivalence ratio plots for diesel, biodiesel and VO nearly overlap each other. For the present test conditions with fixed HRR, calculated T_{ad} of 2030 K, 2010 K and 2050 K, respectively, for diesel, biodiesel, and VO is within +/- 20 K for the three fuels. Note that T_{ad} could be achieved with complete combustion and without heat loss from the combustor wall. However, the quartz combustor used in the present study results in unavoidable heat loss, which can be significant. In addition, the local flame temperature in the liquid fuel flame is related to fuel atomization affecting droplet size in the spray, and fuel pre-vaporization and fuel-air mixing processes, which can vary greatly throughout the flame.

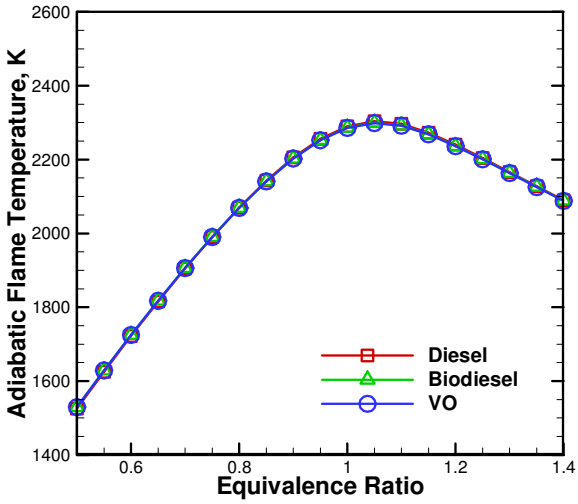

Figure 4. Calculated adiabatic flame temperature.

IV. Results and Discussion

Figure 5 shows visual flame images of diesel, biodiesel, and VO. All flames exhibit remarkably similar features in spite of the significant differences in their physical properties. The flame is stabilized in the downstream region at axial plane, z > 5.0 cm. Fuel preparation including primary atomization, fuel pre-vaporization and fuel-air mixing occurs in the dark near injector region, i.e., z < 5.0. Thus, the downstream reaction zone is dominated by the premixed mode. The diesel flame is encompassed between z = 6.0 cm and 15 cm, the biodiesel flame extends from z = 8 cm to 20 cm, while that for VO resides between z = 6.0 cm and 18 cm. From Figure 5(a), it is clear that diesel visual flame zone is relatively compact, intense and dominated with blue color indicating CH* chemiluminescence and clean burning lean premixed (LPM) combustion[22]. Figure 5(b) shows that biodiesel visual flame zone is slightly downstream, wider, and longer. The flame is stabilized farther downstream, possibly because of the higher fuel flow rate in this case to achieve the same HRR. Larger fuel droplets would also burn in the diffusion flame mode, marked by the orange glow observed in the downstream flame region[23-24]. Figure 5(c) shows the slender elongated VO flame zone dominated with blue CH* chemiluminescence. Note that, higher kinematic viscosity and surface tension properties of VO can be expected to increase population density of larger droplets. However, the droplets are sufficiently small to pre-vaporize and premix with air with the short residence time in the dark region near the injector exit.

Figure 6 shows combustor surface temperature contours measured by the infrared. These images are consistent with visual flame images, and help identify flame regions and reaction zones in the combustor. Primary air entrainment is limited in the center region, which would produce fuel-air mixtures closer to stoichiometric conditions and hence, higher reaction zone temperatures leading to higher combustor wall temperatures observed in Fig. 6. The temperature is highest around the axial plane z = 12 cm, which is located in the mid-section of the visual flames in Fig. 5. In this mid-section, larger fuel droplets vaporize and combust at high temperatures to produce locally higher NOx and CO concentrations. Similar results are obtained for all three fuels indicating that the reaction zone is relatively independent of fuel's physical properties. High combustor wall temperature would result in high heat loss by natural convection and radiation from the combustor to the ambient. For z > 12 cm, the combustor wall temperature decreases as combustion products homogenize by thermal mixing and because of the heat loss from the combustor wall as discussed above.

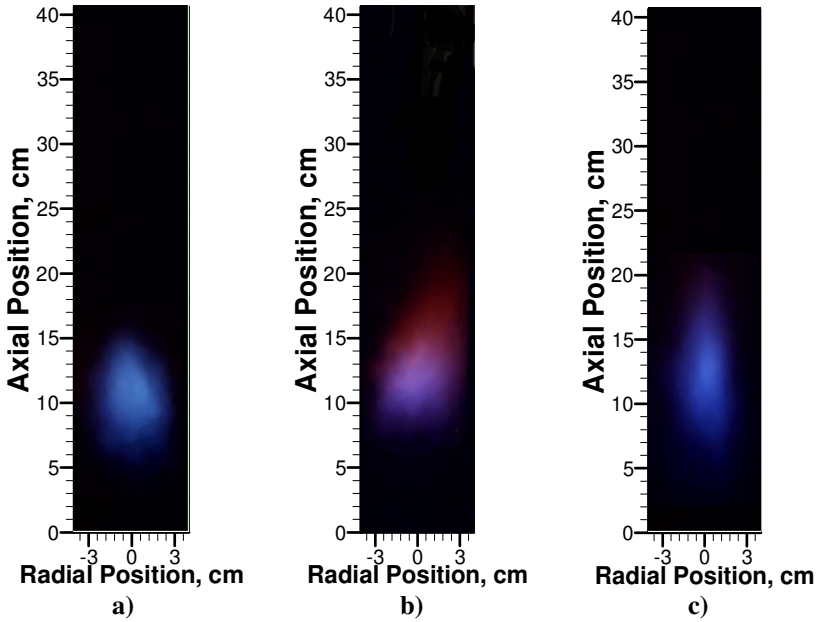

Figure 5. Flame images: a) diesel b) biodiesel c) VO.

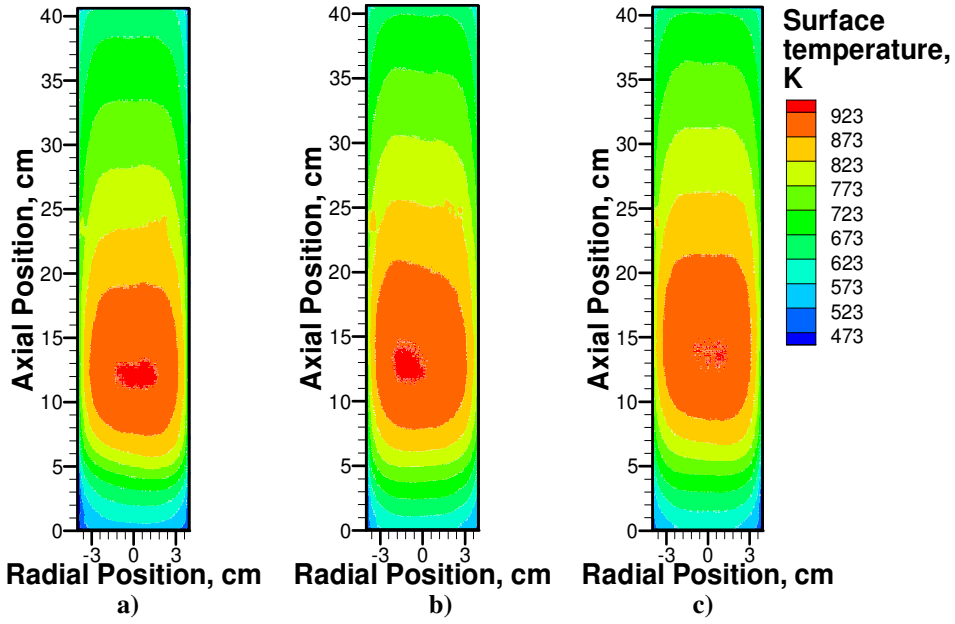

Figure 6. Infrared (IR) image contours of the combustor for a) diesel b) biodiesel c) VO.

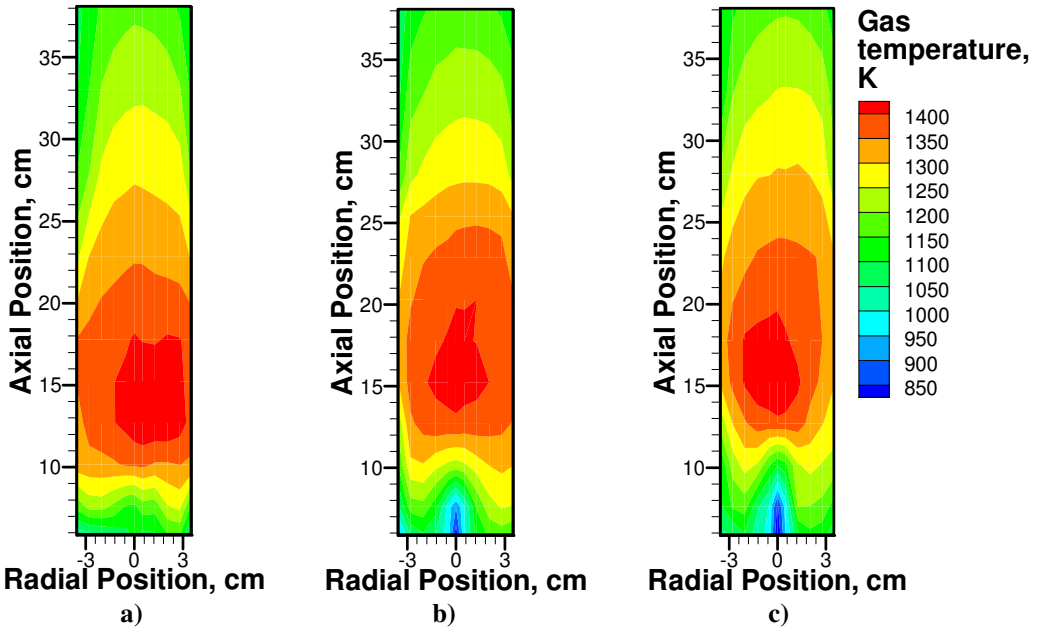

Figure 7. Gas temperature contours inside the combustor for a) diesel b) biodiesel c) VO.

Figure 7 shows contours of gas temperature (uncorrected) inside the combustor for the three flames. In agreement with the wall temperature contours, these results also show a high temperature reaction zone in the mid-section of the flame. In comparison with biodiesel and VO flames, the high temperature region for the diesel flame is slightly closer to the injector exit, indicating faster fuel pre-vaporization associated with smaller droplets for the latter case. Figure 8(a) shows radial profiles of product gas temperature at the combustor exit plane for diesel, biodiesel, and VO flames. As expected, the temperature slightly higher in the center region and decreases towards the combustor wall because of the heat loss. Temperature profiles for all three fuels are nearly identical because the fuel flow rate was chosen to provide the same HRR. Figures 8(b)-(d) compares axial profiles of product gas temperature at various radial locations of the combustor for the three fuels. Most of the heat is released in the flame zone to result in higher temperature at these locations. At locations closer to the combustor exit, the gas temperature decreases because of the heat loss to the ambient. For all three cases, temperature profiles are similar revealing that all fuel combust similarly with good prevaporization and fuel-air mixing. Inside the diesel flame, the peak temperature is reached slightly closer to the injector exit indicating faster fuel prevaporization associated with small fuel droplets. In general, similar temperature profiles with minor differences are found at various locations in the combustor, indicating that the FB injector yields fine spray in spite of the significant differences in fuel properties.

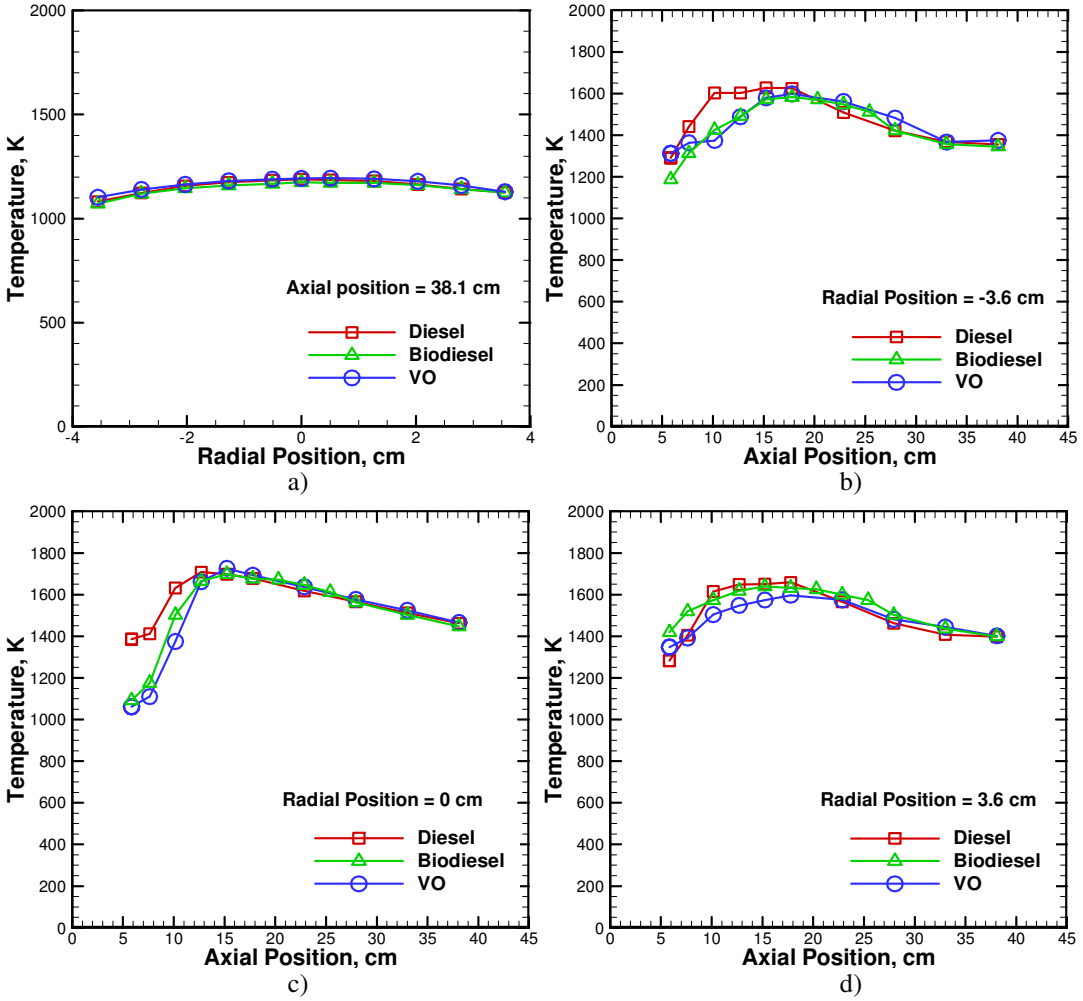

Figure 8. Comparisons of gas temperature inside the combustor for diesel, biodiesel and VO.

Previous studies show that diesel and biodiesel can be burnt with AB atomization with acceptable emission level, while straight VO produced unacceptably high emissions beyond the gas analyzer range[25]. However, FB atomizer used in this study shows that all three fuels can be combusted with low emissions. Figure 9 (a) shows the radial CO emissions profile at the combustor plane and Figs. 9(b)-(f) show axial profiles of CO emissions at radial location near combustor wall, mid radial location on either side of center, and centerline. For all cases, CO emissions from these three fuels are extremely low. The CO emissions of diesel and biodiesel are close to each other with slightly higher emissions for diesel. This result can be explained by the oxygen content in biodiesel favoring faster CO oxidation. The CO emissions from VO are higher than those from other fuels, possibly because of increased combustion in diffusion mode in the oxygen deficient center region containing larger droplets. High CO emissions measured near the injector exit for VO flames are erroneous readings resulting from suction of fuel droplets into the probe and subsequent combustion within the probe in diffusion mode. Overall, results show that CO emissions the lowest in the diesel flame and highest in the VO flame. For all the three fuels, the CO emissions are higher in the upstream reaction zone before decreasing by oxidation towards the combustor exit.

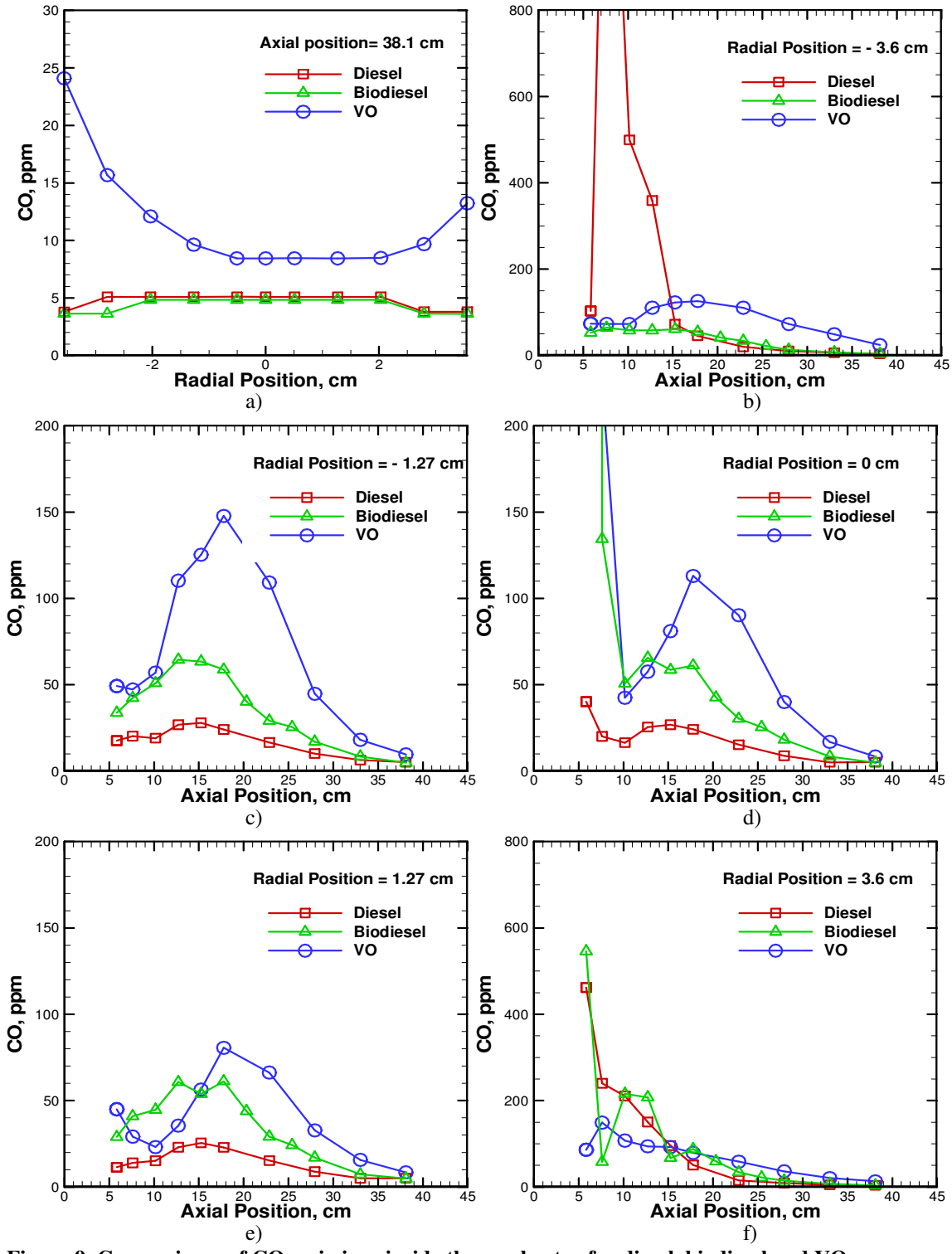

Figure 9. Comparisons of CO emissions inside the combustor for diesel, biodiesel and VO.

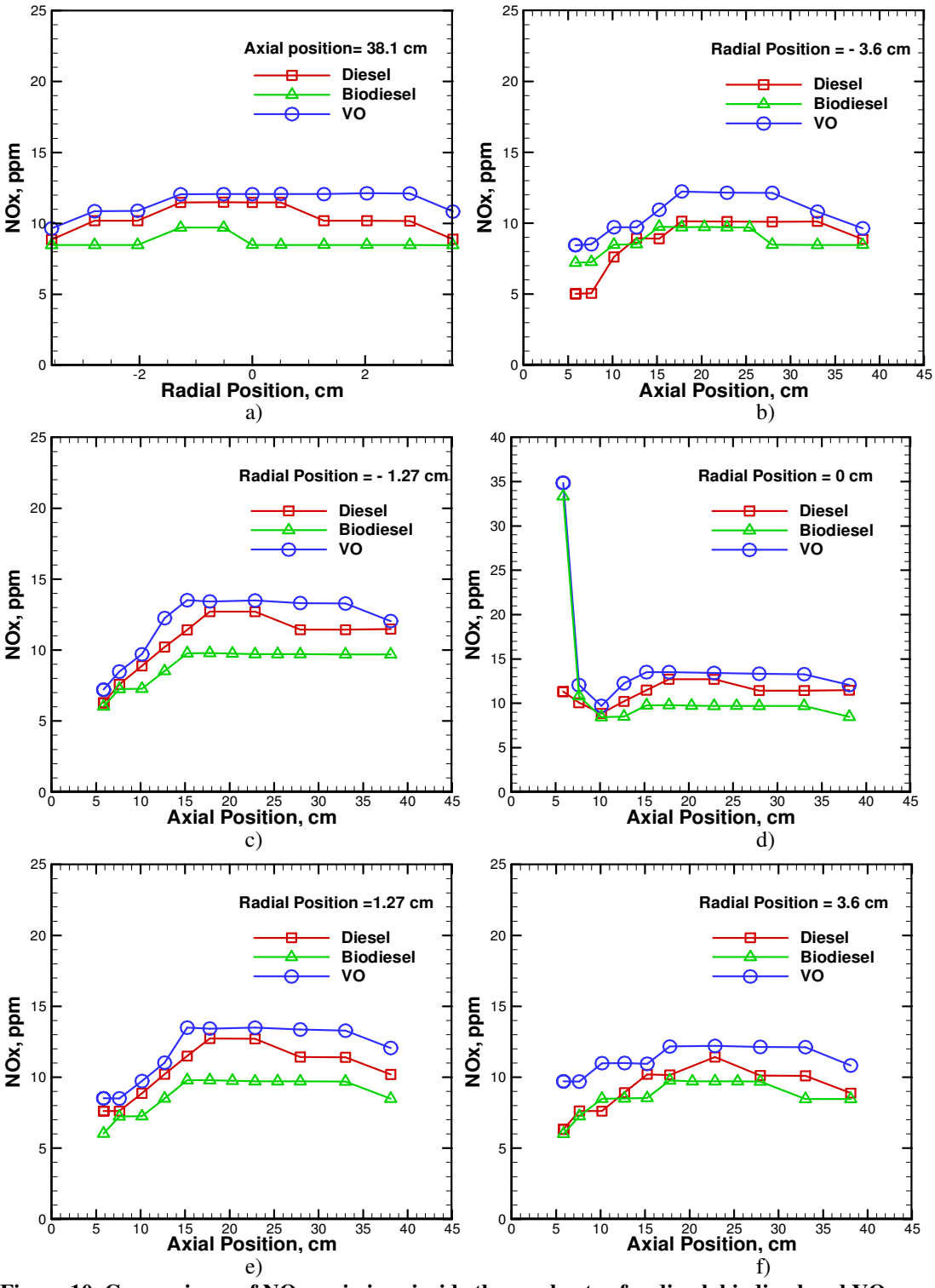

Figure 10. Comparisons of NOx emissions inside the combustor for diesel, biodiesel and VO.

Figure 10(a) shows the radial profiles of NOx emissions at the combustor exit plane and Figures 10(b)-(f) show axial profiles of NOx emissions at radial location near combustor wall, mid radial location on either side of center, and center. The NOx emissions are lowest for the biodiesel flame indicating fuel oxygenation favorably altering chemical kinetics to reduce NOx emissions. However, the lower NOx emissions are not observed for VO flame,

which is also an oxygenated fuel. The VO's adverse fuel physical properties such as higher kinematic viscosity, higher vaporization and auto-ignition temperatures more than offset potential benefit gained by the presence of oxygen in the fuel. Contrary to trend of CO emissions, the NOx emissions near the combustor wall are lower than those near the center. Heat loss resulting in lower gas temperatures curtails thermal NOx formation near the combustor wall. In general, NOx emissions are within 15 ppm or rather low for all three fuels. In general, NOx emissions increase in the downstream direction to reach a constant value depending upon the residence time in the high temperature reaction zone. Upstream locations along center line sufficiently close to injector exit reveal high values resulting from diffusion mode combustion of fuel droplets inside the probe as discussed previously. Therefore, measurements upstream of the flame anchoring location do not represent actual data.

V. Conclusions

In this study, low-emission combustion of diesel, biodiesel and straight VO (soybean oil) has been achieved by utilizing a fuel-flexible FB injector to yield fine droplets for fuels with significantly different physcial properties. Visual images illustrate clean blue flames illustrating nearly lean premixed combustion for all three cases. The CO and NOx emissions at the combustor exit plane are lowest for the biodiesel flame. For NOx emissions, fuel bound oxygen likely favors lower NOx emissions for biodiesel flame compared to diesel flame. In addition, fine droplets produced by the FB injector also play a significant role in producing lower NOx emissions in biodiesel flame. The VO has the highest CO and NOx emissions throughout the combustor, likely due to slightly larger fuel droplets produced. However, for all three fuels, the CO and NOx emissions at the combustor exit plane are very low and close to one another, which demonstrates the ability of the FB atomizer to produce fine fuel spray for fuel's with widely different fuel properties. The flame temperature profiles of all three fuels are consistent with visual flame images and combustor wall temperatures measured by an infrared camera. In summary, FB injector is highly fuel flexible and can produce fine spray to achieve clean combustion with different liquid fuels. In particular, straight VO can be cleanly burnt without the need for chemical processing or preheating.

Acknowledgments

This research was supported by the US Department of Energy Award EE0001733.

References

[1]B. Metzger, "Glycerol Combustion," M.S. Thesis, Mechanical Engineering Dept., North Carolina State University, 2007.

[2]Raghavan, V., Rajesh, S., Parag, S. and Avinash, "Investigation of combustion characteristics of biodiesel and its blends," *Combustion Science and Technology*, Vol. 181, No. 6, 2009, pp. 877-891.

[3]Pan, K.L., Li, J.W., Chen C.P. and Wang, C.H., "On droplet combustion of biodiesel fuel mixed with diesel/alkanes in microgravity condition," *Combustion and Flame*, Vol. 156, No. 10, 2009, pp. 1926-1936.

[4]Park, S.H., Cha, J. and Lee, C.S., "Spray and engine performance characteristics of biodiesel and its blends with diesel and ethanol fuels," *Combustion Science and Technology*, Vol. 183, No. 8, 2011, pp. 802-822.

[5]Wang, X., Huang, Z., Kuti, O.A., Zhang, W. and Nishida, K., "An experimental investigation on spray, ignition and combustion characteristics of biodiesels," *Proceedings of the Combustion Institute*, Vol. 33, No. 2, 2011, pp. 2071-2077.

[6]Panchasara, H., Sequera, D., Schreiber, W. and Agrawal, A.K., "Combustion performance of a novel injector using flow-blurring for efficient fuel atomization," *Journal of Propulsion and Power,* Vol. 25, No. 4, 2009, pp. 984-987.

[7]C.A. Sharp, S.A. Howell and J. Jobe, "The effect of biodiesel fuels on transient emissions from modern diesel engines, part 1 regulated emissions and performance," *SAE Technical Paper No.* 2002–01–1967, 2002.

[8]M.S. Graboski and R.L. McCormick, "Combustion of fat and vegetable oil derived fuels in diesel engines," *Progress in Energy and Combustion Science*, Vol. 24, No. 2, 1998, pp. 125–164.

[9]J.P. Szybist, A.L. Boehman, R.L. McCormick and J.D. Taylor, "Evaluation of formulation strategies to eliminate the biodiesel NOx effect," *Fuel Processing Technology*, Vol. 86, No. 10, 2005, pp. 1109–1126.

[10]James P. Szybist, Juhun Song, Mahabubul Alam and André L. Boehman, **"**Biodiesel combustion, emissions and emission control," *Fuel Processing Technology,* Vol. 88, No. 7, 2007, pp. 679-691.

[11]Cheng, A.S., Upatnieks, A. and Mueller, C.K., "Investigation of the impact of biodiesel fueling on NOx emissions using an optical DI diesel engine," *International Journal of Engine Research*, Vol. 7, No. 4, 2006, pp. 297-318.

[12]A.H. Lefebvre, *Prog. Energy Comubst. Sci.,* Vol. 6, 1980, pp. 233-261.

[13]Benjamin M. Simmons, Pankaj S. Kolhe, Robert P. Taylor, and Ajay K. Agrawal, C. M., "Glycrol Comubstion using Flow-Blurring Atomization," *the 2010 Technical Meeting of the Central States Section of The Combustion Institute*, Champaign, Illinoi, 2010.

[14]Alfonso M. Gañán-Calvo, "Enhanced liquid atomization: From flow-focusing to flow-blurring," *Applied Physics Letters*, Vol. 86, No. 21, AIAA, Sevilla, Spain, 2005, pp. 2141-2142.

[15]Simmons, B.M., Panchasara, H.V. and Agrawal, A.K., "A comparison of air-blast and flow blurring injectors using phase doppler particle analyzer techniques," *ASME Conference Proceedings*, 2009 (48838), pp. 981-992.

[16]Simmons, B.M. and Agrawal, A. K., "Spray characteristics of a flow blurring atomizer," *Atomization and Sprays*, Vol. 20, No. 9, 2010, pp. 821-825.

[17]Panchasara, H., Sequera, D., Schreiber, W. and Agrawal, A.K., "Combustion performance of a novel injector using flow-blurring for efficient fuel atomization," *Journal of Propulsion and Power,* Vol. 25, No. 4, 2009, pp. 984-987.

[18]Benjamin M simmons and Ajay K. Agrawal, "Flow Blurring Atomization for Low-Emission Combustion of Liquid Biofuels," Combustion Science and Technology (to be published)..

[19]Glaude, P.A., Fournet, R., Bounaceur and R.,Moliére, M, "Adiabatic flame temperature from biofuels and fossil fuels and derived effect on NOX emissions," *Fuel Processing Technology*, Vol. 91, No. 2, 2010, pp. 229-235.

[20]Panchasara, H. V., Simmons, B. M., and Agrawal, A. K., "Combustion performance of biodiesel and diesel-vegetable oil blends in a simulated gas turbine burner," *Journal of Engineering for Gas Turbines and Power*, Vol. 131, No. 3, 2009, pp. 1-11.

[21]Schwab, A.W., Dykstra, G.J., Selke, E., Sorenson, S.C., and Pryde, E.H., "Diesel fuel from thermal decomposition of soybean oil," *Journal of the American Oil Chemists' Society,* Vol. 65, No. 11, 1988, pp. 1781-1786.

[22-24]Turns, S.R., *An Introduction to Combustion*, 2nd ed., McGraw-Hill Higher Education, USA, 2000, pp. 256.

[25]Panchasara, H. V., Simmons, B. M., and Agrawal, A. K., "Combustion performance of biodiesel and diesel-vegetable oil blends in a simulated gas turbine burner," *Journal of Engineering for Gas Turbines and Power*, Vol. 131, No. 3, 2009, pp. 1-11.

Paper #070MI-0285 Topic: Microcombustion & New Combustion Devices

8th U. S. National Combustion Meeting
Organized by the Western States Section of the Combustion Institute
and hosted by the University of Utah
May 19-22, 2013

Analysis of a Mesoscale Fuel Reformer with Heat Recirculation and Porous Surface Stabilized Flame

William C. Thompson and Ajay K. Agrawal

Department of Mechanical Engineering, University of Alabama,

Tuscaloosa, Alabama 35401, USA

Abstract

Syngas, or synthetic gas, is composed primarily of hydrogen (H_2) and carbon monoxide (CO). Carbon monoxide and hydrogen store chemical energy, thus syngas can be used as a fuel source. Fuel reformation is the process used to convert an existing fuel source, such as methane or diesel, into synthetic gas. In this study, thermal partial oxidation is used for fuel reformation to eliminate the need for the catalyst. Thermal partial oxidation employs thermal energy to partially oxidize the fuel to produce syngas. The major drawback to this method of fuel reforming is the significant heat loss associated with the procedure. Further, fuel reforming at the mesoscale is difficult because of the short residence time available. In this study, a fuel reformer with a counterflow annular heat exchanger for heat recirculation and porous inert media to stabilize the flame is presented. These design features address the issue of major heat loss and make the process much more efficient. A detailed computational analysis is presented to evaluate design features and show thermal and combustion characteristics of the system. The analysis is based on conservation equations of mass, momentum, and species mass conservation in an axisymmetric domain. The computational analysis includes simulations under rich conditions at ambient pressure. Chemkin and Fluent software were integrated to simulate rich methane-air combustion at different equivalence ratios using a detailed chemical kinetic mechanism. Analysis reveals the effects of reactant inlet temperature and fuel reformer operating conditions on fuel to syngas conversion. Ultimately this study shows that thermal oxidation for fuel reforming can be a viable and efficient process.

I. Introduction

As energy demands increase around the world, more viable fuel sources must be found and utilized. Fuel flexible combustion devices must also be developed to satisfy energy demands in the commercial and industrial sectors. Hydrogen is a clean fuel that contains more energy per unit mass than any hydrocarbon fuel. Hydrogen also generates minimum emissions when burned and no emissions when electro-chemically converted to electricity in a fuel cell [1]. Fuel reforming is used to produce hydrogen, which is the main reactive component in synthetic gas, or syngas. More broadly, syngas is primarily composed of hydrogen (H_2) and carbon monoxide (CO), along with carbon dioxide (CO2), unburned hydrocarbons (UHC), and several other minor species. Syngas is combustible and can be used as a fuel source in internal combustion engines and gas turbines.

Syngas is produced by three major methods: carbon dioxide reforming, water steam reforming, and partial oxidation (POX). Typically, methane is used in these fuel reforming processes but

other hydrocarbon fuels such as diesel, glycerol, bio-diesel, and vegetable oil can also be used to produce syngas [2]. Steam reforming is an endothermic process that occurs at a temperature range of 700°C to 850°C, and because of its low temperature range, coking can be an issue. Partial oxidation reforming is an exothermic reaction that can be achieved through the use of a catalyst or thermally with the use of heat. Catalytic partial oxidation (COPX) reforming occurs in a temperature range of 800°C to 1000°C. CPOX can also be combined with steam reforming in a process called autothermal reforming (ATR).

Thermal partial oxidation (TPOX) reforming occurs above a temperature of 1100°C. Because of the high temperature associated with TPOX, heat loss can be a problem that can decrease the efficiency of the reforming process significantly [3]. This study investigates partial oxidation reforming to produce syngas, specifically TPOX reforming. Numerical simulations using detailed chemical kinetics analysis and computational fluid dynamics analysis integrated with detailed chemical kinetics are presented to show the effect of equivalence ratio, reactant inlet temperature, and pressure on syngas production, specifically the production of hydrogen and carbon monoxide. Methane was the fuel studied for TPOX reforming, but other hydrocarbon fuels could be employed in the future.

Figure 1 shows a schematic of the combustor used for the simulations. It utilizes an annular design to recirculate heat to the incoming reactants and a porous inert media (PIM) to homogenize the mixture, as well as to stabilize the flame and preheat the incoming reactants.

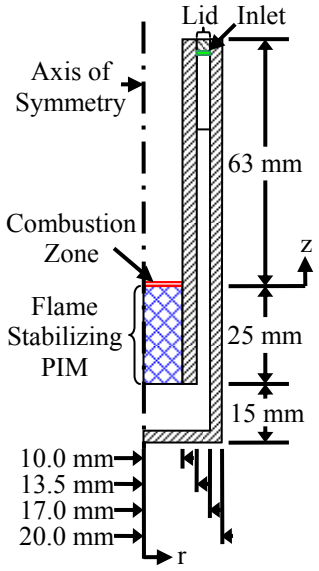

Figure 1. Combustor Schematic

The PIM stabilizes the flame and anchors the flame to the surface at the matrix interface of the PIM, which allows for higher burning speeds. PIM also creates a super adiabatic effect, i.e. higher adiabatic flame temperature locally versus the adiabatic flame temperature of a free flame at the same equivalence ratio. The sensible enthalpy from the products is recirculated through convection from the hot gas to the inert media, which then transfers heat through conduction and radiation to the media upstream of the reaction zone to preheat the incoming reactants. The high

thermal conductivity of the solid matrix compared to the conductivity of the gas enhances heat transfer from the products to the reactants. Thus, the overall effect is a substantial preheating of the incoming reactants. The preheating as well as the heat recirculated through the annulus allow for faster kinetics, higher flame speed, and extended flammability limits of the fuel/oxidizer mixture. The higher temperature compared to the free flame conditions allows initiation and chain-branching mechanisms to occur at ultra-rich equivalence ratios. The extended rich flammability limit allows partial oxidation conditions to be established, thus allowing the stripping of the hydrogen from the original fuel molecule to produce syngas [4]. These advantages allow TPOX to be a viable approach for syngas production. Several simulations are presented to show how these advantages affect syngas production.

II. Methods

Chemkin-Pro and Ansys Fluent were used to simulate methane-air combustion. Chemkin was used to run a perfectly-stirred reactor (PSR) model at various inlet temperatures, equivalence ratios, and operating pressures. Chemkin was also used to run a premixed burner-stabilized flame model. A commercial computational fluid dynamics (CFD) software (Fluent) was integrated with detailed a chemical reaction mechanism to simulate the coupling among fluid dynamics, chemical kinetics, and heat transfer. PSR and burner-stabilized models were used to calculate the optimum operating conditions for the system. The CFD model was used to investigate the overall trend of syngas production. All three model results are presented in sequence, each model with increasing complexity to account for flow and chemical kinetics of the problem.

Perfectly Stirred Reactor (PSR) Model. The simplest model, used to obtain baseline data, is the PSR model. PSR model is a homogenous reactor model in which the contents are assumed to be nearly spatially uniform due to high diffusion rates, and the reactor is assumed to be perfectly mixed to describe the spatially averaged properties, or bulk properties. Because of the homogeneous nature of the mixture, the conversion of reactants to products is controlled by reaction rates and not by the mixing processes. This model consists of a chamber, which may allow for heat loss, with inlets and outlets. The general conservation equations in this model as implemented in the Chemkin software include the conservation equations of mass, energy, and species. Figure 2 depicts a schematic representation of a generic perfectly stirred reactor. [5]

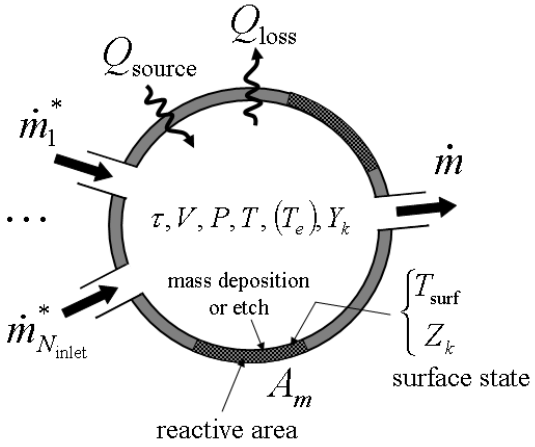

Figure 2. Schematic Representation of a Perfectly Stirred Reactor

This study uses a single PSR reactor with one inlet and an outlet at steady state. This model can evaluate steady state systems and transient systems, but steady state was chosen to obtain product gas properties for a fixed residence time. The inlet and outlet serve as a means for mass to enter and leave the system. A major parameter for this simulation that must be specified is a nominal residence time (τ), which is calculated using the nominal density of the mixture, mass flow rate, and reactor volume. A sufficiently large residence time of 0.5 s was used in this study to achieve near equilibrium conditions at the reactor exit. The reactor volume and mass flow rate are arbitrary values while the density remains constant. Other parameters that must be specified are inlet temperature, pressure, equivalence ratio, heat loss, surface temperature, the species of fuel and oxidizer. In this study heat loss was assumed zero, the surface temperature was considered to be equal to the gas temperature, and methane-air combustion was used for reactant and product species. A parametric study was conducted by varying equivalence ratio, operating pressure, and reactant inlet temperature. The equivalence ratio was varied from 1 to 3 in increments of 0.5. The pressure was varied from 1 atm to 5 atm in increments of 1 atm. The inlet temperature was varied from 300 K to 600 K in increments of 50 K. This simulation was used to calculate the optimum operating conditions when most syngas is effectively produced.

Premixed Burner Stabilized Flame Model. The premixed burner-stabilized flame model is a 1-D premixed laminar flame model. This model is often used to study the chemical kinetics of a problem in a combustion environment. This simulation has the ability to model the chemical kinetics and transport processes that occur inside the flame to understand the combustion process itself. Like the PSR model, the general conservation equations of mass, energy, and species are used. In addition, the conservation of momentum in 1D is also used [5]. This model can be run by solving the energy equation or by specifying the gas temperature profile to account for the heat loss. Regardless, the model has to have a temperature profile, generated or specified, to complete the simulation. In this study, the energy equation was solved by neglecting the heat loss [6]. A sufficiently large unbunt gas temperature of 600 K was specified because optimum results occur when the reactants enter the combustor at a high temperature (higher than ambient). An equivalence ratio of 2.5 was used to maximize syngas production. This analysis was conducted only at 1 atm since pressure effects observed from PSR models would also be viable for this model. Methane-air combustion simulation was performed to determine how the product species of hydrogen and carbon monoxide develop axially. Further, the temperature profile will be generated for the analyzed length (10 cm), and along with profiles of the product species, the reaction zone can be determined.

Computational Fluid Dynamics-Chemical Kinetics Model: This detailed model, though preliminary at this stage, combined CFD analysis with chemical kinetics analysis. The computational domain was assumed to be axisymmetric to approximate the actual hardware. For steady, laminar flow, the governing equations of mass, momentum, and energy are presented in Equations 2 through 5.

Mass conservation equation:

$$\frac{\partial}{\partial z}(\rho v_z)+\frac{\partial}{\partial r}(\rho v_r)+\frac{\rho v_r}{r}=S_m \tag{2}$$

Momentum conservation equation in the axial (z) direction:

$$\frac{1}{r}\frac{\partial}{\partial z}\left(r\rho v_z v_z\right)+\frac{1}{r}\frac{\partial}{\partial r}\left(r\rho v_r v_z\right)=-\frac{\partial P}{\partial z}+\frac{1}{r}\frac{\partial}{\partial z}\left[r\mu\left(2\frac{\partial v_z}{\partial z}-\frac{2}{3}\vec{\nabla}\cdot\vec{v}\right)\right]+\frac{1}{r}\frac{\partial}{\partial r}\left[r\mu\left(\frac{\partial v_z}{\partial r}+\frac{\partial v_r}{\partial z}\right)\right]+S_z \tag{3}$$

Momentum conservation equation in the radial (r) direction:

$$\frac{1}{r}\frac{\partial}{\partial z}\left(r\rho v_z v_r\right)+\frac{1}{r}\frac{\partial}{\partial r}\left(r\rho v_r v_r\right)=-\frac{\partial P}{\partial r}+\frac{1}{r}\frac{\partial}{\partial z}\left[r\mu\left(2\frac{\partial v_r}{\partial z}+\frac{\partial v_z}{\partial r}\right)\right]+\frac{1}{r}\frac{\partial}{\partial r}\left[r\mu\left(2\frac{\partial v_r}{\partial r}-\frac{2}{3}\vec{\nabla}\cdot\vec{v}\right)\right]-2\mu\frac{v_r}{r^2}+\frac{2}{3}\frac{\mu}{r}\left(\vec{\nabla}\cdot\vec{v}\right)+\rho\frac{v_z^2}{r}+S_r \tag{4}$$

Energy conservation equation:

$$\frac{1}{r}\frac{\partial}{\partial r}\left(r\rho v_r c_p T+r\rho v_r\frac{v^2}{2}\right)+\frac{\partial}{\partial z}\left(\rho v_z c_p T+r\rho v_z\frac{v^2}{2}\right)=\frac{1}{r}\frac{\partial}{\partial r}\left(k_r r\frac{\partial T}{\partial r}\right)+\frac{\partial}{\partial z}\left(k_z\frac{\partial T}{\partial z}\right)+S_E \tag{5}$$

Here v is the total velocity and v_r and v_z are the radial and axial components of velocity, respectively [7]. The governing equations are solved in Fluent software. The chemical reactions were represented by a 60-step reaction mechanism for methane-air combustion typically used to calculate laminar flame speed in Chemkin software. The elements associated with this kinetics input file are hydrogen (H), oxygen (O), carbon (C), and nitrogen (N). The associated 19 species are CH_4, CH_3, CH_2, CH, CH_2O, HCO, CO_2, CO, H_2, H,O_2, O, OH,HO_2,H_2O_2, H_2O, and N_2. Table 1 shows the reactions involved in the 60-step reaction mechanism.

The computational domain was divided into various zones including the inlet, porous media zone, and combustion zone. Boundary conditions were specified for each of these zones, such as mass flow rate into the combustor, the porosity of the porous media, and total reactant inlet enthalpy. These are just a few examples of the many boundary conditions specified for this problem. Reactions were turned off everywhere except in the porous media zone and combustion zone for this simulation, which was comprised of domain including PIM and the combustor downstream of it. Source terms to specify the mass flow rate into the system. Three volumetric mass source terms were used in this simulation, the total mass source term, the methane mass source term, and the oxygen mass source term. The mass source terms were based on a $\dot{m}_{total}$ = 7.911e-4 kg/s, a $\dot{m}_{CH_4}$ = 1.041e-4 kg/s, and a $\dot{m}_{O_2}$ = 1.602e-4 kg/s. It is possible to use a radiation model with this simulation, but it was not used for simplicity. The energy model and species transport models were the main models utilized for this simulation. The mixture properties are specified or calculated in the species transport model. These properties must be correct to ensure correct simulation.

Table 1. Reactions for 60-Step Methane Reaction Mechanism

CH3+H+M=CH4+M
CH4+O2=CH3+HO2
CH4+H=CH3+H2
CH4+O=CH3+OH
CH4+OH=CH3+H2O
CH3+O=CH2O+H
CH3+OH=CH2O+H2
CH3+OH=CH2+H2O
CH3+H=CH2+H2
CH2+H=CH+H2
CH2+OH=CH2O+H
CH2+OH=CH+H2O
CH+O2=HCO+O
CH+O=CO+H
CH+OH=HCO+H
CH+CO2=HCO+CO
CH2+CO2=CH2O+CO
CH2+O=CO+H+H
CH2+O=CO+H2
CH2+O2=CO2+H+H
CH2+O2=CH2O+O
CH2+O2=CO2+H2
CH2+O2=CO+H2O
CH2+O2=CO+OH+H
CH2+O2=HCO+OH
CH2O+OH=HCO+H2O
CH2O+H=HCO+H2
CH2O+M=HCO+H+M
CH2O+O=HCO+OH
HCO+OH=CO+H2O
HCO+M=H+CO+M
HCO+H=CO+H2
HCO+O=CO2+H
HCO+O2=HO2+CO
CO+O+M=CO2+M
CO+OH=CO2+H
CO+O2=CO2+O
HO2+CO=CO2+OH
H2+O2=2OH
OH+H2=H2O+H
H+O2=OH+O
O+H2=OH+H
H+O2+M=HO2+M
OH+HO2=H2O+O2
H+HO2=2OH
O+HO2=O2+OH
2OH=O+H2O
H+H+M=H2+M
H+H+H2=H2+H2
H+H+H2O=H2+H2O
H+H+CO2=H2+CO2
H+OH+M=H2O+M
H+O+M=OH+M
H+HO2=H2+O2
HO2+HO2=H2O2+O2
H2O2+M=OH+OH+M
H2O2+H=HO2+H2
H2O2+OH=H2O+HO2

The solution methods used for this problem consisted of the SIMPLEC pressure-velocity coupling scheme, and QUICK and power-law differencing schemes. Different schemes were used for energy, momentum, species, etc. The power law scheme was exclusively used for species equations, while the energy and momentum utilized the QUICK scheme. All species and the energy equations were under-relaxed by a factor of 0.5, and the momentum equation was under-relaxed by a factor of 0.7. Convergence criterion (mostly 0.001) were specified and the solution was initialized with initial guesses for the species and temperature. Temperature was guessed to be 500 K everywhere, and the mole fractions of H_2 and O_2 were specified to be 0.0548 and 0.21933, respectively.

Methane-air combustion was analyzed with this simulation at an equivalence ratio of 1.0 and 1.25. Because of the simplifications made for this problem, such as turning off the radiation model and not refining the grid at high velocities inside the combustor, the simulation at an equivalence ratio of 1.5 reached blow-off. Blow-off would not have occurred if fewer assumptions were made. From experimental work, it is known that stable methane-air combustion easily occurs at an equivalence ratio of 1.5. Thus, these assumptions that simplify problem also introduce errors because some of the realism is removed. However, the model used shows the trend of how hydrogen and carbon monoxide are produced as the reactants become rich with increasing equivalence ratio. The assumptions made were necessary to reduce the complexity brought to the simulation with detailed chemical kinetics, and although these assumptions introduced error, they still produce viable initial results that can be used to interpret the behavior of the system.

III. Results and Discussion

PSR Model. PSR model provided data showing the optimum operating conditions for this system. Figure 3 depicts the adiabatic flame temperature versus pressure for different reactant inlet temperatures. Reactant inlet temperature was varied from 300 K to 600, the pressure was varied from 1 atm to 5 atm, and the equivalence ratio was varied from 1 to 3. From Figure 3, it can be seen that the adiabatic flame temperature decreases as equivalence ratio increases, and adiabatic flame temperature increases as pressure increases. Some of the temperature profiles appear constant, because of the scale of the plot. As inlet temperature increases, the adiabatic flame temperature also increases, as expected. These results just verified what was expected of the system. Figure 4 shows how the adiabatic flame temperature decreases with increasing equivalence ratio for reactant inlet temperature of 300 K. The mole fraction of hydrogen and carbon monoxide are of the greatest interest because they are the primary reactants in syngas. Figure 5 shows how hydrogen and carbon monoxide production are affected by equivalence ratio and reactant inlet temperature for operating pressure of 5 atm.

Syngas production increases with increasing reactant inlet temperature. As seen in Figure 5, hydrogen production starts to decrease after an equivalence ratio of 2.5, and carbon monoxide production starts to decrease after an equivalence ratio of 2.0. Syngas production efficiency is sometimes defined as seen in equation 6:

$$\eta_{sygas\ production} = \frac{H_{2,production}}{CO_{production}} \quad (6)$$

According to this definition, the most efficient operating conditions are at an equivalence ratio of 2.3. Thus, from this simulation it is shown that the optimum operating conditions for optimum syngas production are at a high inlet temperature and an equivalence ratio of 2.3. Since the optimum syngas production occurs at an equivalence ratio of 2.3, the effect of pressure was investigated for equivalence ratios between 2 and 3 and varying the pressure from 1 atm to 5 atm. Figure 6 shows how production of hydrogen and carbon monoxide are affected by pressure at an inlet temperature of 600 K.

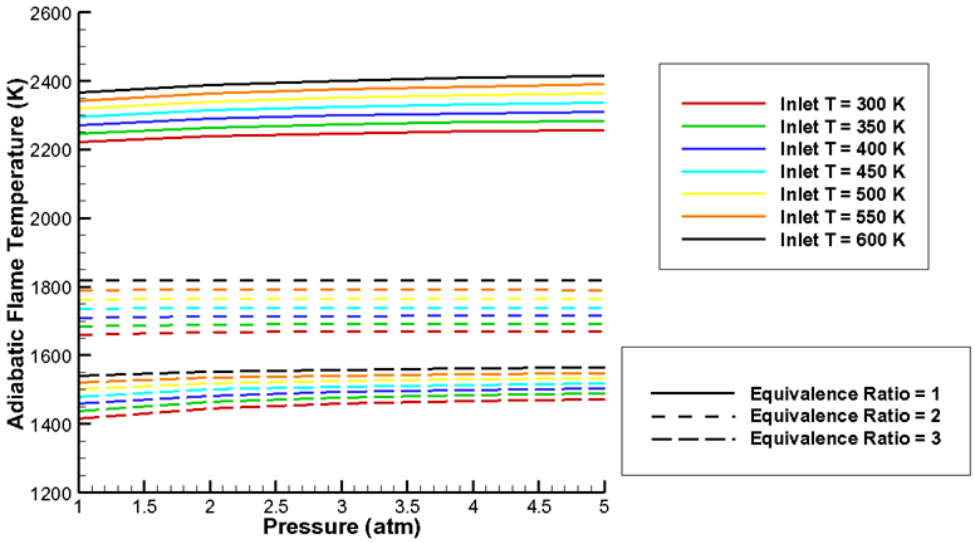

Figure 3. Adiabatic Flame Temperature as a Function of Pressure and Inlet Temperature

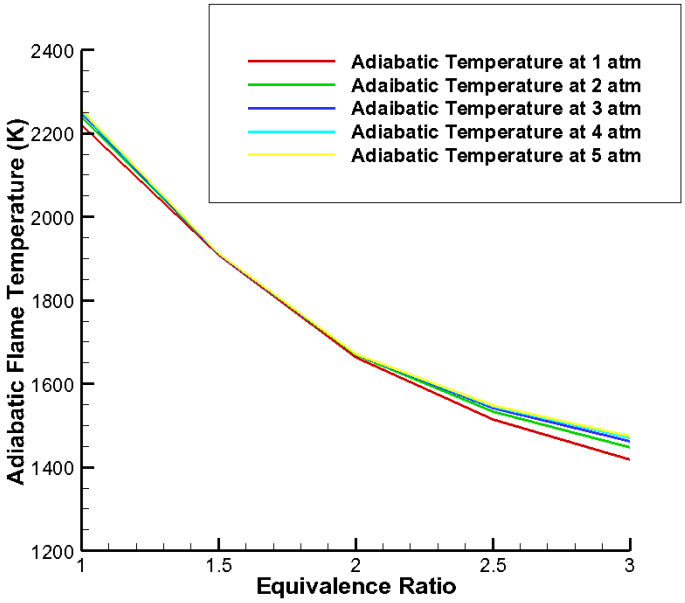

Figure 4. Equivalence Ratio versus Adiabatic Flame Temperature at Inlet Temperature of 300 K

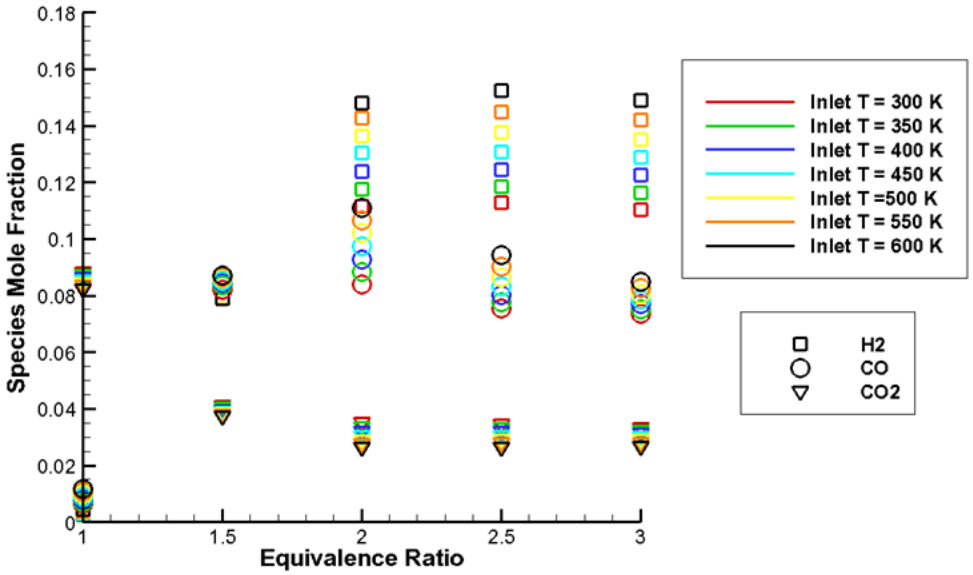

Figure 5. Species Mole Fraction as a Function of Equivalence Ratio and Inlet Temperature

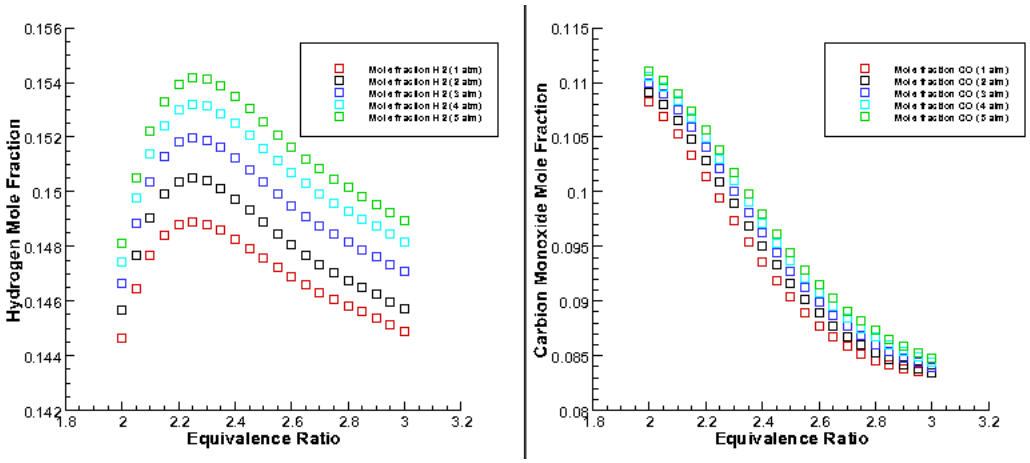

Figure 6. Hydrogen and Carbon Monoxide Production between Equivalence Ratios of 2 and 3 Ranging From a Pressure of 1 atm to a Pressure of 5 atm

Figure 6 further states that the optimum operating conditions occur at an equivalence ratio of 2.3. This is where the maximum hydrogen production to carbon monoxide production ratio occurs. This figure also shows that hydrogen production and carbon monoxide production both increase with increasing pressure. Thus, the optimum conditions for syngas production occur at a high inlet temperature, an equivalence ratio of 2.3, and high pressure.

Premixed Burner Stabilized Model. The premixed burner-stabilized model was used to determine how hydrogen and carbon monoxide are produced axially as the reactions progress through the combustor. The temperature profile was also generated for the length examined (10 cm). Figure 7 shows hydrogen and carbon monoxide profiles along the 10 cm length of the burner-stabilized adiabatic flame. Figure 7 shows that the reactants enter the combustion zone, react in the first 0.5 cm of the combustor, and increase the temperature to 1655 K. Carbon monoxide mole fraction remains fairly constant after the reaction zone, and while hydrogen mole fraction increases along the length examined. This result shows that the reactions that produce the hydrogen extend past the reaction zone, while reactions producing carbon monoxide occur mainly within the reaction zone. This simulation was only carried out at 1 atm only because as the pressure increases, a similar trend of pressure on species mole fractions as the PSR model is expected for the burner-stabilized model.

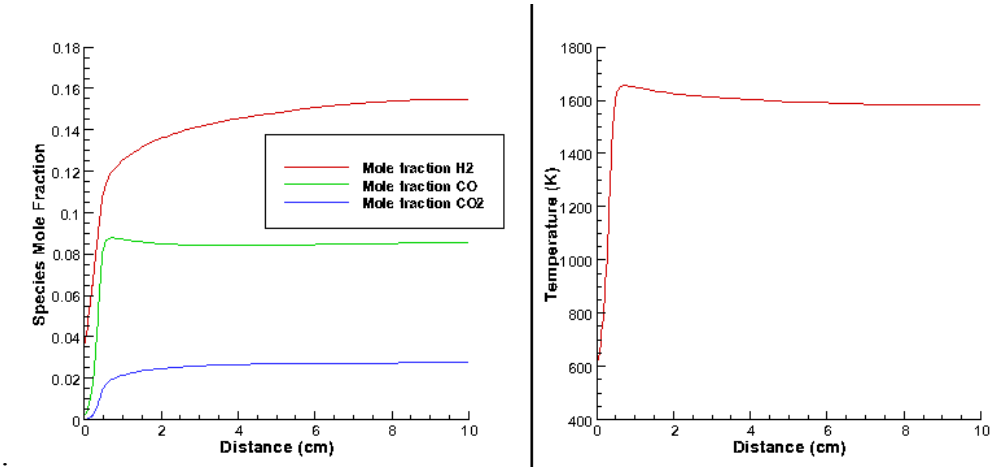

Figure 7. Burner-Stabilized Model Results

Computational Fluid Dynamics-Chemical Kinetics Model: Figure 8 compares the temperature contours from detailed CFD simulations at equivalence ratio of 1.0 and 1.25. As Figure 8 depicts, the porous media plays a vital role in preheating the reactants. Heat from the reaction is conducted into the porous media, which is in contact with the combustor wall, and in turn is conducted through the wall into the incoming reactants. In the reaction zone, boundary layers are formed, which tend to insulate the reactants in the annulus from the high temperature reaction zone of the combustor. Thus, most of the preheating of the reactants takes place around the porous media. Less heat is conducted in the case were the equivalence ratio equals 1.25 because the adiabatic flame temperature is less than in the case where the equivalence ratio equals 1.0. The reactant inlet temperature for both cases is around 400 K and the combustor pressure was specified as atmospheric. More efficient syngas production will occur at the optimum conditions specified earlier, but this simulation was carried out at a lower inlet temperature, pressure, and equivalence ratio to gain basic understanding of the coupling effects between fluid flow, heat transfer, porous media, and chemical kinetics. The heat transfer pathways would also be influenced by radiation which could be significant in some regions of the system, but ignored in this preliminary study.

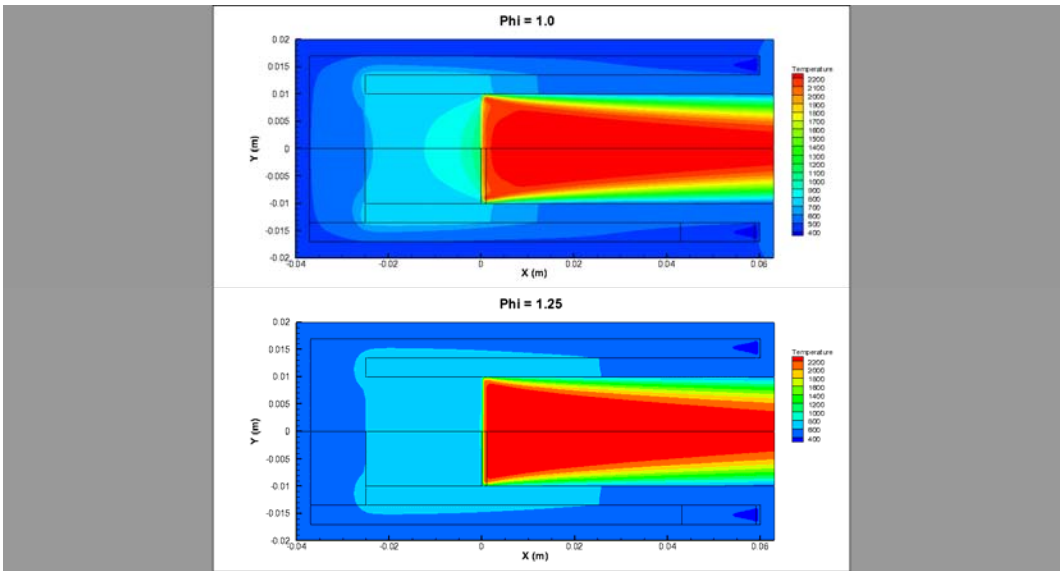

Figure 8. Temperature Contours for CFD-Detailed Kinetics Simulation

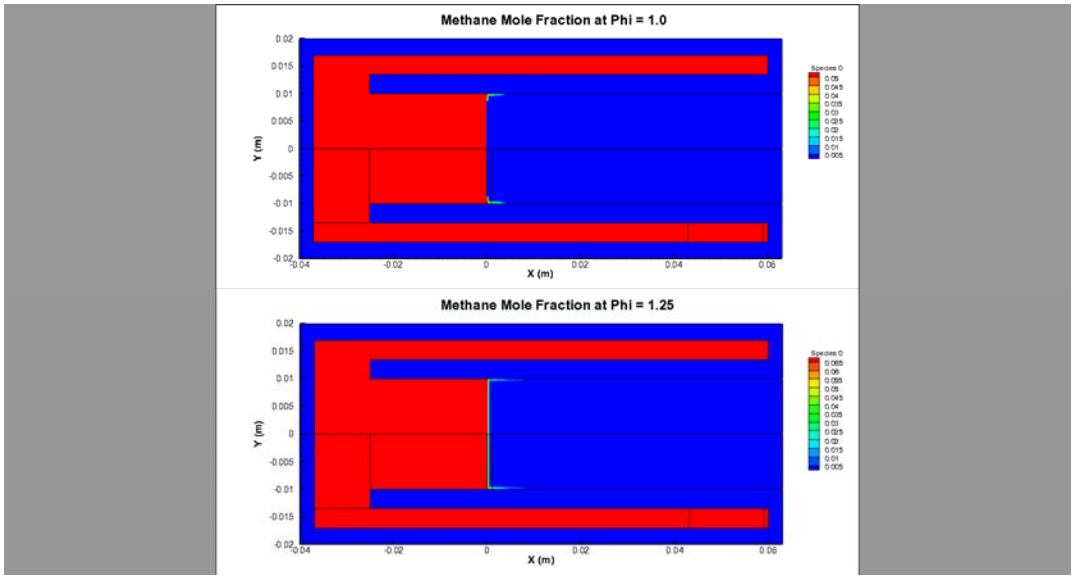

Figure 9. Methane Mole Fraction Contours for CFD-Detailed Kinetics Simulation

Figure 9 depicts the methane (CH_4) mole fraction. The simulation specified where reactions could take place, which is only in the porous media, flame and exhaust zones. Figure 9 shows no methane present in these zones, signifying complete oxidation of the original fuel. The same can be said for Figure 10, which shows the oxygen (O_2) mole fraction. Both cases for Figures 9 and 10 are the same because the total mass flow rate was held constant. Next, the radical production was examined to understand how it affected the reaction zone. Oxygen radical (O) and hydrogen radical (H) are generated at the plane just downstream of the porous media, and are confined to a narrow but intense flame zone. These radicals help sustain reactions that would eventually produce product species including H_2 and CO in case of fuel-rich combustion. Figure 11 shows contours of the mole fractions of oxygen radicals (O) produced in this system. Similarly, Figure 12 and 13 show contours of the mole fraction of hydrogen radicals (H) and hydroxyl radical (OH) produced in the system.

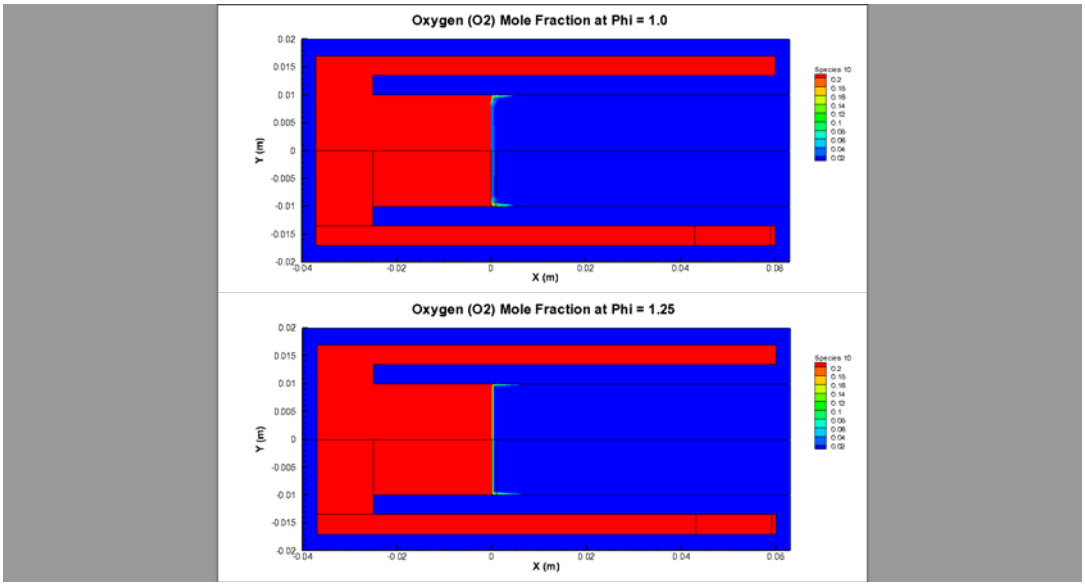

Figure 10. Oxygen (O_2) Mole Fraction Contours for CFD-Detailed Kinetics Simulation

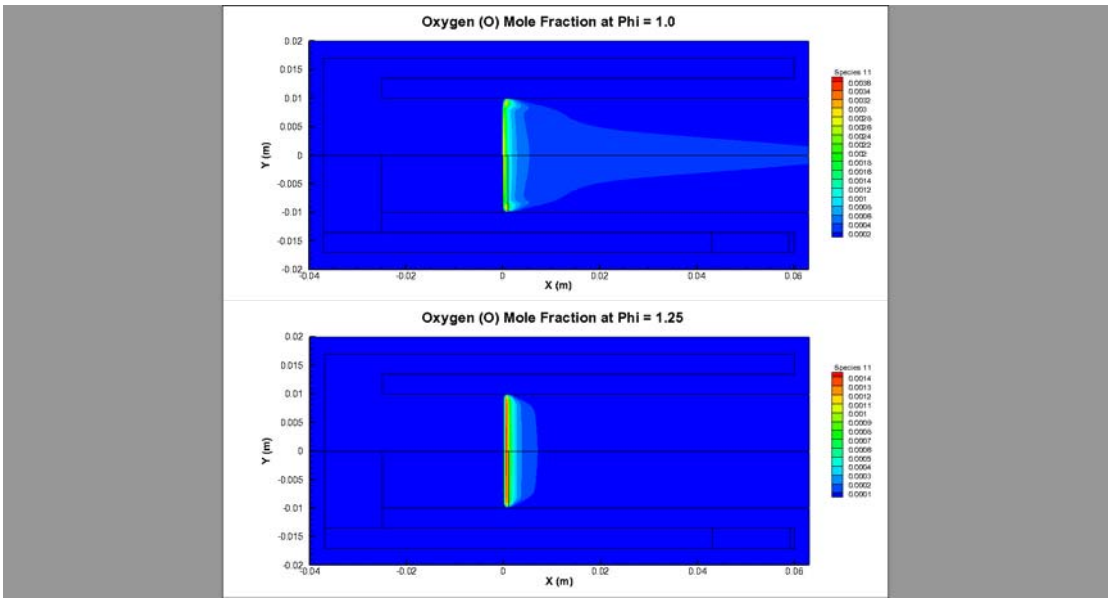

Figure 11. Oxygen Radical (O) Mole Fraction Contours for CFD-Detailed Kinetics Simulation

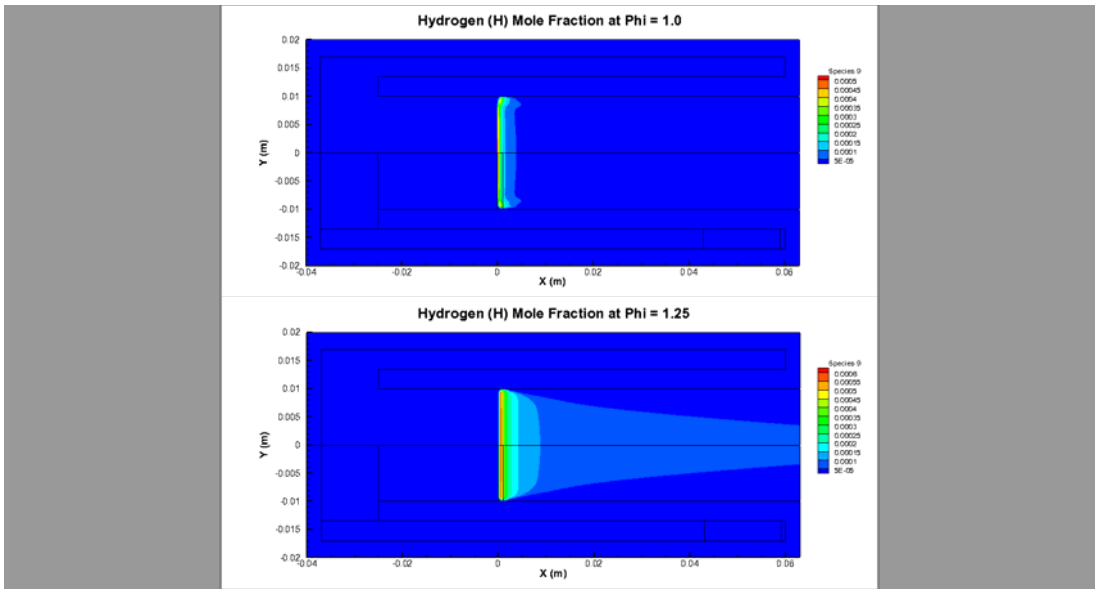

Figure 12. Hydrogen Radical (H) Mole Fractions for Fluent Simulation

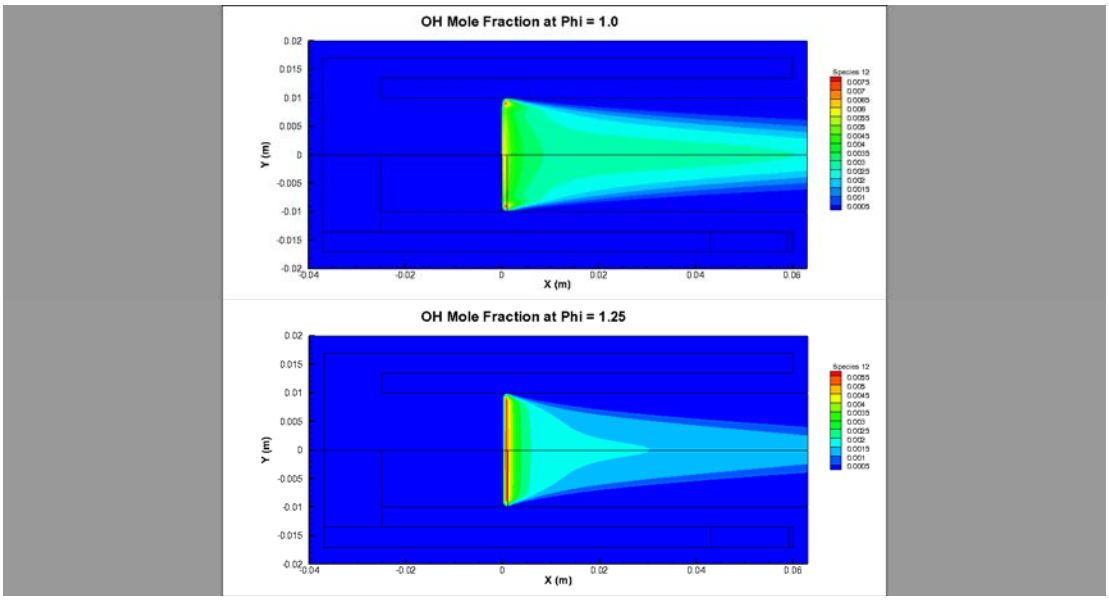

Figure 13. OH Mole Fractions for Fluent Simulation

Figures 11, 12, and 13 show that at stoichiometric conditions (ϕ=1.0) more radicals are produced compared to the fuel-rich combustion at ϕ=1.25. Radical concentration related to the reaction zone temperature, which is higher for ϕ=1.0. These results also identify the axial and radial extend of radical production zones, although complete reliance on these results will require a fully grid-independent solution which has not been attained in the present study because of the large computational requirements. Still, these results offer unparallel insight into the reaction zone and its coupling with various fluid flow and heat transfer phenomena evident in the present system.

Next, CFD results are examined to evaluate production of H_2 and CO. Figure 13 depicts the contours of hydrogen (H_2) mole fractions for this system. As the equivalence ratio increases past stoichiometric condition and the mixture becomes fuel-rich, H_2 production can be expected to increase as inferred from PSR and burner-stabilized models. Present simulations replicate this trend, and also show increased H_2 in the boundary layer region where the temperature is lower for the $\phi = 1.25$ case. Figure 14 shows the contour plots of CO mole fraction for this system. A similar trend as observed for the H_2 mole fractions is also observed for the CO mole fraction. More CO is produced for fuel-rich conditions as expected. Under rich conditions excess fuel is present, and since methane's molecular make up is of carbon and hydrogen, more hydrogen and carbon become available in the form of unreacted products.

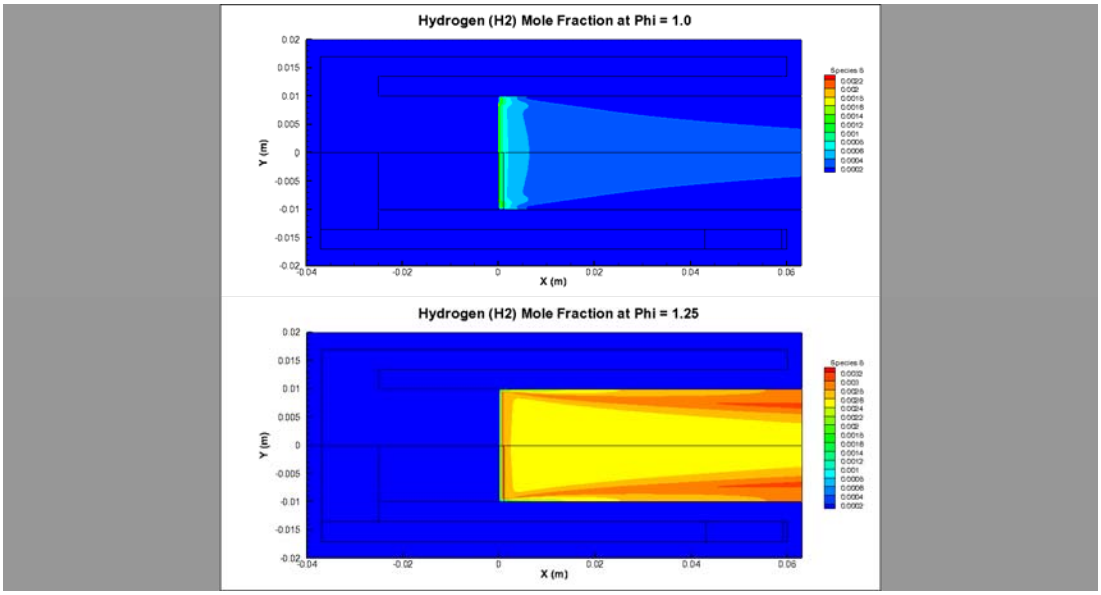

Figure 14. H_2 Mole Fractions for Fluent Simulation

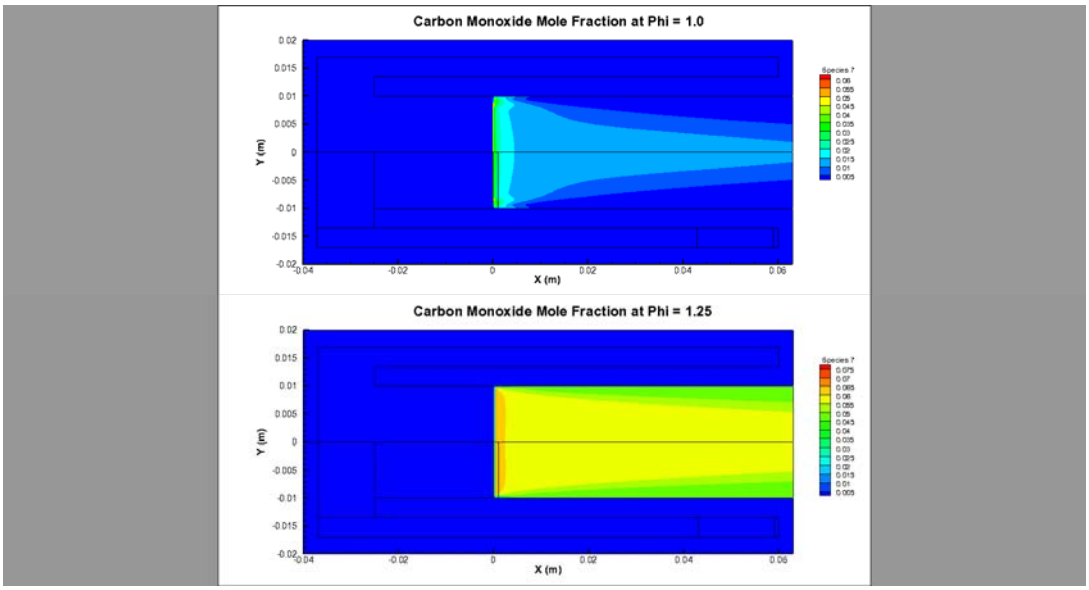

Figure 15. CO Mole Fractions for Fluent Simulation

Finally, Figure 16 shows the contour plot of CO_2 mole fraction in the system. Results show that more CO_2 is produced outside of the flame in the boundary layer, and more CO is produced within the flame zone. This effect can be explained by increased dissociation in the high-temperature reaction zone.

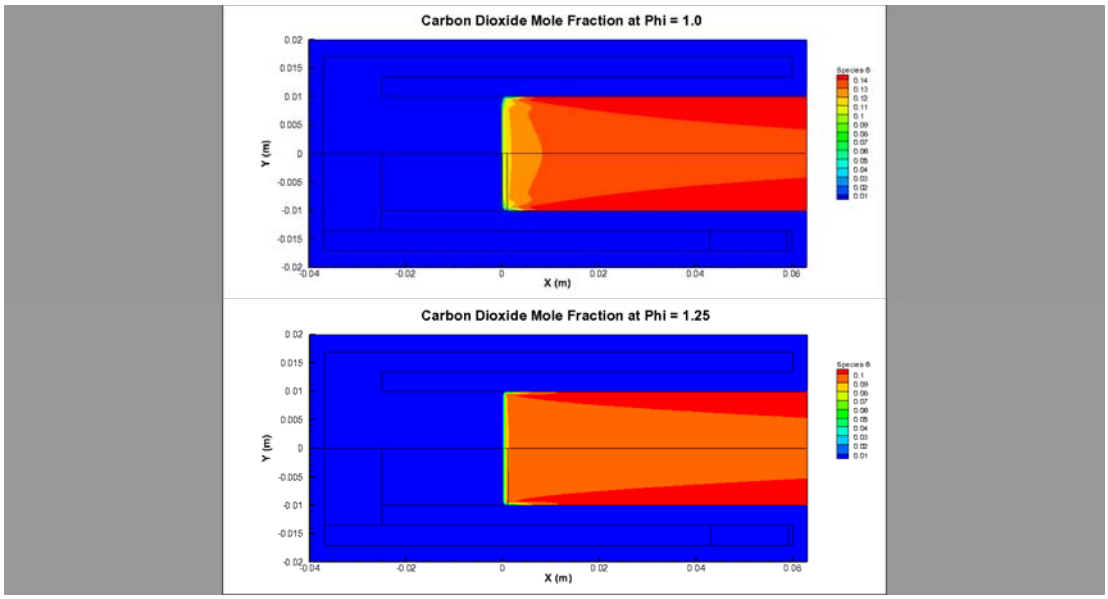

Figure 15. CO_2 Mole Fractions for Fluent Simulation

IV. Conclusions

Three models with increasing complexity were used to investigate fuel-rich combustion of methane to produce syngas containing hydrogen (H_2) and carbon monoxide (CO). Simple PSR model provided results that allowed the optimum operating conditions for syngas production to be determined. These optimum conditions were at high operating pressure, high inlet temperature, and an equivalence ratio of around 2.3. The burner-stabilized model showed how the product species, specifically H_2 and CO, were produced in the reaction zone, as well as the pre-reaction zone and post-reaction zone. Most H_2 was produced in the reaction zone, but these reactions continued downstream to further increase H_2 production. The CO was produced mainly in the reaction zone, and downstream of this zone, CO was consumed by further oxidation reactions. CFD analysis with detailed chemical kinetics revealed the complex coupling among fluid flow, heat transfer, porous media, and chemical reactions. From this simulation it was found that most of the preheating of the reactants occurs in the porous media region. Because of the simplification introduced (e.g., no radiation), the heat transfer model is not completely accurate, but the trend observed with the porous media is consistent with previous experimental observations. Simulations revealed that fewer radicals are produced in the reaction zone as the mixture becomes fuel-rich. Simulations also identified how H_2 and CO production is affected by the local temperature. H_2 production increases in the boundary layer for the fuel-rich reactant mixture. CO_2 production also increased in the boundary layer because of low temperature and less dissociation. These trends offer unparallel insight into combustion processes inside this system. However, future studies will focus on fully validated, grid independent solution incorporating detailed chemical kinetics with thermal radiation for a range of operating conditions to optimize the system performance.

V. Acknowledgments
This research was supported by US Department of Energy Award EE0003134.

References
[1] Toledo, M., Bubnovich, V., Saveliev, A., Kennedy, L., *International Journal of Hydrogen Energy, 34(2009), 1818-1827*
[2] Dobrego, K.V., Gnesdilov, N.N., Lee, S.H., Choi, H.K., *Chemical Engineering Journal, 144(2008), 79-87*
[3] Ayabe S., Omotoa H., Utaka T., Kikuchi R., Sasaki K., Teraoka Y., & Eguchi K., *Applied Catalysis A: General, 241(2003), 261-269*
[4] Pastore, A., Mastorakos, E., *Fuel 90* (2010) 64-76.
[5] Chemkin Theory Manual
[6]Chemkin Tutorial Manual
[7] Marbach, T.L.,"*Mesoscale, Porous Media Heat Recirculating Combustor,"* Ph.D. Dissertation, Department of Mechanical Engineering, University of Oklahoma, 2005.

Spring Technical Meeting
of the Central States Section of the Combustion Institute
April 22–24, 2012

Reforming Reactor System for Partial Oxidation and Autothermal Fuel Reforming

William C. Thompson, Dan Hershman and Ajay K. Agrawal

Department of Mechanical Engineering, University of Alabama,

Tuscaloosa, Alabama 35401, USA

A combustion system to reform long-chain hydrocarbons such as diesel or Jet-A fuel into syngas is presented. Heat recirculation concept based reactor is used to partially combust highly rich air-fuel mixture to yield product gas with very high CO and H_2 concentrations. Chemical equilibrium and perfectly stirred reactor models were used to simulate the rich combustion of n-heptane to obtain insight into CO and H_2 conversion efficiency at elevated temperatures (in excess of 1000°C) to sustain thermal partial oxidation. Experimental system developed uses preheated air, convective and conductive annular heat transfer, twin-fluid injectors, and porous inert media combustion to test the viability of partial oxidation reaction and autothermal fuel reforming without the use of a catalyst. The complete reforming reactor is 9.3 inches long and 4.6 inches in diameter. Preliminary experimentation on rich methane are carried out to demonstrate combustion at equivalence ratio of three indicating potential of the developed fuel reformer.

1. Introduction

Fossil fuel reforming describes the process of reforming commonly available fossil fuels into hydrogen (or other useful products). The hydrogen produced by fuel reforming can be used in fuel cells and internal combustion engines, for cooling of gas turbines and generators, and in heavy petro-chemical processes. Natural gas, methane, and diesel are the most commonly reformed fuels, although diesel's sulfur content and much higher enthalpy of formation leads to some difficulties in reforming diesel using standard processes. Catalytic steam methane reforming (CSMR) combined with water-gas shift (WGS) cleanup, the current industry standard technique for hydrogen production, is shown as follows:

$$CH_4 + H_2O \rightarrow CO + 3H_2 \qquad \Delta H^0_{298K} = +206.16\ ^{kJ}/_{mol} \tag{1}$$

$$CO + H_2O \leftrightarrow CO_2 + H_2 \qquad \Delta H^0_{298K} = -41.15\ ^{kJ}/_{mol} \tag{2}$$

$$CH_4 + 2H_2O \leftrightarrow CO_2 + 4H_2 \qquad \Delta H^0_{298K} = +165.01\ ^{kJ}/_{mol} \tag{3}$$

Catalytic steam methane reforming is an endothermic process that occurs at 700°C to 850°C and 2-25 atmospheres of gage pressure. Water-gas shift is an exothermic process that can be used as an after-treatment to raise the efficiency of any reforming process, as well as improving the hydrogen output to 70-80% of the products. When CSMR and WGS are combined, the resulting combined endothermic process requires a steam-to-carbon mass ratio greater than 3:1 to avoid coking and steam recycling to maintain process efficiency and offset the high steam-to-carbon mass ratio.

Another reforming technique that has gained traction recently, especially when combined with water-gas shift, is catalytic partial oxidation (CPOX), shown as follows:

$$CH_4 + \frac{1}{2}O_2 \rightarrow CO + 2H_2 \qquad \Delta H^0_{298K} = -35.66\ ^{kJ}/_{mol} \tag{4}$$

$$CO + H_2O \leftrightarrow CO_2 + H_2 \qquad \Delta H^0_{298K} = -41.15\ ^{kJ}/_{mol} \tag{5}$$

$$CH_4 + H_2O + \frac{1}{2}O_2 \leftrightarrow CO_2 + 3H_2 \qquad \Delta H^0_{298K} = -76.81\ ^{kJ}/_{mol} \tag{6}$$

Catalytic partial oxidation reforming is a mildly exothermic reaction that occurs at 800°C to 1000°C and 1-25 atmospheres of gage pressure and results in a 2:1 molar ratio of hydrogen to carbon monoxide. However, the pure oxygen atmosphere and low-sulfur content (<50ppm) fuel required for the reaction makes CPOX an expensive alternative to CSMR. Partial oxidation reactions can also occur without the presence of catalysts in thermal partial oxidation reforming (TPOX), which requires temperatures above 1100°C to occur, lowering the efficiency of the overall process, and, in most cases, offsetting the cost savings from not using catalysts. Thermal partial oxidation reforming is ideal for high sulfur, long hydrocarbon-chained fuels (such as diesel) due to the lack of a poisonable catalyst and the high reaction temperature required to reform large hydrocarbons instead of burning them in coking combustion.

Combining the reactions in steam methane reforming and partial oxidation reforming is autothermal reforming (ATR), shown as follows:

$$CH_4 + H_2O \leftrightarrow CO + 3H_2 \qquad \Delta H^0_{298K} = +206.16\ ^{kJ}/_{mol} \tag{7}$$

$$CH_4 + \frac{1}{2}O_2 \leftrightarrow CO + 2H_2 \qquad \Delta H^0_{298K} = -35.66\ ^{kJ}/_{mol} \tag{8}$$

$$CH_4 + (1-x)H_2O + \frac{x}{2}O_2 \leftrightarrow CO + (3-x)H_2 \quad \Delta H^0_{298K} = +206.16 - 241.82x\ ^{kJ}/_{mol} \tag{9}$$

which can be performed with (catalytic) or without a catalyst (thermal) [1]. The composition range for most autothermal reforming must be in the range of $0 < x < 1$ [2], leading to a heat of reaction range between +206.16 kJ/mol and -35.66 kJ/mol. When a catalyst is used, ATR can be performed at temperatures as low as 650°C and pressures from1-25 atmospheres of gage pressure. Removing the catalyst raises the minimum reaction temperature to 950°C, making thermal ATR difficult to perform in most reactors due to quenching and low residence times lowering the reaction temperature possible in the reforming vessel [2].

This research will focus on thermal partial oxidation reforming and autothermal reforming to negate the need for a catalyst. Based upon the research of Marbach *et al* [3] a porous inert media will be used in the combustion/reforming zone to maintain the high temperatures and longer residence times required for these processes to be accomplished without a catalyst. All air used in the reactor will be preheated to temperatures from 500°C to 750°C, and then will be passed through 2 annuluses to further preheat the fuel/water/air mixture before entering the porous inert media. Additionally, Sadasivuni *et al*. [4] have shown that if a flow-blurring fuel injector is used,

a longer-chained hydrocarbon can be atomized and used in this combustor, providing the opportunity to release more hydrogen per mass of hydrocarbon.

The described fuel reforming process will produce syngas. Syngas, or synthetic gas, is the name given to a gas mixture that primarily contains carbon monoxide (CO) and hydrogen (H_2). While the composition of syngas primarily consists of carbon monoxide and hydrogen, small amounts of carbon dioxide, unburned hydrocarbons, and other products are present, depending on the fuel source. The primary components of syngas, carbon monoxide and hydrogen, have energy content and are therefore combustible. Because of this, syngas can be used as a fuel source for internal combustion engines. Syngas is a vital fuel source to be explored because of its potential in fuel flexible technologies, as well as clean burning combustion processes.

The fundamental concept in syngas production is to oxidize the fuel, obtaining carbon monoxide and hydrogen as the main products of the reaction. This thermal oxidation is a partial oxidation process. This partial oxidation of the hydrocarbon fuel, characterized by the amount of oxidizer, is an exothermic reaction. The governing equation for syngas production is:

$$C_mH_n + (0.5)mO_2 = mCO + (0.5)nH_2 \quad (10)$$

assuming pure oxygen as the oxidizer. The main advantage of this partial oxidation technique is the small size of the reactor and the rapid response to changes. However, the main disadvantages lie with the low H_2:CO ratio and the danger of handling premixed air/fuel mixtures. In addition, if air is used as the oxidizer, a high fraction of nitrogen dilutes reformate hydrogen content. Because of the high temperatures involved, thermal partial oxidation does not need the assistance of a catalyst [5]. The fuel/oxidizer mixture being preheated allows operation at very lean or rich equivalence ratios and contributes to low NO_x emissions. The combustion temperature of porous inert media (PIM) burners can be made relatively low; however, they are still high enough to cause degradation of the porous material. Recently, porous ceramic foams and discrete ceramic matrices have become available and advanced this field of study greatly. Porous ceramic foams have good temperature resistance, but their durability suffers from cracking due to thermal cycling [6].

3. Chemkin Simulation for Thermal Fuel Reforming

Very rich fuel air mixture is expected to lead to incomplete combustion products producing syngas (CO and H2) along with unburned hydrocarbon, CO2 and H2O. However, combustion without use of a catalyst is expected to result in a penalty that would be realized through lower efficiency of conversion to syngas as a fraction of fuel would be completely burned to sustain combustion reactions. Chemical Equilibrium calculations were carried out for n-Heptane fuel in chemkin software to check the product species mole fraction and adiabatic temperature associated with it. These chemical equilibrium computations were carried out at 5atm pressure and inlet reactant temperatures varying from 300K to 600K in steps of 50K.

From practical standpoint for sustaining fuel rich combustion, equivalence ratios resulting in minimum of adiabatic temperatures in vicinity of 1400K would be expected. Figure 1 below shows that equivalence ratio around 2.8 with inlet temperature of 500K or higher would likely provide combustible mixture providing fairly high fuel conversion to syngas (CO and H2 mixture). Note that the best conversion efficiencies are expected to be obtained at ultra-rich

equivalence ratios. However, a flame temperature higher than the adiabatic flame temperature needs to be maintained at high equivalence ratios in order to have high conversion efficiency as well as mixture to be combustible. Fuel preheating serves this purpose. Shortcoming of thermal reforming is that it needs fraction of fuel to be completely burnt in absence of the catalyst to sustain the reforming reactions.

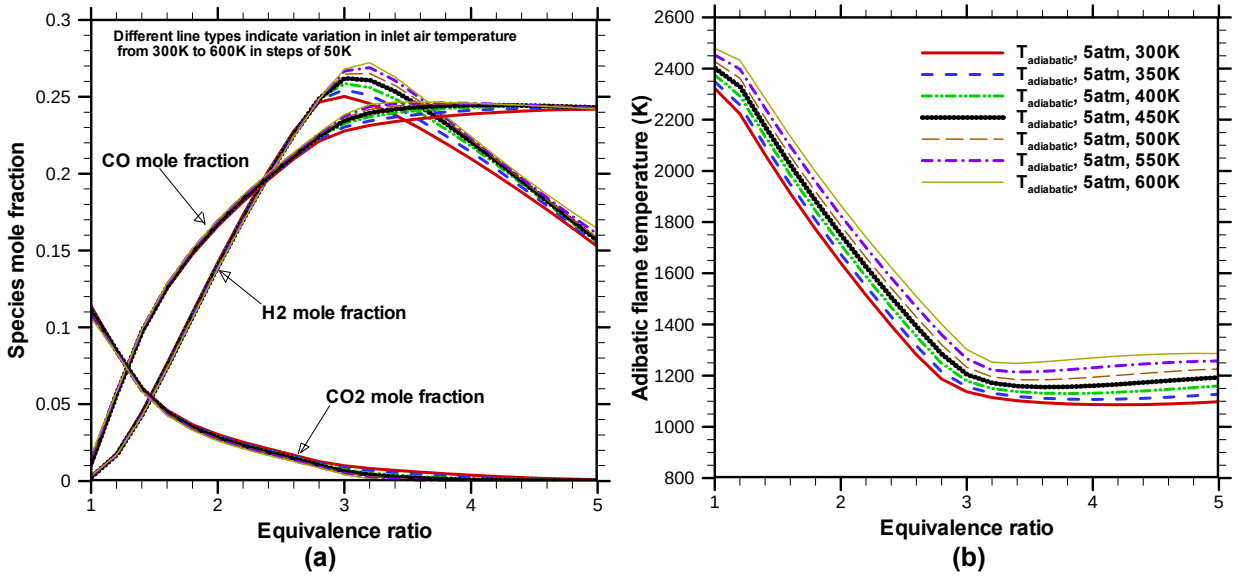

Figure 1: Equilibrium calculations for n-heptane at 5atm pressure for different inlet temperatures (a) species mole fraction and (b) Adiabatic temperature.

From design fabrication stand point of view, information such as minimum residence time to sustain the reactions is required. Perfectly stirred reactor (PSR) model in chemkin is utilized with n-heptane mechanism to get more information from stand point of chemical kinetics (viz. minimum residence time or maximum flow rates that would ensure the autothermal reforming reactions are sustained). Such information would aid in geometrical design of the reformer with that would be critical in fabrication process for suppling syngas at flow rates demanded by particular application (e.g. application in vehicular transport or power generation combustion systems).

Based on chemical equilibrium calculations, conditions of equivalence ratio of 2.8 with inlet reactant temperature of 500K are used with perfectly stirred reactor model simulation in chemkin to see the effect of residence time on the combustion product species mole fraction. Note that residence time estimation would allow to estimate the geometric dimensions at given flow rate. Besides, PSR yields close to realistic estimation of syngas production since it employs the detailed kinetic mechanism (for n-heptane in present case). Chemkin simulation shows that minimum residence time of 1.8 ms is required for combustion to take place and adiabatic temperature in excess of 1400K indicates that it is more likely to practically carry out the combustion at these conditions for n-Heptane fuel. Based on these preliminary estimates from chemkin simulation, a heat recirculation based fuel reformer model concept employing porous media combustion is developed and discussed in section to follow. The flexibility of such reformer model is that porous media can easily be coated with catalyst to conduct catalytic partial oxidation concept based fuel reforming.

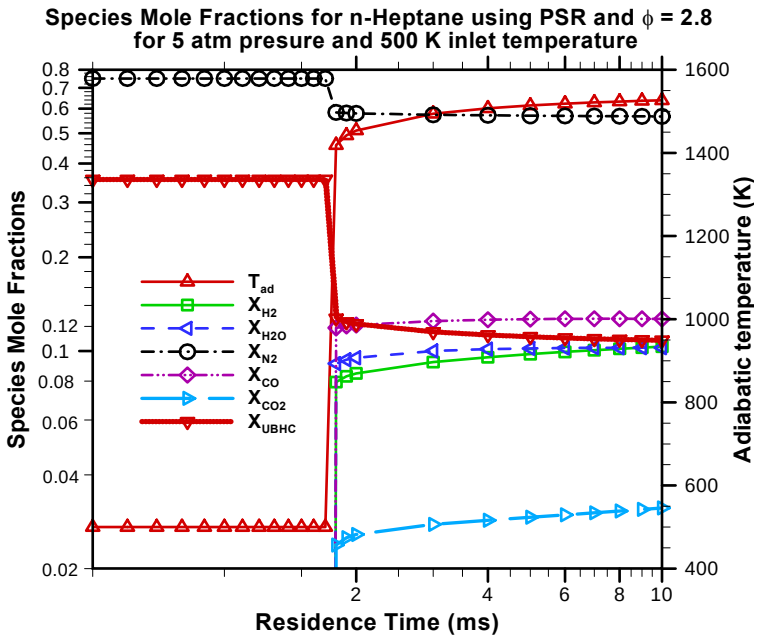

Figure 2. Simulated thermal fuel reforming of n-heptane with perfectly stirred reactor model in chemkin.

3. Thermal Fuel Reforming Model Development:

Figure 3 shows heat recirculation concept based fuel reformer incorporating concentric tube configuration. Innermost tube is typical porous media combustor and fuel air mixture passes through annular region on outside surface of the porous media combustor resulting in preheating and vaporization of liquid fuel prior to entering porous media combustor. The porous inert media stabilizes the flame within the matrix of the porous media, which allows for higher burning speeds. The porous media creates a super adiabatic effect, which consists in the local occurrence of higher flame temperatures compared to the adiabatic temperature of a free flame at the same equivalence ratio. The recirculation of the sensible enthalpy of the flame products occurs through convection from the hot gas to the inert matrix, which, in turn, transfers the heat through conduction and radiation to the matrix upstream of the flame, which then heats the incoming unburned mixture. The higher thermal conductivity of the solid matrix compared to the conductivity of the gas enhances the effective heat transfer from the products to the reactants. Thus, the overall effect is a substantial preheat of the fresh mixture. The subsequent faster kinetics, because reaction rate is a function of temperature, lead to higher flame speed and to the extension of the flammability limit of the fuel/oxidizer mixture. The higher temperature compared to the free flame conditions allows initiation and chain-branching mechanisms to occur at ultra-rich equivalence ratios. The extended rich flammability limit allows partial oxidation conditions to be established, thus allowing the stripping of the hydrogen out of the original fuel molecule. Consequently, the main products of the reactions are molecular hydrogen and carbon monoxide, along with nitrogen and other species in low concentrations [7].

Using the PIM burner for combustion has several advantages over open flame combustion, especially with liquid fuels. Conventional burners must be rather large and maintained at high temperature for there to be sufficient time for the liquid fuel to completely evaporate and burn. A PIM burner has a very high radiant output due to the high emissivity of ceramic materials.

The porosity provides the fuel with a convoluted path through a homogeneously radiant field that is without cold boundaries, ensuring droplet vaporization and contributing to complete reaction. Thus, the PIM burner, having a high volumetric energy output due to a high burning rate, can be compact. Another advantage is the potentially low emission of NO_x. Low NO_x emission is due to droplet vaporization and mixing in the porous media [6]. Because of these advantages, a PIM burner can help with the production of syngas.

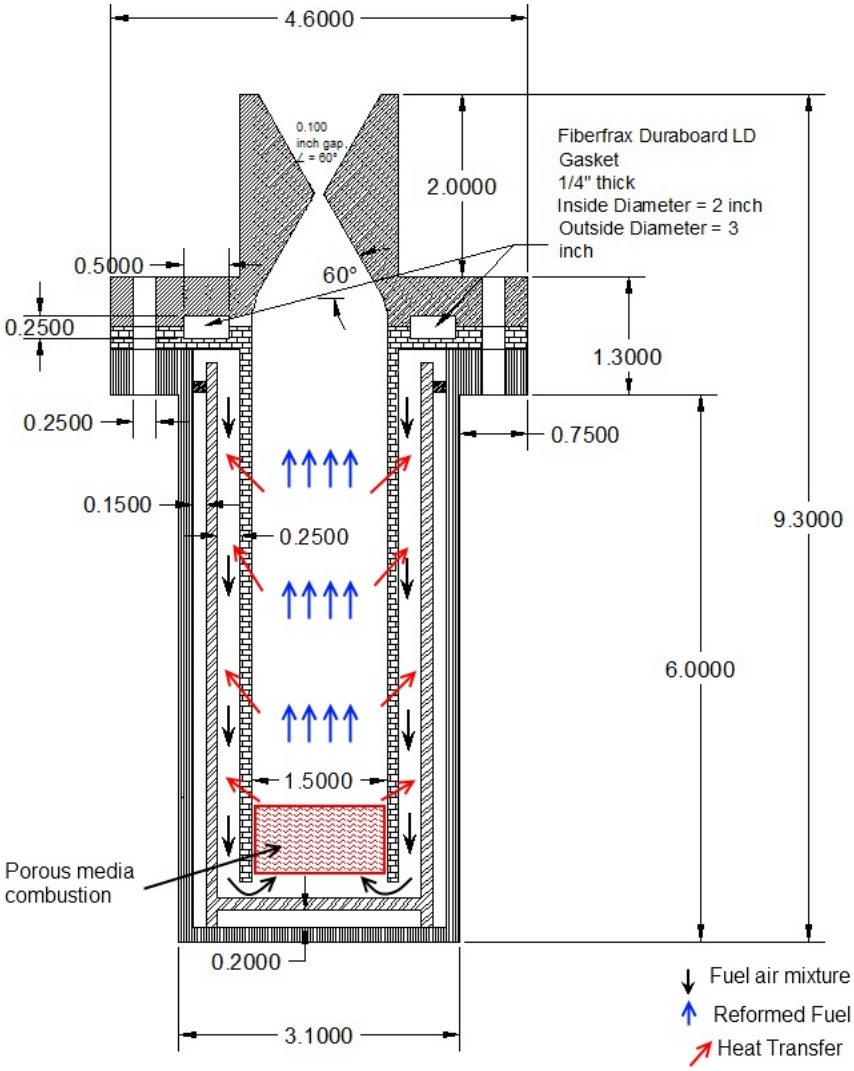

Figure 3. Fuel reformer model based on heat recirculation concept combustor

4. Experimental Setup

A fuel reformer has been designed to reform fuel using a porous inert media. Silicon carbide, porous ceramic foam, is being used as the porous media for the designed fuel reformer. Three ½″ discs have been placed inside the combustion chamber. This creates 1.5 inches of porous material within the combustion chamber. From research undertaken in the area of syngas production, it is shown that the best conversion efficiencies are reached at ultra-rich equivalence ratios. This conversion efficiency is increased if the fuel/oxidizer mixture is preheated. This

will be achieved by pre-heating the air to around 700ºC. Note that, the fuel reformer is designed as a waste heat recovery system. Thus, heat released in the combustion process is also used to pre-heat the incoming fuel/oxidizer mixture. This, along with the radiation of the porous media, will pre-heat the incoming fuel/oxidizer mixture. This will allow for higher conversion efficiency because fewer pollutants (NO_x, CO_2) are present in the products. Pre-heating the incoming mixture allows one to initiate combustion at a temperature below the narrow combustion band (1300ºC-1600ºC), while also keeping pollutants very low. This process saves energy and reduces pollutant emissions [8].

Figure 4 shows experimental setup for autothermal fuel reformer. It consists of the fuel reformer, fuel pump, air flow meter, air heater, and air supply. The air is supplied to the fuel reformer from an air compressor. The air flow meter is an Aalborg mass flow meter, specifically for air, with a range of 0 to 200 SLPM. This particular mass flow meter is model GFM57. The air heater is made by Sylvania and it can heat the air temperature up to 1400ºF. This air heater is a threaded inline heater with a 4kW output capacity and can be operated at high flow rates. The only requirement for this air heater is a 220 V power source. The fuel pump is manufactured by Cole-Parmer Instrument Company with a model number 752K-30. This fuel pump is a positive displacement pump that uses a P23 model pump head. The P23 pump head displaces 0.261 mL per revolution. It is a 0.1 hp Micropump with a 60 to 3600 rpm range and a minimum flow rate of 15 mL/min.

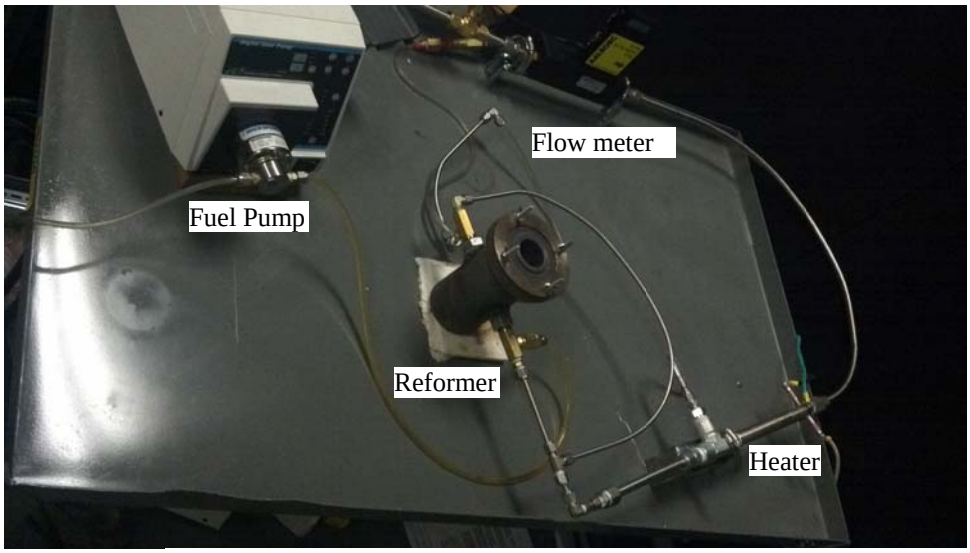

Figure 4: Autothermal fuel reformer setup

The fuel reformer uses a dual-fuel system. The fuel reformer uses methane for ignition and the other hydrocarbon fuel is gradually introduced into the fuel reformer. It uses methane for ignition to heat the combustion chamber and porous media. Then, the hydrocarbon fuel is gradually introduced into the system until only the hydrocarbon fuel is entering the fuel reformer. The hydrocarbon fuel will then be partially oxidized to produce syngas. In present case experiments were carried out on methane alone. The emissions of the fuel reformer will be tested using the V & F Gas Analyzer. The V & F Gas Analyzer uses an Ion Reaction Mass Spectrometer (IRMS), an Electron Impact Mass Spectrometer (EIMS), and a filtration system to analyze the emissions. From the measured emissions, the conversion ratio of the useable energy

content will be evaluated. These tests will be performed for a given fuel until the optimum operating conditions are determined. Analyzing the emissions data will allow us to calculate what conditions produce the greatest conversion efficiencies. This optimum operating condition will come at ultra-rich conditions. The greatest challenge for this experiment is maintaining a high flame temperature at ultra-rich conditions. If a high flame temperature can be maintained, high conversion efficiencies will be attained. This will be achieved by preheating the incoming fuel/oxidizer mixture. The air (oxidizer) is being preheated before it enters the combustion chamber. In addition, the fuel reformer is designed with a waste heat recovery system to preheat the incoming fuel/oxidizer mixture. These characteristics of the system allow for ample preheating.

5. Preliminary Results

Methane was first tested at equivalence ratios ranging from 0.75 to 3.0. These preliminary tests were performed without preheating the air and with the combustion chamber open to atmospheric conditions. The airflow rate remained constant at 50 SLPM throughout the tests and the fuel flow rate was varied to achieve various equivalence ratios. For methane, a fuel flow rate of 4.0 SLPM was used to achieve an equivalence ratio of 0.75. A fuel flow rate of 8 SLPM was used to achieve an equivalence ratio of 1.5. A fuel flow rate of 10.7 SLPM was used to achieve an equivalence ratio of 2.0. A fuel flow rate of 13.35 SLPM was used to achieve an equivalence ratio of 2.5. Lastly, a fuel flow rate of 16 SLPM was used to achieve an equivalence ratio of 3.0. Figure 5 depicts methane combustion at the stated equivalence ratios can be seen below.

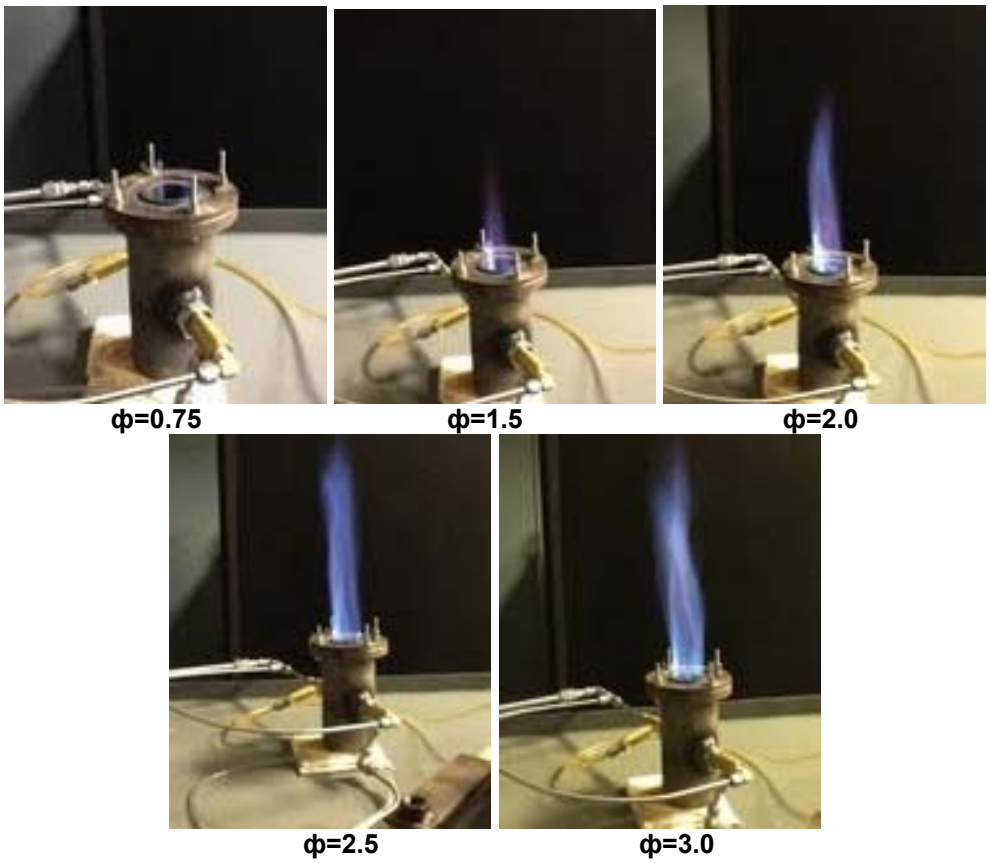

Figure 5: Thermal Fuel reformer in operation on methane at various equivalence ratios.

Emissions data was collected at an equivalence ratio of 2.0 for methane. These results showed the emissions contained 15.1% CO and 2.1% H_2. These results are lower than expected because the air was not preheated and the combustion chamber was open to the atmosphere. Higher concentrations of carbon monoxide and hydrogen are expected when the air heating system is running, as well as when the combustion chamber is pressurized. In future, V&F analyzer would be calibrated for various species of interest (viz. H_2, CO, CO_2, N_2, H_2O vapor, unburned hydrocarbon species, aldehydes and ketones) to carry out detailed analysis of syngas produced.

6. Concluding Remarks

A fuel reformer has been designed to produce syngas from any hydrocarbon fuel via autothermal partial oxidation with the assistance of a porous inert media. The porous medium aids in stabilizing the flame, as well as pre-heat the incoming fuel/oxidizer mixture. The designed fuel reformer is a promising device for the production of syngas. The greatest conversion efficiencies are expected to come at ultra-rich equivalence ratios as can be seen in the Chemkin Simulation results from Figure 1. Although the simulation is for n-heptane, other hydrocarbon fuels are expected to behave similarly. The demonstration of rich methane combustion at equivalence ratio of 3 in the reformer shows its potential to achieve higher conversion efficiencies. Future experiments would demonstrate working on other long chain hydrocarbon fuel such as diesel, biodiesel, soybean oil and glycerol.

7. Acknowledgments

This research was supported by US Department of Energy Award EE0003134.

References

[1] Ogden, J., *Review of Small Stationary Reformers for Hydrogen Production* (2001) 1-49.
[2] Ayabe S., Omotoa H., Utaka T., Kikuchi R., Sasaki K., Teraoka Y., & Eguchi K., *Applied Catalysis A: General, 241(2003), 261-269.*
[3] Marbach T. L., Agrawal A. K., *ASME J. Eng. Gas Turbines Power* 127 (2005) 307-313.
[4] Sadasivuni V., Agrawal A.K., *Proceedings of the Combustion Institute* **32** (2009) 3155-3162.
[5] Pastore, A., *Syngas Production from Heavy Liquid Fuel Reforming in Inert Porous Media* 2010.
[6] Howell, J.R., Hall, M.J., Elizey, J.L., *Prog. Energy Combustion Science* **22** (1996) 121-145.
[7] Pastore, A., Mastorakos, E., *Fuel 90* (2010) 64-76.
[8] Huang, Y., Chao, C.Y.H., Cheng, P., *International Journal of Heat and Mass Transfer* **45** (2002) 4315-4324.

8th U. S. National Combustion Meeting
Organized by the Western States Section of the Combustion Institute
and hosted by the University of Utah
May 19-22, 2013

Ultra High Speed Rainbow Schlieren Deflectometry for Statistical Description of Turbulent Low-Density Jets

Pankaj S Kolhe and Ajay K Agrawal
Department of Mechanical Engineering, University of Alabama, Tuscaloosa AL 35487

Rainbow schlieren deflectometry (RSD) integrated with ultra high-speed digital imaging system is used to characterize a turbulent low-density jet through statistical description of path-integrated measurements. Unlike deconvoluted measurements, statistics of deflectometric data are free from approximations and can be utilized as benchmark to compare and validate path-integrated quantities derived from large-eddy and/or direct numerical simulations. Deflectometry techniques allow non-intrusive measurements to probe difficult to access near-field region of the jet exit. The experimental system consists of a helium jet discharged vertically into ambient air from a round tube injector of 4 mm inside diameter (d) and jet exit Reynolds number of 4000. Rainbow schlieren apparatus was configured to cover the near-field axial range of 0 to 20d downstream of injector exit at pixel resolution of 124 μm, temporal resolution of 20 μs, and image acquisition rate of 50,000 frames per second to capture a wide range of turbulent structures. Deflectometric measurements are utilized to estimate integral length scales, integral time scales, and wavenumber spectra at different locations in the flow field. Results show characteristics of a developing turbulent flow in the axial direction with gradual establishment of order. Space-time cross-correlation functions show that the Taylor's hypothesis of frozen flow turbulence is strictly not applicable in the near-field. Two point cross-correlation functions in transverse direction represent high intensity fluctuations and possible noise source locations.

1. Introduction

Turbulent mixing of two or more fluids is an important problem for non-reacting and reacting flow systems. Prediction, design and control of such systems require accurate turbulence models validated using experimental measurements. The properties of turbulent flow are often described in terms of velocity correlations in space, in time, and in space-time. Space-time cross correlations are of practical interest as a tool to analyze inhomogeneity and anisotropy, and find application in characterization of turbulent boundary layer[1-2], turbulent shear layer[3-4] and turbulent jets/flames[5-7]. Limiting cases of space-time cross correlation provide information about integral length and time scales and wavenumber and frequency spectra through simple mathematical manipulation. These characteristics alone are sufficient and necessary to provide statistical description of turbulent flows[8-15].

Spacetime correlations have been extensively applied to laser-based velocity measurement techniques such laser Doppler velocimetry (LDV) and particle image velocimetry (PIV) to analyze turbulent flows. However, spatial resolution for point measurement diagnostics poses a problem due to finite probing volume along with inconsistent data rates[16-18]. Neumann et al.[19, 20] have demonstrated high resolution measurement of minimum 15μm separation for velocity measurements to alleviate issue of achieving autocorrelation of unity for zero time lag and Taylor's micro scales by employing two separate point measurement probing systems. Extensive application of spacetime correlations of velocity measurements have been carried out for characterizing turbulence or noise propagation and noise source detection. Similar applications of spacetime cross correlations are employed to measure scalar fields using optical deflectometry. Doty and McLaughlin[21], Veltin et al[22] and Tam et al[23] have utilized autocorrelations and cross correlation to detect noise source location and its propagation for high speed jets. Strong negative radial direction autocorrelation information is utilized to locate noise sources as they represent locations of high intensity fluctuations. Davis and group[24-26] have used schlieren or shadowgraph technique along with cross beam technique or Abel inversion for single beam to estimate cross correlation of local field and energy spectrum. They employed cross beam correlation technique with laser beam schlieren, a point measurement technique. However, Kolhe and Agrawal[27] have proposed correction to the cross beam correlation algorithm and accuracy of reconstruction of cross correlation function using cross beam technique is suspect without incorporating correction. Nevertheless, they have demonstrated capability of deflectometric measurements to carry out such measurements to characterize turbulent flow.

In this study, rainbow schlieren deflectometry integrated with high-speed imaging is utilized to obtain spacetime cross correlation measurements together with integral length and time scales, and wavenumber spectra of deflection angle data. Although spacetime cross correlation is computed for path integrated data, it provides a measure of local field as wavenumber spectra of path integrated data is simply a scaled spectrum of local field and the link is established through well known Fourier central slice theorem. Similarly, integral length and time scales for deflection angle data would be representative of large scale structures along the path length as they would be providing dominant contribution to deflection angle statistics. Therefore, the statistics of deflection angle data are important from perspective of statistical description of turbulent flow. Besides, deflection angle statistics can be measured very precisely, and do not involve any assumptions or simplifications. Hence, deflection angle statistics can be used as bench mark to validate numerical models through comparison of synthetic schlieren data from numerical simulations to experimental schlieren data. Sections to follow demonstrate the potential of rainbow schlieren deflectometry to characterize near field developing turbulent flow of a helium jet.

2. Experimental Setup

Figure 1 shows the schematic diagram of the experimental setup. The flow system consists of compressed gas cylinder to supply helium, a mass flow meter (Aalborg GFM37 with range 0-100 standard liters per minute or slpm), a needle valve to control the helium flow rate, and 50 mm long tube injector with wall thickness of 0.5 mm and inner diameter, d = 4 mm. The flow at the tube exit is expected to be nearly fully-developed. Helium is discharged vertically into the quiescent air environment kept at ambient conditions. Helium volume flow rate is kept constant at 80 standard liters per minute (slpm). The jet exit Reynolds number $\left(\mathrm{Re} = \rho \cdot V \cdot d / \mu\right)$ is 4000 and the jet exit Richardson number $\left(Ri = \frac{g \cdot d}{V^2} \cdot \left(\frac{\rho_{air} - \rho_{He}}{\rho_{He}} \right) \right)$ is 2.1×10^{-5}. Thus, the jet exit flow is considered as momentum-dominated. At ambient conditions, the Schimdt number $\left(Sc = \nu / D_0\right)$ is 1.7 for helium air jet indicating viscous diffusion and molecular mass diffusion effects are comparable. However, the turbulent Schmidt number reported in literature for turbulent helium-air jet (at jet exit Re ≈ 4000) is 0.7 as evaluated by Panchapakesan and Lumley[28].

High-speed RSD system is configured to acquire simultaneous whole-field measurements at 50,000 Hz with image size of 304x448 pixels and 124 μm per pixel spatial resolution in field of view. Schlieren system consists of the light source aperture, collimating and decollimating lenses, a rainbow filter, and a digital color camera (ultra high-speed Photron SA-5). Light to the rectangular source aperture (50 μm wide and 3 mm high) is supplied by a 650 mW mounted LED with 1200 mA LED driver from Thor labs. The light source aperture is placed at the focal point of the collimating lens (82 mm diameter and 300 mm focal length) to obtain parallel beams that pass through the test medium causing refraction. The refracted rays are refocused to form the source image at the focal point of the decollimating lens (82 mm diameter and 300 mm focal length) where the rainbow filter is placed. The filtered images are acquired by high-speed digital camera with 50 mm focal length lens. The schlieren system is aligned to ensure precise alignment of the optical axis of all of the components. The camera onboard memory allows acquisition of 42,017 schlieren images continuously for the test conditions. In the present study, 42,000 images in tiff file format are used to conduct statistical analysis of deflectometric data.

The RSD technique employs a continuously graded color filter to measure the deflection angle of light rays passing through the test medium[29]. Visible white light consists of multiple wavelengths or colors. The rainbow filter serves as a continuously graded filter since it transmits light of a particular wavelength (or color) corresponding to the location on the filter. This color-coding scheme facilitates computation of lateral (or axial) displacement of light rays at the filter plane corresponding to each pixel location in the color schlieren image. However, a priori knowledge of color distribution in the rainbow filter is required. The rainbow filter is sensitive only to the transverse displacements if the source aperture and color strips on the filter are aligned with the axial direction, and vice versa. In this study, the source aperture and color strips on the rainbow filter were oriented to detect the ray displacements in the transverse direction only.

In the RSD technique, hue, saturation, and intensity (HSI) color model is used to characterize the color by a single attribute, hue. Figure 2 shows the filter calibration curve expressed in terms of hue versus transverse location on the filter plane. The calibration curve is obtained by computing the average hue of the color schlieren image acquired without the test medium (background schlieren image) while the rainbow filter is traversed in increments of 50 μm. Schlieren images without and with the test medium are acquired without disturbing the optical system or the

experimental setup. This practice ensures that a given pixel in the schlieren image maps the same physical location without or with the test medium.

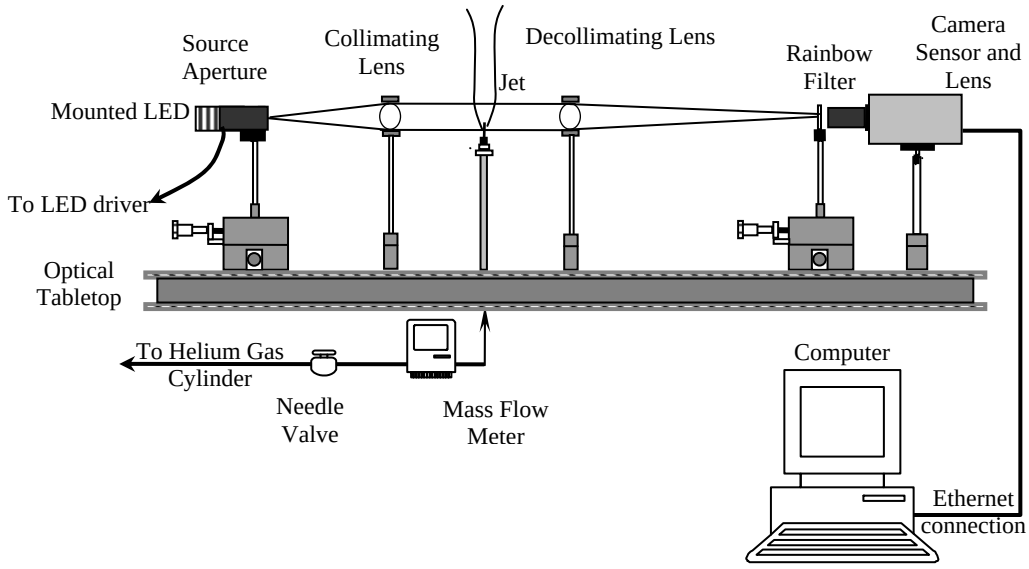

Figure 1: Schematic of experimental setup.

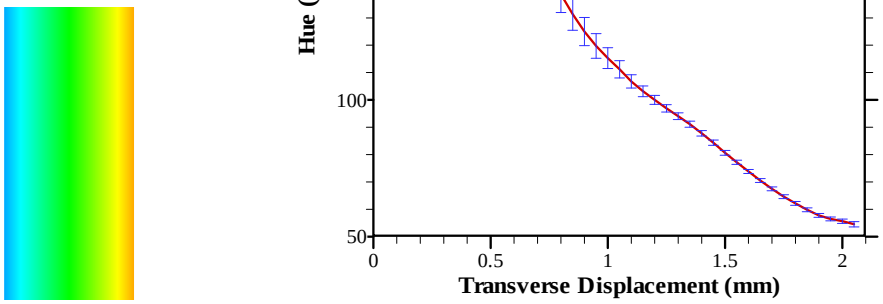

Figure 2: Asymmetric rainbow filter and hue calibration curve.

3. Data Analysis

In the analysis procedure, the measured hue (H) at each pixel location in the schlieren image is converted to the transverse position on the filter plane (χ) using the filter calibration curve and Equation 1.

$$\chi(H) = \chi_i + \frac{\chi_{i+1} - \chi_i}{H_{i+1} - H_i} \cdot (H - H_i) \tag{1}$$

where (χ_i, H_i) and (χ_{i+1}, H_{i+1}) are filter calibration coordinates closest to the measured hue, H. Next, the transverse deflection angle of the light ray is found from Equation 2.

$$\Theta = \frac{\chi(H) - \chi(H_b)}{f} \tag{2}$$

where, $\chi(H_b)$ is the transverse filter position pertaining to the background hue, H_b and *f* is focal length of the decollimating lens (*f* = 750 mm). Note that filter calibration curves are used together with Equations 1 and 2 to obtain transverse deflection angle at each pixel location of instantaneous schlieren image. Thus, RSD yields simultaneous measurements across the whole field of view. The instantaneous fluctuation in deflection angle and its intensity is computed from Equation 3(a) and 3(b), where x, z, and t refer, respectively, to transverse coordinate (x), longitudinal streamwise coordinate (z), and time (t).

$$\Theta'(x,z,t) = \Theta(x,z,t) - \frac{1}{T}\cdot\int_0^T \Theta(x,z,t)\cdot dt \tag{3a}$$

$$\overline{\Theta'^2(x,z)} = \frac{1}{T}\cdot\int_0^T \left[\Theta'(x,z,t)\cdot\Theta'(x,z,t)\right]\cdot dt \tag{3b}$$

The instantaneous deflection angle fluctuation is utilized to estimate various quantities such as spatial, temporal, and space-time cross correlation functions, integral length and time scales, and power spectral density. Note that temporal autocorrelations at any transverse and axial location can be estimated from the instantaneous deflection angle measured at that location and employing Equation 4, where 'τ' is the temporal separation. Local spatial correlations in transverse direction at particular axial location can be defined on instantaneous basis as shown in Equation 5, where 'ζ' is the transverse separation distance. Time-averaged spatial correlation at particular longitudinal plane is estimated from Equation 6, which is also used to obtain the wavenumber spectra given by Equation 7.

$$R_t(x,z,\tau) = \frac{\int_0^T \left[\Theta(x,z,t) - \overline{\Theta(x,z)}\right]\cdot\left[\Theta(x,z,t+\tau) - \overline{\Theta(x,z)}\right]\cdot dt}{\overline{\Theta'^2(x,z)}} \tag{4}$$

$$R_x(\zeta,z,t) = \frac{\int_{-X}^{X} \left[\Theta(x,z,t) - \overline{\Theta(x,z)}\right]\cdot\left[\Theta(x+\zeta,z,t) - \overline{\Theta(x+\zeta,z)}\right]\cdot dx}{\int_{-X}^{X}\left[\Theta'(x,z,t)\right]^2\cdot dx} \tag{5}$$

$$\overline{R_x}(\zeta,z) = \frac{1}{T}\cdot\int_0^T R_x(\zeta,z,t)\cdot dt \tag{6}$$

$$P(k_x,z) = \frac{1}{2X}\cdot\int_{\zeta=-X}^{\zeta=X} \overline{R_x}(\zeta,z)\cdot e^{-i\left(\frac{\pi\cdot k_x}{X}\right)\cdot\zeta}\cdot d\zeta \tag{7}$$

Note that in above equations integrating limits 'X' and 'T' represent the bounds on spatial (transverse) and temporal dimensions for the acquired deflectometric data. Instantaneous integral length scale and local integral time scales are estimated using Equations 8 and 9 respectively. Note that upper integral limits in Equation 8 and 9 represent minimum positive lag in space or time for which correlation drops to zero.

$$l(z,t) = \int_0^{\zeta^*} R_x(\zeta,z,t)\cdot d\zeta \tag{8}$$

$$i_t(x,z) = \int_0^{\tau^*} R_t(x,z,\tau)\cdot d\tau \tag{9}$$

Two point cross correlations in longitudinal streamwise direction and transverse direction are estimated using Equation 10 and 11 respectively.

$$R_{zt}(\varsigma = \Delta z, \tau) = \frac{\int_0^T \left[\Theta(x,z,t) - \overline{\Theta(x,z)}\right]\cdot\left[\Theta(x,z+\Delta z,t+\tau) - \overline{\Theta(x,z+\Delta z)}\right]\cdot dt}{\sqrt{\overline{\Theta'^2(x,z)}\cdot\overline{\Theta'^2(x,z+\Delta z)}}} \tag{10}$$

$$R_{xt}(\zeta = \Delta x, \tau) = \frac{\int_0^T \left[\Theta(x,z,t) - \overline{\Theta(x,z)}\right]\cdot\left[\Theta(x+\Delta x,z,t+\tau) - \overline{\Theta(x+\Delta x,z)}\right]\cdot dt1}{\sqrt{\overline{\Theta'^2(x,z)}\cdot\overline{\Theta'^2(x+\Delta x,z)}}} \tag{11}$$

Note that, the deflectometric measurements are obtained in near-field, where Taylor's frozen flow hypothesis might not apply. However, eddy convection velocity at any location is estimated from longitudinal direction spacetime cross correlation with non-zero time lag where a peak is observed with spatial separation.

4. Results and Discussion

Experiments were conducted by traversing tube injector in upstream direction to obtain schlieren measurements in the near field ranging from 0 to 20d from the injector exit. Statistics of transverse deflection angle were obtained using 42,000 images captured at 50,000 frames/sec rate. Figure 3(a) and 3(b) show the mean and variance of transverse deflection angle. Note that mean deflection angle is both positive and negative because of the asymmetric filter used to map varying deflections in turbulent flows. Nonetheless, Figure 3 shows excellent flow symmetry in time-averaged mean and variance of deflection angle data. The magnitude of the mean deflection angle is rather small, only between 0 and 0.0005 radian.

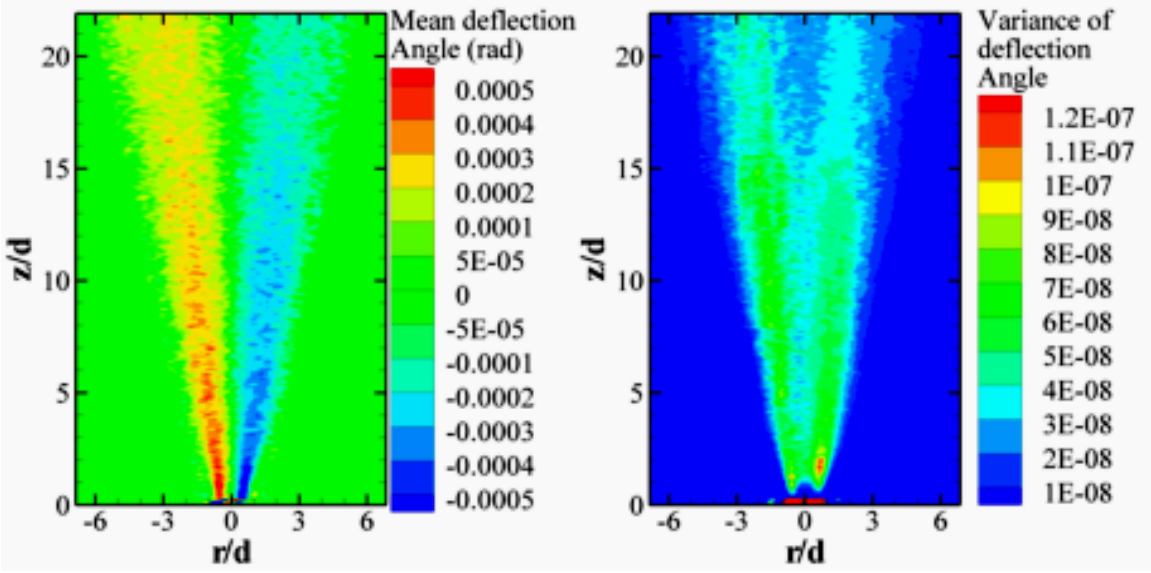

(a) **(b)**

Figure 3. Whole field deflection angle statistics in turbulent helium jet at Re = 4000 and jet diameter d = 4mm (a) mean deflection angle in radians, and (b) variance of deflection angle.

Figure (4) shows effect of sampling duration on statistics of the deflection angle. Sampling duration of 0.84 seconds corresponding to 42,000 images seems to achieve statistical stationarity as evident from variation in mean and variance of deflection angle at different radial and axial locations in Figure (4).

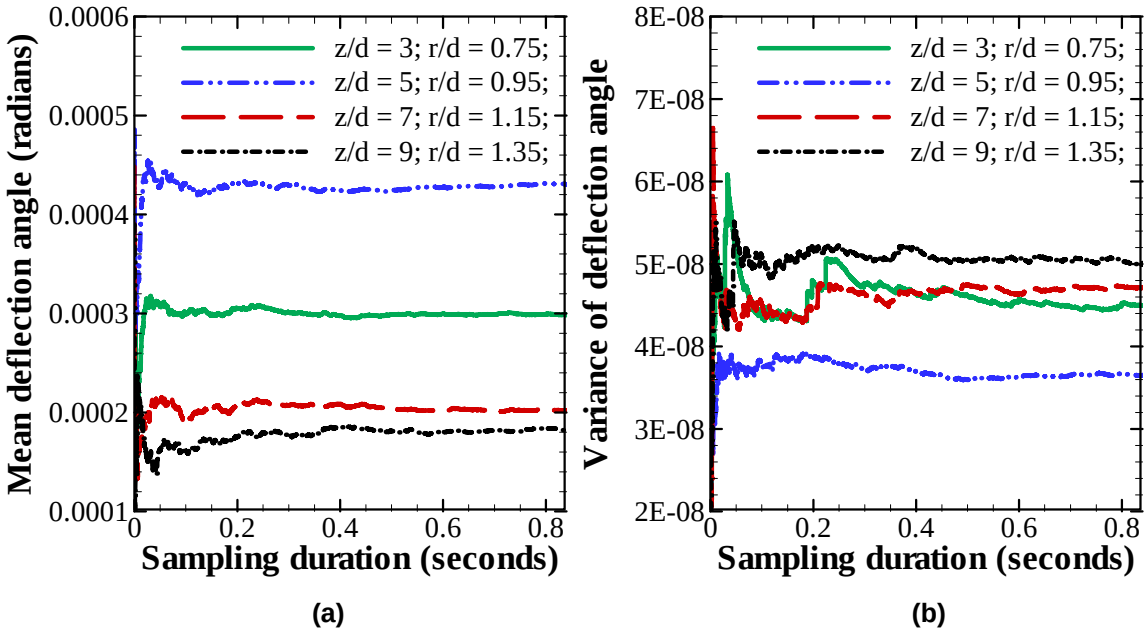

Figure 4. Effect of Sampling Duration on (a) mean, and (b) variance of deflection angle.

Figure 5(a) shows the autocorrelation function in time at different axial and radial locations inside the mixing region. Note that time lag is normalized using d and bulk mean axial velocity at injector exit. At downstream axial locations, a widening of the autocorrelation function is observed indicating higher correlation over extended period; the correlation decreases to zero for normalized time separation of about 30 at z/d = 5 but of over 60 at z/d = 20. This variation in autocorrelation function indicates faster fluctuations in the near field and slower fluctuations at downstream locations, which is consistent with reduction in concentration and velocity gradients by mixing and entrainment.

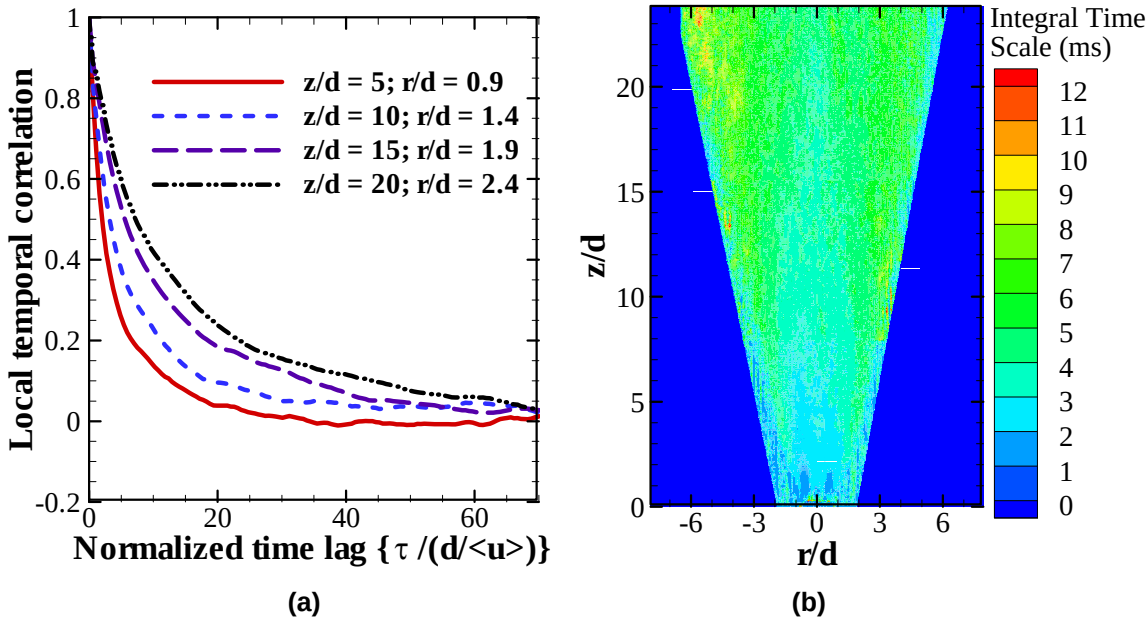

Figure 5. (a) Local temporal correlations, and (b) integral time scales in turbulent helium jet.

Figure 5(b) shows integral time scales associated with the observed flow field. Note that, the integral time scale characterizes the time over which turbulent fluctuations are correlated in the largest eddy along the path-length. Integral time scale varies from 2 ms to 12 ms in the field of view spanning from 0 to 20 d in longitudinal direction and from -6d to 6d in the transverse direction. Increase in integral time scale at downstream locations indicates larger eddies moving at a smaller convection velocity. The integral time scale in region r/d = ±0.5 and z/d < 5 is rather small, indicating features of the potential core with unmixedness. The integral time scale is small near jet center region and higher in the shear layer region for all longitudinal locations.

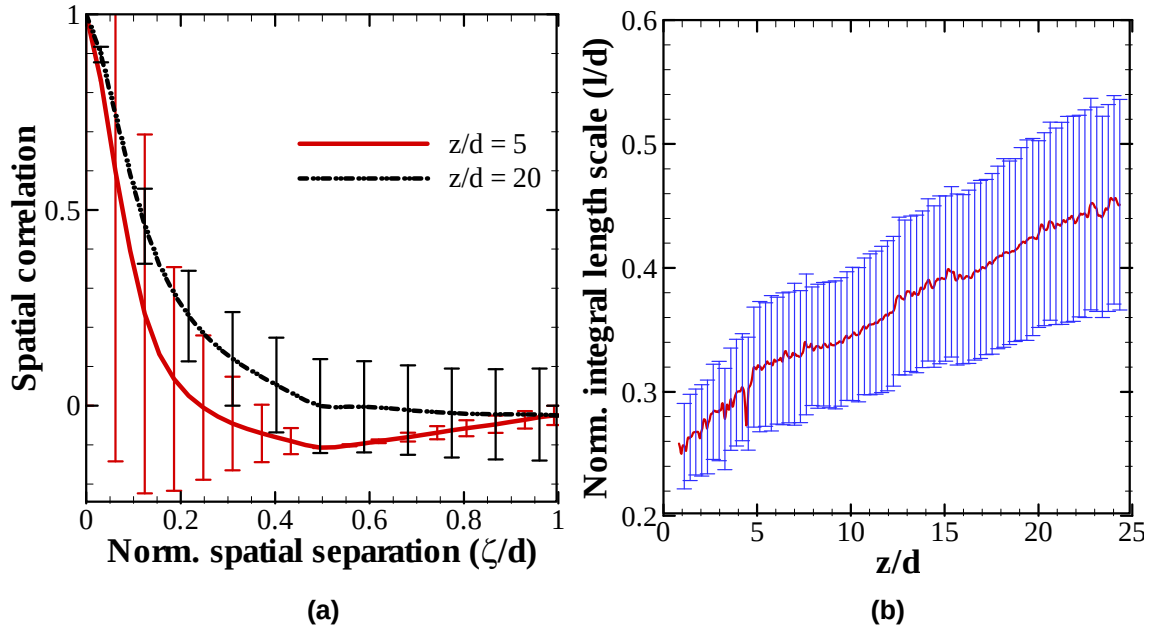

Figure 6. (a) Time averaged spatial correlation, and (b) integral length scale variation

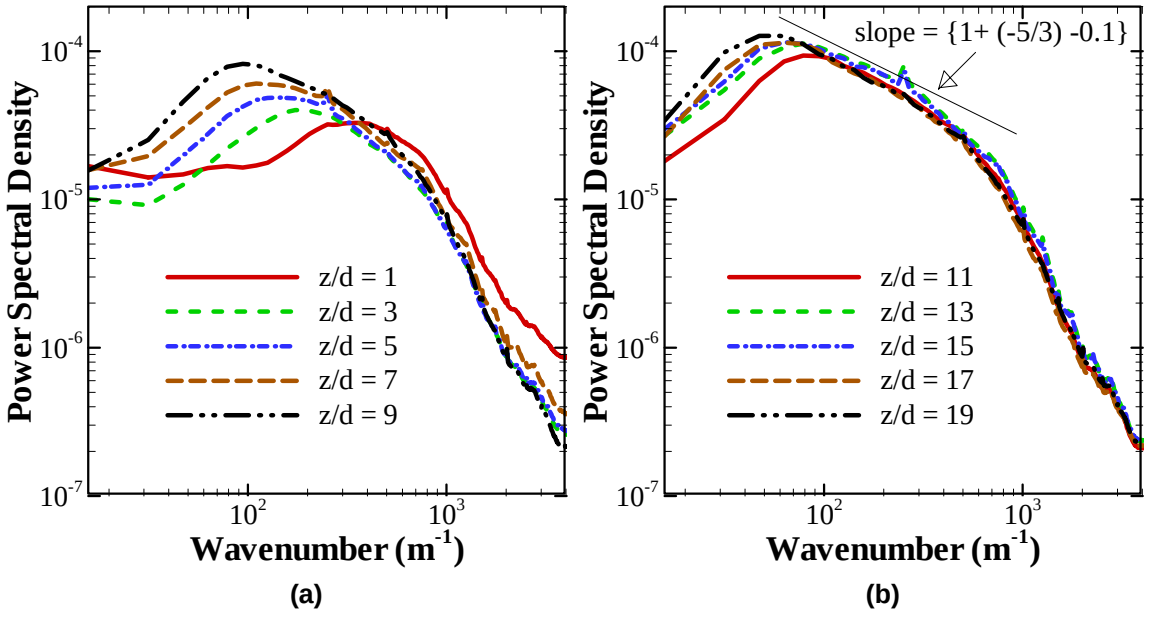

Figure 7. Wavenumber spectra for path integrated deflection angle data at different axial locations (a) near injector axial locations, and (b) downstream axial locations.

Figure 6(a) shows profiles of spatial correlation function in transverse direction at z/d = 5 and 20. Note that profiles represent time-averaged mean values and error bars show standard deviation in the spatial correlation for each spatial separation. Results show that spatial correlation decreases to negative values much faster for z/d = 5 in comparison to

that for z/d = 20. A steeper drop in spatial correlation indicates smaller eddies at z/d = 5 compared to those at z/d = 20. The standard deviation in spatial correlation is large for smaller separation (ζ/d < 0.2) at z/d = 5, and for larger spatial separations ζ/d > 0.3 at z/d = 20. Note that, at downstream locations jet spreading would result in higher eddy convection velocities in transverse direction, which would contribute to larger variation in spatial correlation in transverse direction. Figure 6(b) shows the variation in mean integral length scale in the longitudinal direction. Note that mean and variance of integral length scale at a longitudinal plane characterize the largest eddy size along the light of sight. Increasing trend in mean integral length scale with increasing longitudinal coordinate indicates growing size of larger eddies at downstream locations. Mean integral length scales normalized by jet exit diameter varies from 0.25 to 0.45 for z/d = 0 to ≤ 20. Within the same distance, the variance of integral length scale varies from 0.07d to 0.2d. Thus, within 95% confidence interval, the normalized integral length scale varies between 0.22 and 0.29 at z/d = 1 and between 0.35 and 0.54 at z/d = 24. Clearly, eddies are smaller near the injector and they gradually grow larger in the streamwise direction.

Figure (7) shows the wavenumber spectra of developing scalar turbulence from z/d = 1.0 to 19. Wavenumber spectra at z/d = 1 represents random flow without order since spectral energy content is spread over wide range of wavenumbers. Interestingly more than 70% of energy content is distributed in wavenumbers (in 1/m) between 100 and 1000. This result is in stark contrast to fully developed turbulence spectrum where most of energy content is distributed in lower wavenumbers (< 100 m^{-1}). From Figure (7), spectral energy content shift is evident at downstream locations. For z/d > 10, a clearly defined spectral slope in inertial subrange of wavenumbers (100 m^{-1}< k <1000 m^{-1}) is observed, which is typical turbulent flow characteristics representing energy cascading, i.e., transfer of energy from larger eddies to smaller eddies. Development of spectral energy content represents evolution from random chaotic flow to developing turbulent flow. Observed spectral slope of -0.766 in inertial subrange of wavenumbers can be seen as {1 + (-5/3) - 0.1} split. Note that deflection angle data are path-integrated data and hence, expected spectral slope in accordance with Kolmogorov's hypothesis would be {1 + (-5/3)} and an additional split of -0.1 can be attributed to intermittency in turbulent flow. From Figure (7), it can be seen that for z/d > 3, spectral energy content at lower wavenumbers (k < 100 m^{-1}) is increasing, which is consistent with growth of large eddies at downstream locations. For wavenumbers k < 60 m^{-1} spectral energy content is observed to decrease from between z/d =1 and 3. This result can be attributed to shrinking of jet potential core and transfer of energy to intermediate range wavenumbers.

Figure (8) and Figure (9) show two-point cross correlation function in longitudinal and transverse direction respectively at axial locations of z/d = 1, 3 and 5 in jet center region (r/d = 0) and mixing region with r/d = 0.75. Autocorrelation is limiting case of cross correlation function with zero spatial separation. General trend of peak autocorrelation at zero time lag and peak cross correlation at non-zero time lag is clearly evident. However, peak magnitude of cross correlation is observed to be lower than the autocorrelation magnitude at same time lag. This trend indicates clear mismatch in eddy convection velocity and mean flow velocity. In fact, Taylor's hypothesis is not valid for this near field region, which is anticipated from wavenumber spectra depicting transition to turbulent flow. From Figure (8), it is clear that two-point cross correlation function for any spatial separation shows higher correlation at zero time lag along jet center compared to that in the mixing region. Besides, peak magnitude of cross correlation for any given spatial separation is higher along jet center compared to mixing region. Note that higher correlation is indicative of more coherent structure near jet center compared to mixing region, which is expected as corroborated by mean integral length, integral time scales, and spectral energy distribution in the near injector field. The time lag corresponding to peak correlation is smaller at jet center compared to mixing region because of higher convection velocity at jet center. For z/d =1, autocorrelation function drops much more precipitously for mixing region compared to jet center region. Such drastic change in autocorrelation shape is not observed at any of the downstream locations indicating that structures immediately downstream of tube injector exit do not maintain coherence for longer duration in the mixing region. This result can be explained from strong mixing entrainment associated with large gradients in scalar and velocity fields. From Figure (9), it is evident that two point cross correlation for spatial separations of Δx/d = 0 and 1/32 are nearly matching each other. Note that experimental deflection angle data is a measure of transverse gradient in present case and hence two point cross correlation for small spatial separation in transverse direction would resemble each other.

Transverse direction two point cross correlations at jet center in Figure (9) show similar features. Peak magnitude falls at non zero time lag indicating movement of coherent structures in transverse direction. However, in mixing region non-negative peak magnitude at non-zero time lag is not observed possibly indicating much faster structural changes in transverse direction to detect any coherent nature. Besides, if mean flow direction is aligned with longitudinal direction, spacetime correlations in transverse direction would not show any resemblance with Taylor's hypothesis[9]. Strong negative correlations for zero time lag observed at axial location of z/d = 1 in transverse direction cross correlations are generally important from acoustics point of view (viz. noise source detection and propagation) as it reveals high intensity

fluctuation region and possible noise source. These strong negative correlations at zero time lag are observed for spatial separation of the order of integral length scale pointing to contribution from large scale eddies to possible noise generation {refer Figure 6(b)}.

Figure (10) and Figure (11) show two point cross correlation function in longitudinal and transverse direction respectively at axial locations of z/d = 8, 12 and 16 in jet center region and mixing region (r/d = 1.7). Trend of lower magnitude of peak cross correlation for any spatial separation compared to autocorrelation for the same time lag associated with peak cross correlation continued at jet center {refer Figure 10}. However, in mixing region peak magnitudes of cross correlations are nearly matching autocorrelation magnitudes for the same time lag particularly at location downstream of z/d = 12. Therefore, it can be concluded that there is discrepancy in eddy convection velocities and mean flow velocities with jet center region showing much larger discrepancy. Observation of higher autocorrelation magnitude at reference fixed point for same time lag for which cross correlation shows peak indicates that Taylor's frozen flow hypothesis is strictly not valid. However, the transition trend observed here likely indicates Taylor's hypothesis to be applicable in fully turbulent regime at far downstream axial locations. For axial locations $z/d \geq 8$, transverse direction cross correlation with reference fixed point at jet center shows neat tend of peak cross correlation at non zero time lag indicating resolvable transverse direction movement of eddy structures {refer Figure (11)}. Such trend is not observed in mixing region although positive magnitudes of cross correlation are indicative of eddy structures maintaining coherence over short period. Again, to eliminate any bias axial deflection angle can be used to estimate spacetime cross correlation in transverse direction or use different axial locations for fixed reference point and second point of desired spatial separation in transverse direction.

Figure (12) shows, large eddy convection velocity at different radial and axial locations. Note that, eddy convection velocity is estimated using the spatial separation and non zero time lag for which peak cross correlation magnitude is observed. From Figure (12) it can be seen that for a fixed reference point, convection velocity estimation is dependent on spatial separation used for two point cross correlation. This variation in convection velocity for different spatial separation is indicative of the fact that Taylor's frozen flow turbulence hypothesis is not valid. Eddy convection velocity for any transverse location is seen to decrease at downstream axial locations. Peak velocity in the vicinity of 60 m/s is observed at jet center at z/d = 1. Note that bulk mean tube injector exit velocity for the experimental operating conditions is 106.5 m/s. In mixing region for axial locations $z/d \geq 8$, the eddy convection velocity range is observed to vary from 8 m/s to 16 m/s. Variation in eddy convection velocity with spatial separation used for two point correlation reduces at downstream axial locations, where Taylor's hypothesis is applicable. Fisher and Davies[6] have proposed approach of using moving frame autocorrelation to estimate eddy convection velocity for the case where discrepancy in mean flow velocity and eddy convection velocity exists. Moving frame autocorrelation corresponds to envelop of all cross correlations for different spatial separations. Convection velocity is then estimated using spatial separation of cross correlation and the time lag for which the cross correlation and moving frame autocorrelation are tangent to each other. This approach yields uniform convection velocity for any spatial separation at given reference point.

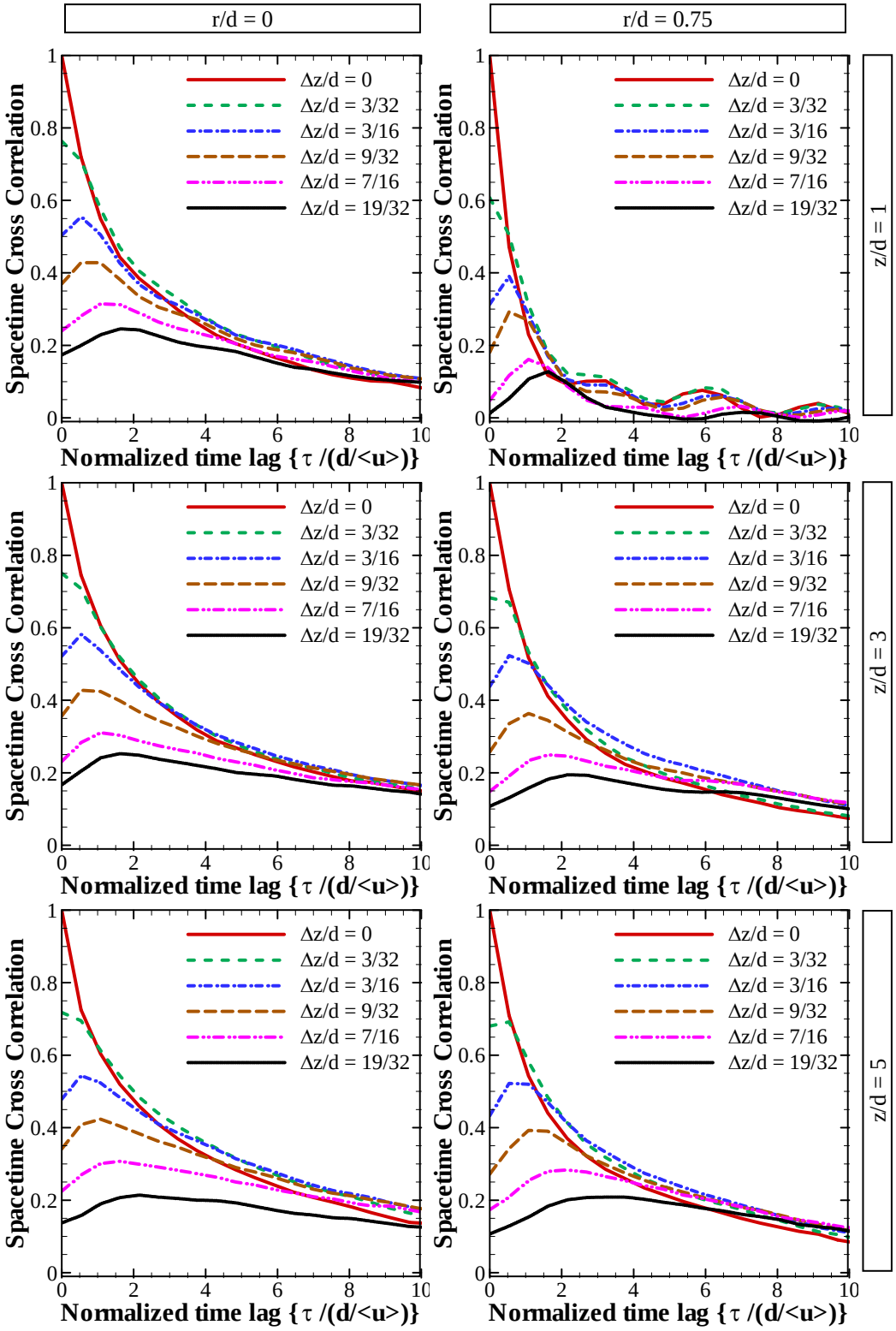

Figure 8. Space-time cross correlations in longitudinal direction (a) at jet center r/d = 0, and (b) in shear layer region r/d = 0.75.

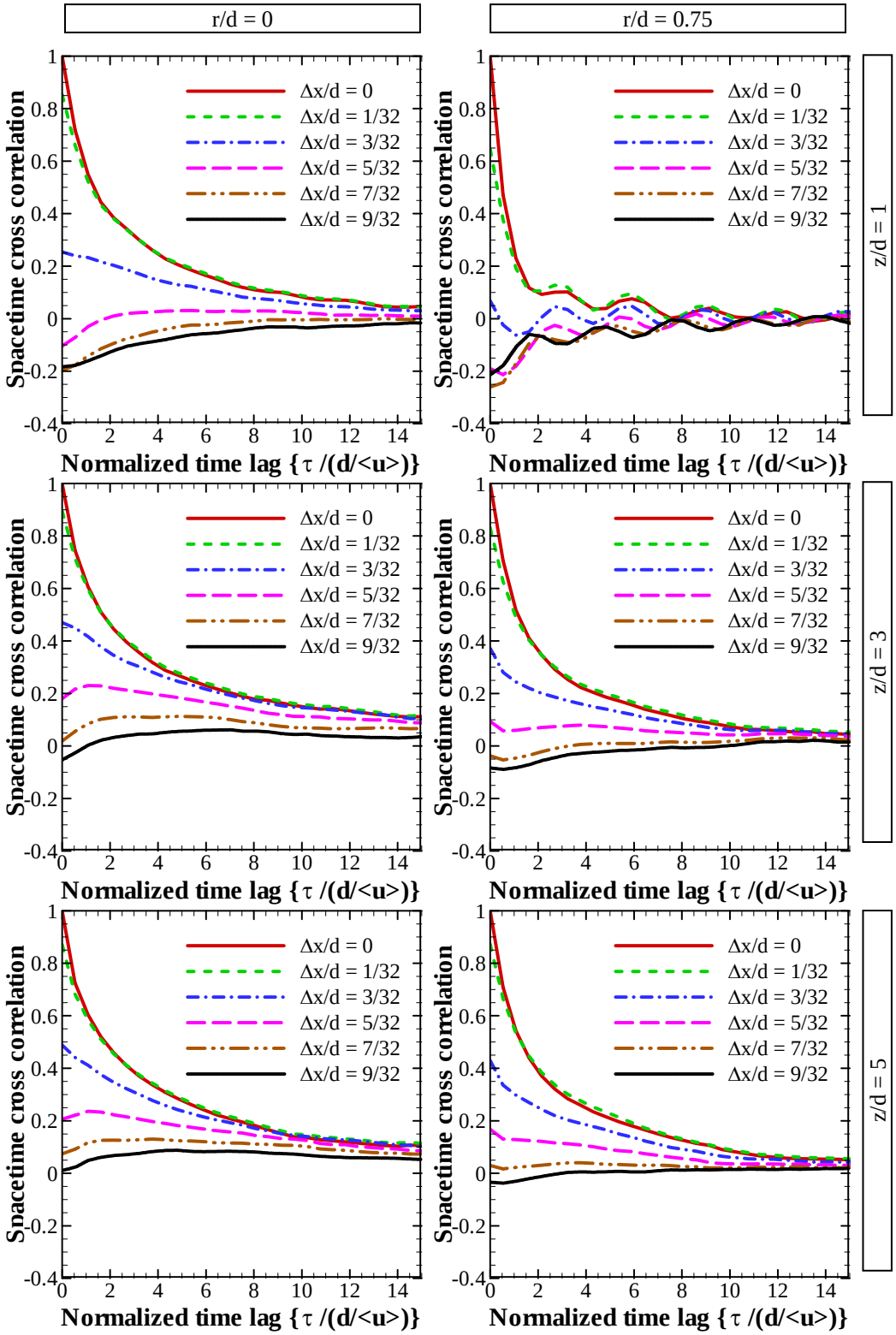

Figure 9. Space-time cross correlations in transverse direction (a) at jet center r/d = 0, and (b) in shear layer region r/d = 0.75.

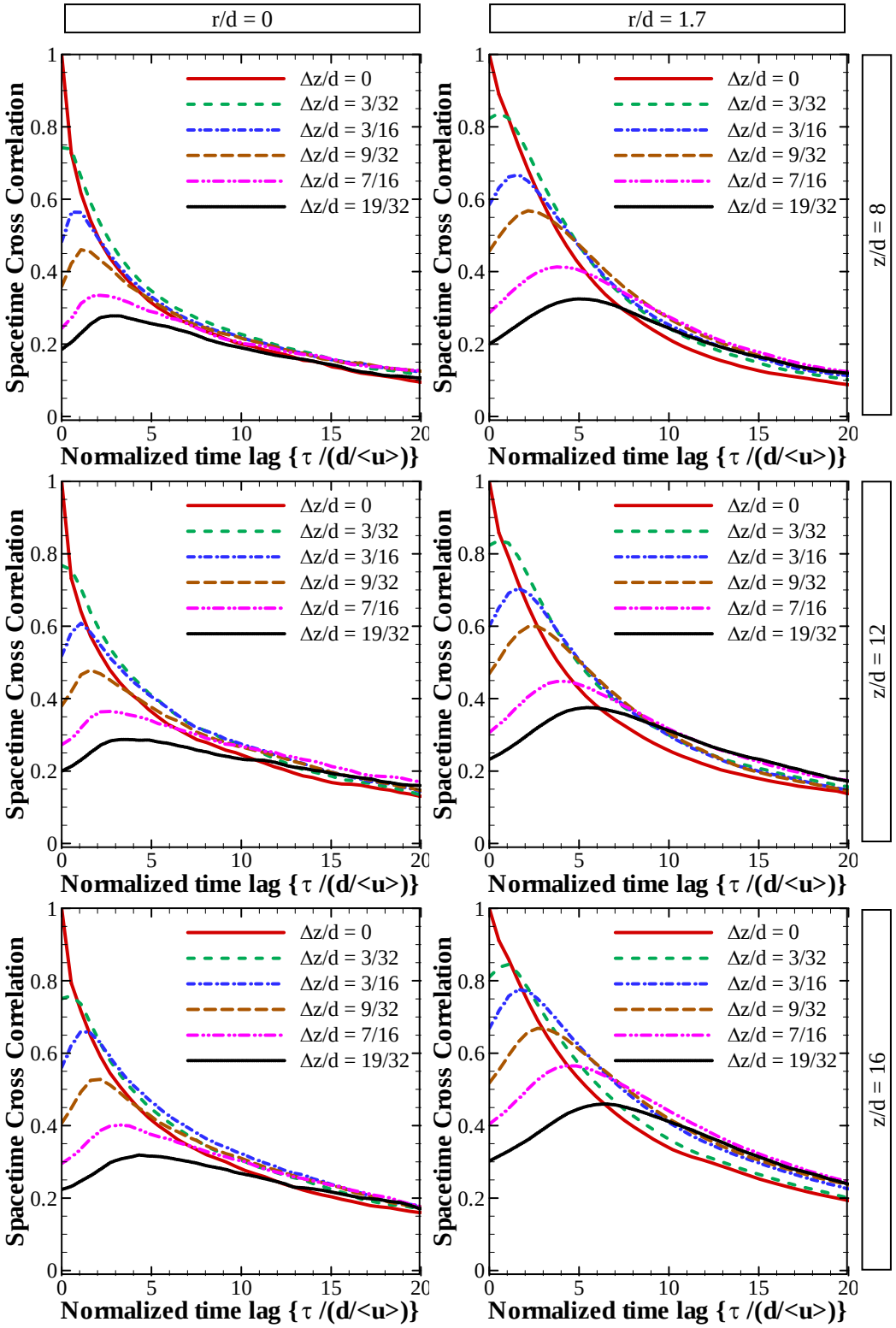

Figure 10. Space-time cross correlations in longitudinal direction (a) at jet center r/d = 0, and (b) in shear layer region r/d = 1.7.

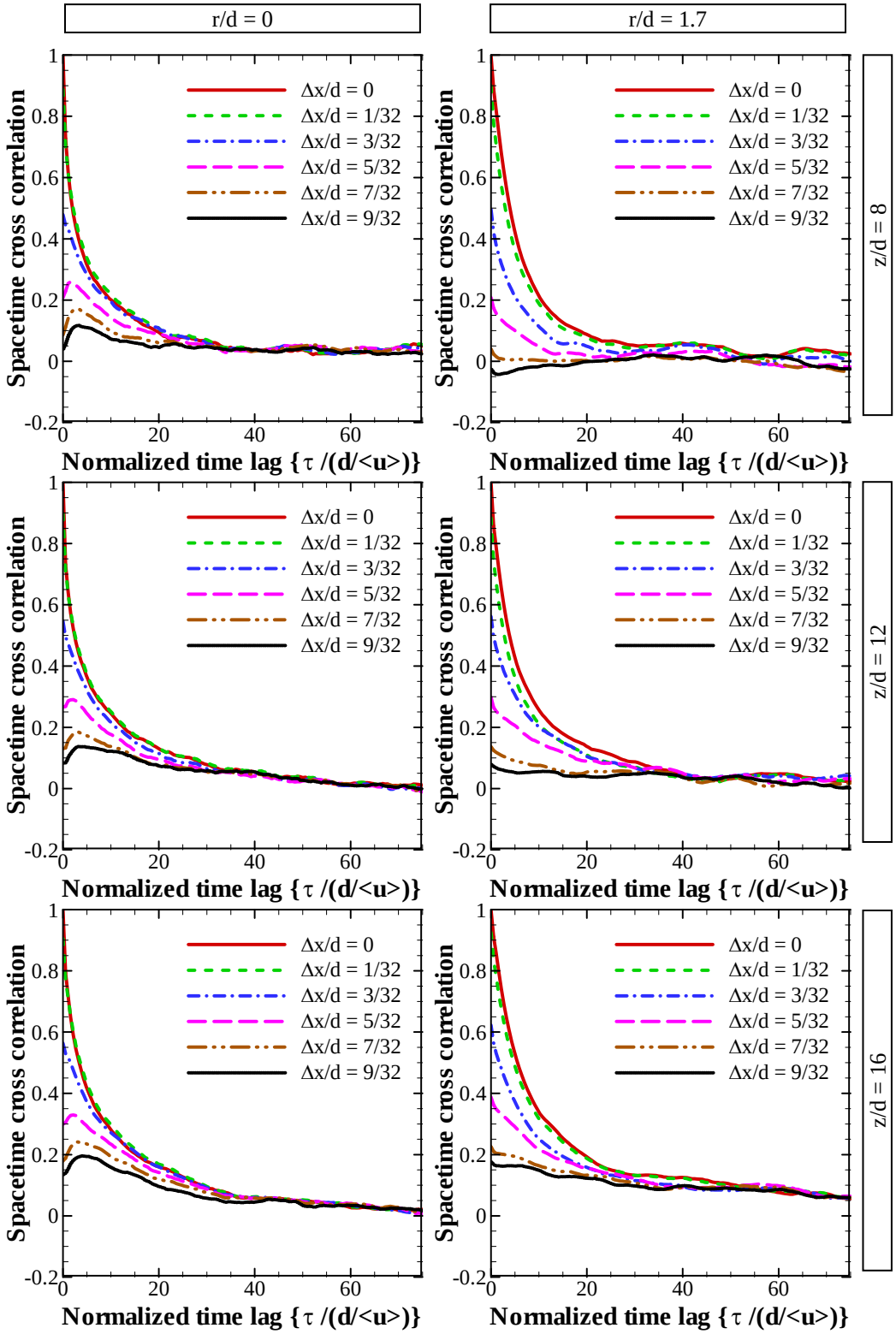

Figure 11. Space-time cross correlations in transverse direction (a) at jet center r/d = 0, and (b) in shear layer region r/d = 1.7.

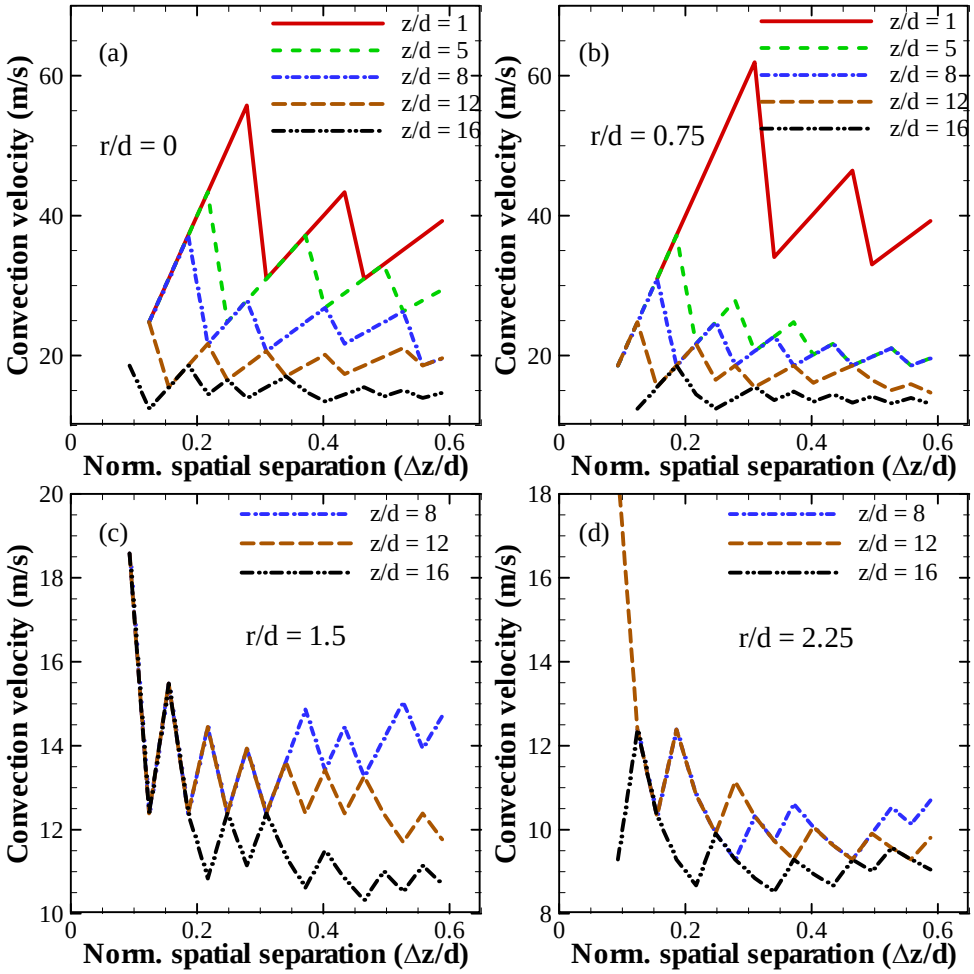

Figure 12. Convection velocity based on space-time cross correlations in longitudinal direction at different axial and radial locations.

5. Conclusions

Ultra high speed rainbow schlieren deflectometry is used to characterize helium jet turbulent scalar field in near tube injector exit region using statistical description of path integrated deflection angle data. Integral length and time scales along with wavenumber spectra clearly indicate the turbulent flow is developing and near field with z/d < 10 shows the establishment of order in spectral energy content for different wavenumbers, which otherwise represents random chaotic flow. Wavenumber spectrums and two-point cross correlation functions at different locations in flow field provide evidence that Taylor's frozen flow hypothesis is not valid in near field region of z/d < 20. Spectral slope of -2.3/3 {= 1 + (-5/3) -0.1} in inertial wavenumber range for path integrated data shows existence of intermittency. Increase in integral length scale provides the evidence of growing large scale structures in the flow which is corroborated by increase in spectral energy content at lower wavenumbers for axial locations downstream of z/d = 3. z/d < 3 represents the region where spectral energy content is redistributed to reflect order in energy content at different wavenumbers, a typical characteristic of turbulent flow showing departure from total chaos. Increased integral time scales indicate slower fluctuations at downstream axial locations as a result of decrease in scalar and velocity gradients due to continued mixing and entrainment. Mean flow velocity is higher in jet core region resulting in lower integral time scales and smaller time lag separation associated with peak cross correlation magnitude in longitudinal direction. Two-point cross correlation in longitudinal direction can provide mean convection velocity component in that direction. However, potential for complete velocimetry through spacetime cross correlations would be realized only after detection of mean flow direction, and evaluation of elliptic model for spacetime cross correlation footprint seems to be possible avenue. Strong negative two-point cross correlation at zero time lag for given spatial separation provides information about possible contribution to the noise generation from eddy structure sizes of the order of spatial separation.

Acknowledgements

This research was supported in part by US Department of Energy Award EE0003134.

References

[1] Favre A, Gaviglio, J. and Dumas R. Space time double correlations and spectra in a turbulent boundary layer. *J. Fluid Mech.* (1957), vol. 2, pp. 313-342.
[2] Favre A, Gaviglio, J. and Dumas R. Further space time correlations of velocity in a turbulent boundary layer. *J. Fluid Mech.* (1958), vol. 3, pp. 344-356.
[3] Jachens A., Schumacher J., Eckhardt B., Knobloch K. and Fernholz H. H. Asymmetry of temporal cross-correlations in turbulent shear flows. *J. Fluid Mech.* (2006), vol. 547, pp. 55–64.
[4] Champagne F. H., Harris V. G., and Corrsin S. Experiments on nearly homogeneous turbulent shear flow. J. Fluid Mech. (1970), vol. , pp. 81-139.
[5] Davies P.O.A.L. and Fisher M. J. The characteristics of the turbulence in the mixing region of a turbulent round jet. . *J. Fluid Mech.* (1963), vol. 15, pp. 337-367.
[6] Fisher M. J. and Davies P.O.A.L. Correlation measurements in a non-frozen pattern of turbulence. . *J. Fluid Mech.* (1964), vol. 18, pp. 97-116.
[7] Cenedese A., Romano G. P., and Felice F. D. Experimental testing of Taylor's hypothesis by L.D.A. in highly turbulent flow. Expt. Fluids, (1991), vol. 11, pp. 351-358.
[8] Taylor G.I. The spectrum of turbulence. Proc. R. Soc. Lond. A, (1938), vol. 164, pp. 476-490.
[9] Smol'yakov A.V., Tkachenko V.M. The Measurement of Turbulent Fluctuations: An Introduction to Hot-Wire Anemometry and Related Transducers. Edited by Bradshawa P and Translated by Chomet S and published by Springer Verlag, Berlin Heidelberg, New York. (1983).
[10] Lin C.C. On Taylor's hypothesis and the acceleration terms in the Navier Stokes equations. Quart. Appl. Math., (1952), vol. 10, pp. 295-306.
[11] Zhou Q., Li C. M., Lu Z. M. and Liu Y. L. Experimental investigation of longitudinal space-time correlations of the velocity field in turbulent Rayleigh-Bénard convection. *J. Fluid Mech.*, (2011), vol. 683, pp. 94-111.
[12] Dahm W. J. A.and Southerland K.B. Experimental assessment of Taylor's hypothesis and its applicability to dissipation estimates in turbulent flows. *Phys. Fluids*, (1997), vol. 9, pp. 2101-2107.
[13] Gledzer E. On the Taylor hypothesis corrections for measured energy spectra of turbulence. Physica D, (1997), vol. 104, pp. 163-183.
[14] He X., He G, and Tong P. Small-scale turbulent fluctuations beyond Taylor's frozen-flow hypothesis. Physical Review E,(2010), vol. 81, pp. 065303:1-4.
[15] Lumley J. L. Interpretation of Time Spectra Measured in High ‐ Intensity Shear Flows. Phys. Fluids, (1965), vol. 8, pp. 1056-1062.
[16] JG Eriksson, RI Karlsson. An investigation of the spatial resolution requirements for two point correlation measurements using LDV. *Expt fluids*, (1995), vol.18, pp.393-396.
[17] Ducci A., Yianneskis M. Analysis of errors in the measurement of energy dissipation with two-point LDA. *Expt.Fluids*, (2005), vol. 38, pp. 449–460.
[18] Kerherve F., Fitzpatrick J., Chatellier L. A sensitivity analysis of the point reference global correlation (PRGC) technique for spatio-temporal correlations in turbulent flows. *Expt. Fluids*, (2008), vol. 44, pp.577–589.
[19] Neumann M., Shirai K., Buttner L., Czarske J. A novel laser doppler array sensor for measurements of micro-scale velocity correlations in turbulent flows. *Flow Meas. and Inst.*, (2012), vol. 28, pp. 7–15.
[20] Neumann M., Shirai K., Buttner L., Czarske J. Two-point correlation estimation of turbulent shear flows using a novel laser Doppler velocity profile sensor. *Flow Meas. and Inst.*, (2009), vol. 20, pp. 252–263.
[21] Doty M. J., McLaughlin D. K. Space–time correlation measurements of high-speed axisymmetric jets using optical deflectometry, *Expt. Fluids*, (2005), vol. 38, pp. 415–425.
[22] Jérémy Veltin J., Day B. J., and McLaughlin D. K. Correlation of flowfield and acoustic field measurements in high-speed jets, *AIAA J.*, (2011), Vol. 49, pp. 150-163.
[23] Tam C. K. W., Viswanathan K., Ahuja K. K. and Panda J. The sources of jet noise: experimental evidence. *J. Fluid Mech.*, (2008), vol. 615, pp. 253–292.
[24] Davis M. R. Determination of turbulent flow properties by a penetrating beam dynamic shadowgraph method. *J. Phys. E: Sci. Instrum.*, (1987), vol. 20, pp. 1271-1277.
[25] Winarto H. and Davis M. R. Fluctuations of density, pressure and temperature in a turbulent mixing region. *Proc. R. Soc. Lond. A*, (1984), vol. 395, pp. 203-228.

[26] Davis M. R. and Rerkshanandana P. Schlieren measurement of turbulent structure in a diffusion flame. *Experimental Thermal and Fluid Science*, (1993); vol. 6, pp. 402-416.
[27] Kolhe P.S., Agrawal A. K. Investigation of the crossbeam correlation algorithm to reconstruct local field statistics from line-of-sight measurements in turbulent flows. *Flow Turbul Combust.*, (2010) vol. 84, pp. 617-638.
[28] Panchapakesan N. R. and Lumley J. L. Turbulent measurements in axisymmetric jets of air and helium. Part 2 Helium jet. *J. Fluid Mech.*, **246** (1993) 225-247.
[29] Al-Ammar, K. N., Agrawal, A. K., Gollahalli, S. R. & Griffin D. Application of rainbow schlieren deflectometry for concentration measurements in an axisymmetric helium jet. *Exp Fluid*, **25** (1998) 89-95.

Spring Technical Meeting
of the Central States Section of the Combustion Institute
April 22–24, 2012

Ultra High-Speed Rainbow Schlieren Deflectometry For Turbulence Measurements in Jets and Flames

P.S. Kolhe and A. K. Agrawal

Department of Mechanical Aerospace Engineering, the University of Alabama, Tuscaloosa, Alabama 35487-0276, USA

Rainbow schlieren deflectometry (RSD) integrated with ultra high-speed imaging system is used to characterize turbulence in helium jet. The experimental system consists of a turbulent helium jet in air probed by rainbow schlieren deflectometry technique to acquire deflectometric data. Helium is discharged vertically into ambient air from a round tube injector of 3.65 mm diameter and jet inlet Reynolds number of 4000. Rainbow schlieren apparatus was configured to cover the near field axial range of 0 to 20 diameters downstream of injector exit at pixel resolution of 300 μm, image acquisition rate of 210,000 frames per second, and image exposure time of 4.7 μs to capture a wide range of turbulent structures. These deflectometric measurements are utilized along with spectral analysis algorithm (SAA) for reconstruction of statistics of local scalar field (helium mole fraction) and theoretical framework for cross-correlation based approach for velocity estimation is presented. Non-intrusive nature of RSD application allows probing the near field region of injector exit to characterize turbulence. Helium concentration statistics shows that flow mixing and energy cascading result into decreased gradients at downstream locations yielding lower peak mean and variance with increased radial extent. Ultra highs-peed imaging integration with RSD looks interesting approach to gain critical velocity field information to complete statistical characterization of turbulence through scalar and velocity measurements.

1. Introduction

Mixing of two or more fluids in turbulent flows is an important problem for non-reacting and reacting flow systems. Prediction, design and control of such systems require accurate turbulence models validated using experimental measurements. An important subset of turbulent flows is the axisymmetric binary gas mixing process used as the foundation to develop comprehensive theories of turbulent mixing involving multiple fluids in complex geometries. Several studies of turbulent binary gas mixing in the literature have reported detailed scalar measurements using intrusive techniques such as hot-wire anemometry and interference probes, and optical techniques such as laser induced fluorescence, Rayleigh scattering, and schlieren deflectometry.

Papanicolaou and List [1] carried out comprehensive set of velocity and concentration measurements using laser Doppler anemometry and laser induced fluorescence. Pitts and co-workers have extensively used Rayleigh light scattering, a non-intrusive optical technique [2-5]. They have reported detailed concentration measurements in axisymmetric free turbulent jets to describe the self-similarity behavior of several jet fluids. Panchapakesan and Lumley [6] used Way-interference probe to investigate turbulent helium jet mixing in air at downstream axial locations ranging from 50 to 120 jet diameter (d) downstream of the nozzle exit. They reported the approximate budgets for the turbulent kinetic energy, scalar variance, and scalar fluxes to aid

in the development of numerical model, since these terms are involved in Reynolds averaged Navier-Stokes equations. Shabbir and George [7] used three-wire (x-wire and cold wire) probes and determined the budgets of mean momentum and energy differentials. Recently, Schefer et al [8] used laser based Rayleigh scattering technique to analyze the self-similarity behavior of the concentration field in a hydrogen jet simulating the accidental leak from compressed storage tanks.

Scalar measurements in fluid flows have also been acquired using path-integrated measurement techniques such as interferometry and schlieren deflectometry. In this case, a deconvolution technique is required to obtain the local scalar field measurements. Stella et al [9] used shearing interferometry to measure temperature field in axisymmetric laminar flames. Al-Ammar et al [10] used the Rainbow schlieren deflectometry (RSD) technique to obtain the concentration field in an axisymmetric laminar helium jet. Agrawal et al [11] used the RSD technique to obtain temperature and oxygen concentration fields in laminar gas jet diffusion flames.

Statistics of scalar fields in turbulent flows have also been obtained using path-integrated techniques. Uberoi and Kovasznay [12] used the shadow method to analyze density fluctuations in the wake region of a supersonic projectile. Assuming homogeneity and isotropy of the flow field they estimated correlation function and power spectrum of 3D turbulent density field. Erbeck and Merzkirch [13] used speckle photography to develop integral transform relationships between correlations of ray deflection angle and local density correlations in a quadratic grid generated turbulent density field. Winarto and Davis [14] used mean square deflections and the cross correlation of angular deflections of two orthogonal laser beams to obtain local distributions of turbulent intensity and integral length scale in a supersonic air jet. Kalghatgi et al. [15] used a similar technique to measure the RMS density fluctuation and RMS density gradient fluctuation across an exhaust plume. Davis and co-workers [16-20] have used this laser schlieren approach to measure the covariance of the angular deflections, related to the local flow properties. Davis and Rerkshanandana [18-20] extended their previous studies to obtain the flow convection velocities and power spectra in turbulent diffusion flames and to delineate the influence of turbulent eddies on thermal mixing. Measurements in all of these studies were obtained by traversing the flow field point by point. Pellicia-Kraft and Watt [21] used multiple beam shearing interferometry to obtain 3D density field in a turbulent helium-argon jet.

Recently, Kolhe and Agrawal [22] demonstrated that the high-speed RSD technique can be used for simultaneous whole-field measurements in turbulent flows. They visualized small scale structures to capture a hitherto unknown secondary instability in transitional gas jet diffusion flames. Kolhe and Agrawal [23] proposed an amendment for the crossbeam technique [16-20] to improve the reconstruction accuracy and extended the algorithm to low Reynolds number flows. Recently, based on a quantitative evaluation of different reconstruction techniques, Kolhe and Agrawal [24] proposed the Spectral Analysis Algorithm (SAA) to obtain the local scalar field statistics in axisymmetric turbulent flows using the line–of-sight deflection angle measurements. Synthetic turbulence data were used to demonstrate the excellent reconstruction accuracy of the SAA [24]. The objective of the present study is to apply the SAA to obtain local scalar measurements and explore schlieren image velocimetry concept with capability of ultra high-speed RSD imaging technique.

2. Experimental Setup

Figure 1 shows the schematic diagram of the experimental setup. The flow system consists of compressed gas cylinder to supply helium, a mass flow meter (Aalborg GFM37 with range 0-100 standard liters per minute or slpm), a needle valve to control the helium flow rate, and 50 mm long tube injector with wall thickness of 0.5 mm and inner diameter, d = 3.65mm. The flow at the tube exit is expected to be nearly fully-developed. Helium is discharged vertically into the quiescent air environment kept at ambient conditions. Helium volume flow rate is kept constant at 73 slpm. The jet exit Reynolds number $\left(\mathrm{Re} = \rho \cdot V \cdot d / \mu\right)$ is 4000 and the jet exit Richardson number $\left(Ri = \frac{g \cdot d}{V^2} \cdot \left(\frac{\rho_{air} - \rho_{He}}{\rho_{He}} \right) \right)$ is 1.52×10^{-5}. Thus, the jet exit flow is considered as momentum-dominated. At ambient conditions, the Schimdt number $\left(Sc = \nu / D_0\right)$ is 1.7 for helium air jet indicating viscous diffusion and molecular mass diffusion effects are comparable. However, the turbulent Schmidt number reported in literature for turbulent helium-air jet (at jet exit Re ≈ 4000) is 0.7 as evaluated by Panchapakesan and Lumley [6] using eddy viscosity and diffusivities.

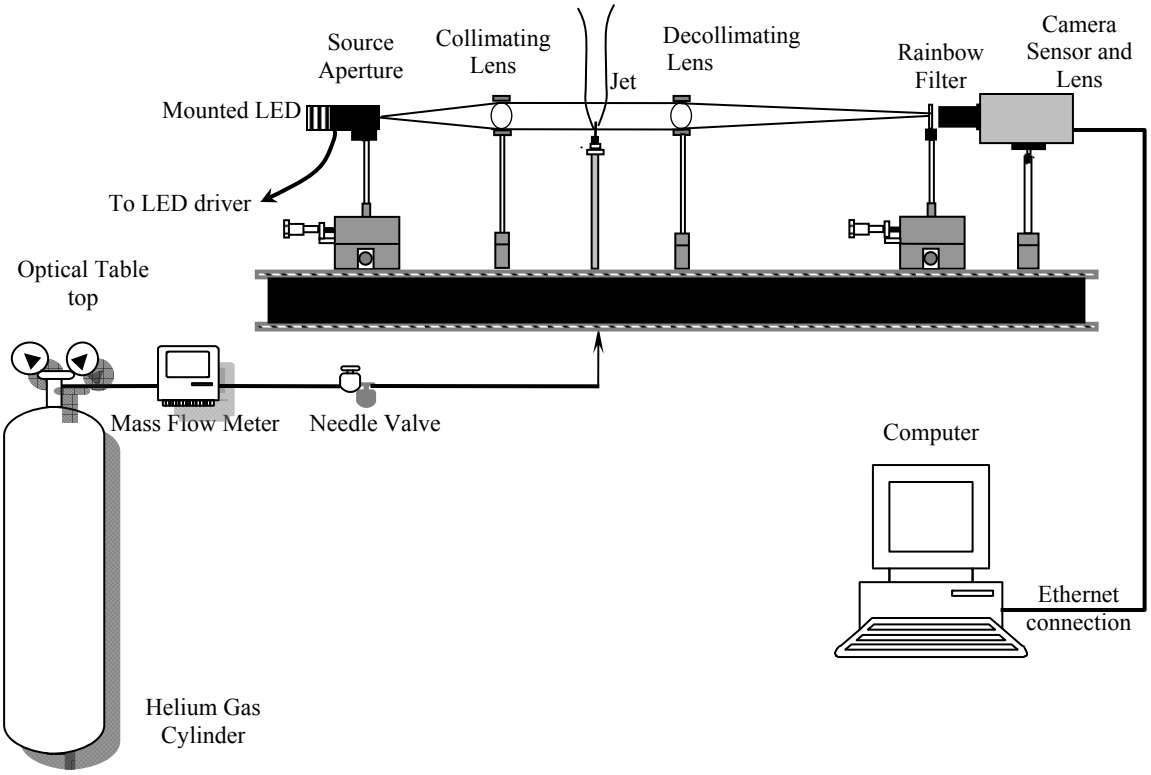

Figure 1: Schematic of experimental setup.

High-speed RSD system facilitates simultaneous whole-field measurements at 210,000 Hz with image pixel resolution of 120x192 with 300μm/pixel spatial resolution of field of view. Schlieren system consists of the light source aperture, collimating and decollimating lenses, a rainbow filter, and a digital color camera (ultra high-speed Photron SA-5). Light to the rectangular source aperture (50 μm wide and 3 mm high) is supplied by a 650 mW mounted LED with 1200 mA LED driver from Thor labs. The light source aperture is placed at the focal

point of the collimating lens (82 mm diameter and 300 mm focal length) to obtain parallel beams that pass through the test medium causing refraction. The refracted rays are refocused to form the source image at the focal point of the decollimating lens (76.2 mm diameter and 750 mm focal length) where the rainbow filter is placed. The filtered images are acquired by high-speed digital camera with 50 mm focal length lens. Each schlieren system is aligned to ensure precise alignment of the optical axis of all of the components. The camera onboard memory allows acquiring 248,370 schlieren images continuously at 210,000 frames per second. In the present study, 248,000 images in tiff file format are used to obtain time-averaged statistics of deflectometric data.

The RSD technique employs a continuously graded color filter to measure the deflection angle of light rays passing through the test medium [10]. Visible white light consists of multiple wavelengths or colors. The rainbow filter serves as a continuously graded filter since it transmits light of a particular wavelength (or color) corresponding to the location on the filter. This color-coding scheme facilitates computation of lateral (or axial) displacement of light rays at the filter plane corresponding to each pixel location in the color schlieren image. However, a priori knowledge of color distribution in the rainbow filter is required. The rainbow filter is sensitive only to the transverse displacements if the source aperture and color strips on the filter are aligned with the axial direction, and vice versa. In this study, the source aperture and color strips on the rainbow filter were oriented to detect the ray displacements in the transverse direction only.

In the RSD technique, hue, saturation, and intensity (HSI) color model is used to characterize the color by a single attribute, hue. Figure 2 shows the filter calibration curve expressed in terms of hue versus transverse location on the filter plane. The calibration curve is obtained by computing the average hue of the color schlieren image acquired without the test medium (background schlieren image) while the rainbow filter is traversed from edge to edge in increments of 50 μm. Schlieren images without and with the test medium are acquired without disturbing the optical system or the experimental setup. This practice ensures that a given pixel in the schlieren image maps the same physical location without or with the test medium.

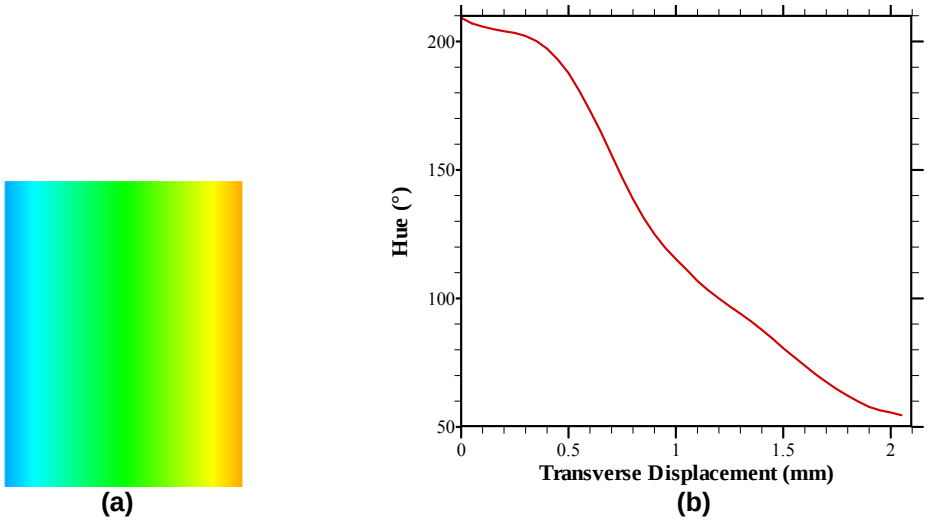

Figure 2: Rainbow filter and hue calibration curve.

3. Data Analysis

In the analysis procedure, the measured hue (H) at each pixel location in the schlieren image is converted to the transverse position on the filter plane (χ) using the filter calibration curve and Equation 1.

$$\chi(H) = \chi_i + \frac{\chi_{i+1} - \chi_i}{H_{i+1} - H_i} \cdot (H - H_i) \tag{1}$$

where (χ_i, H_i) and (χ_{i+1}, H_{i+1}) are filter calibration coordinates closest to the measured hue, H. Next, the transverse deflection angle of the light ray is found from Equation 2.

$$\Theta = \frac{\chi(H) - \chi(H_b)}{f} \tag{2}$$

where, $\chi(H_b)$ is the transverse filter position pertaining to the background hue, H_b and f is focal length of decollimating lens (f = 750 mm). Note that filter calibration curves are used together with Equations 1 and 2 to obtain transverse deflection angles at each pixel location of instantaneous schlieren images acquired by the two orthogonal systems.

Next, the spectral analysis algorithm given by Kolhe and Agrawal [24] is used to obtain the distributions of local mean and variance of refractive index difference. Spectral analysis algorithm utilizes the total energy content of path-integrated signal (e.g., ray deflection angle) in time and Fourier domains to obtain the mean and variance of refractive index difference. For time-averaged axisymmetric flows, this link is established through Abel inverse transform used to obtain the mixing function defined as the product of variance and integral length scale of the refractive index difference. Autocorrelation function is used to estimate the integral length scale, and thus, to deconvolute variance from the mixing function of the refractive index difference. Note that the SAA can be used with the line-of-sight measurements obtained by techniques such as speckle photography, shadow method or background oriented schlieren method with minor or no adaptation necessary. To obtain helium concentration statistics from refractive index difference statistic following procedure is utilized.

The jet flow is considered as binary mixture of helium and air. Therefore, the mean and variance of the refractive index difference is related to the mean and variance of helium mole fraction using the Gladstone-Dale equation for a mixture given as:

$$\delta = \left\{ \frac{1}{n_0} \cdot \left[\frac{P}{\overline{R}T} \cdot \left(k_{He} \cdot M_{He} - k_{air} \cdot M_{air} \right) \right] \right\} \cdot X_{He} \tag{3}$$

In Equation 3, P is the pressure, T is the temperature, $\overline{R}$ is universal gas constant, κ is Gladstone Dale constant, and M is molecular weight of the species or constituent, n_0 is refractive index of surrounding air. δ is the normalized refractive index difference defined as $\delta = (n - n_0)/n_0$ where n is the refractive index at a point in the test medium. The Gladstone-Dale constant for helium and air is, respectively, 1.96×10^{-4} and 2.274×10^{-4} m^3/kg [25]. The linear relationship in Equation 3 is used to obtain linear relationships between means and variances of helium mole fraction and refractive index difference as follows:

$$\overline{\delta} = \left\{ \frac{1}{n_0} \cdot \left[\frac{P}{\overline{RT}} \cdot \left(k_{He} \cdot M_{He} - k_{air} \cdot M_{air} \right) \right] \right\} \cdot \overline{X}_{He} \tag{4a}$$

$$\overline{\delta'^2} = \left\{ \frac{1}{n_0} \cdot \left[\frac{P}{\overline{RT}} \cdot \left(k_{He} \cdot M_{He} - k_{air} \cdot M_{air} \right) \right] \right\}^2 \cdot \overline{X'^2_{He}} \tag{4b}$$

Thus, the mean ($\overline{X}_{He}$) and variance ($\overline{X'^2_{He}}$) of helium mole fraction can be obtained from Equation 4 using the mean ($\overline{\delta}$) and variance ($\overline{\delta'^2}$) of refractive index difference determined by the SAA.

4. Scalar Measurements

Experiments were conducted by traversing tube injector in upstream direction to obtain near schlieren measurements in near field for 0-20 diameters downstream of injector exit. Note that, high speed imaging at 210,000 frames/sec limits the pixel resolution available to visualize the field of view. Figure 1 shows the instantaneous schlieren images along with spatial and temporal sample signal of instantaneous deflections. From Figure 1, it is evident that the imaging settings allow flow field visualization of 37mm x 59 mm size. From Figure 1(b) and 1(c), asymmetry and randomness in path-integrated measurements (deflection angle) on instantaneous basis is evident.

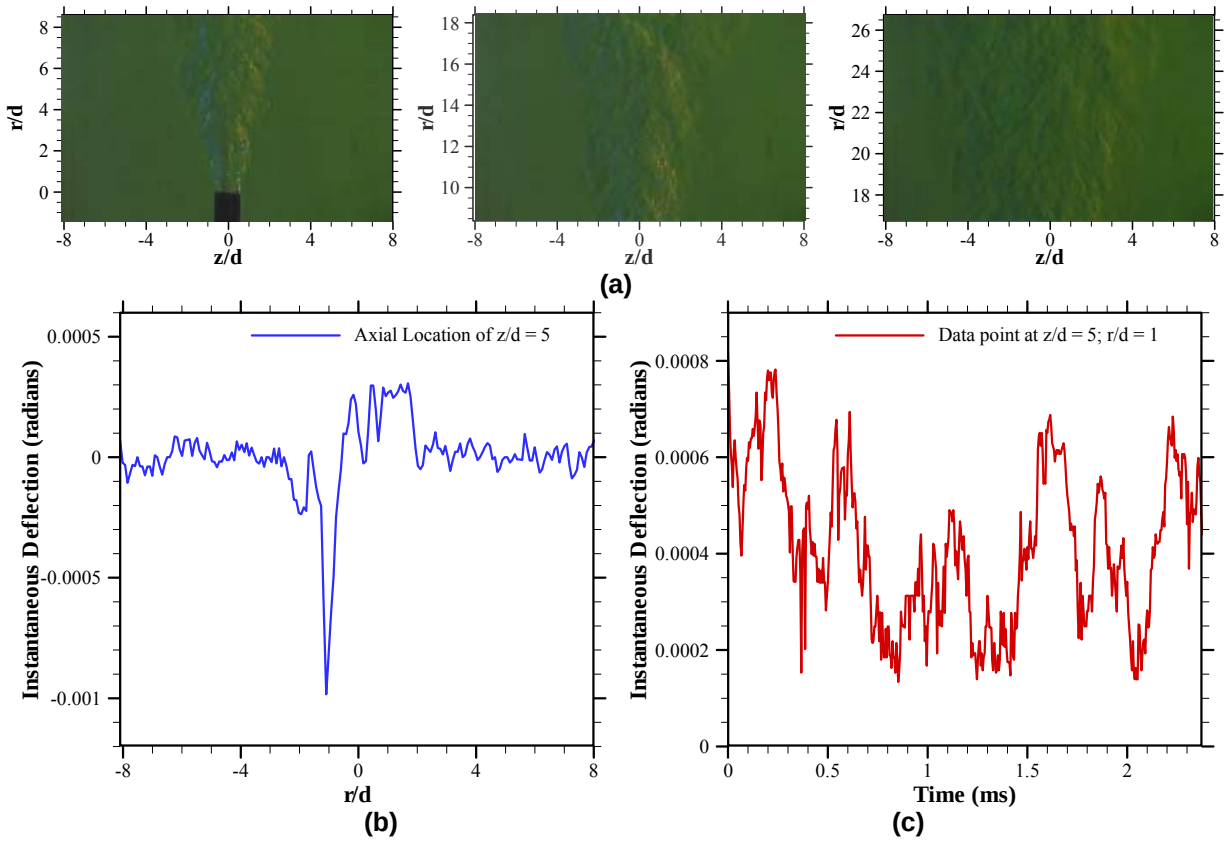

Figure 3: (a) Instantaneous schlieren images for different downstream location field of view and (b) spatial profile and (c) temporal evolution at axial location of z/d = 5.

Note that for turbulent flows use of asymmetric filter is necessary to detect both +ve and –ve deflections. However, LED light source characteristics alters the color sensitivity characteristics of schlieren imaging system limiting the usable hue variation on rainbow filter. From filter calibration curve in Figure 2, it is evident that for present experiments usable range is limited to 55° to 200° instead of 0°-360°.

To obtain the statistics of transverse deflection angle, 248,000 images captured at 210,000 frames/sec rate were used. Figure 4(a) and 4(d) show the mean transverse deflection angle distribution and radial profiles at selected few selected axial locations of z/d = 5, 10, 15 and 20. Maximum magnitude of mean transverse deflection angle is observed to be around 4e-4 radians. From Figure 4(a), it is seen that time averaged deflection angle magnitudes show symmetry with respect to jet centerline even though on instantaneous basis asymmetry and randomness prevails. The peak mean deflection at downstream location is observed to decrease, indicating reduction in scalar gradients at downstream locations due to flow mixing and energy cascading. The increase in radial extent of the mean deflection angle profile is observed at downstream locations as expected due to jet spreading and mixing.

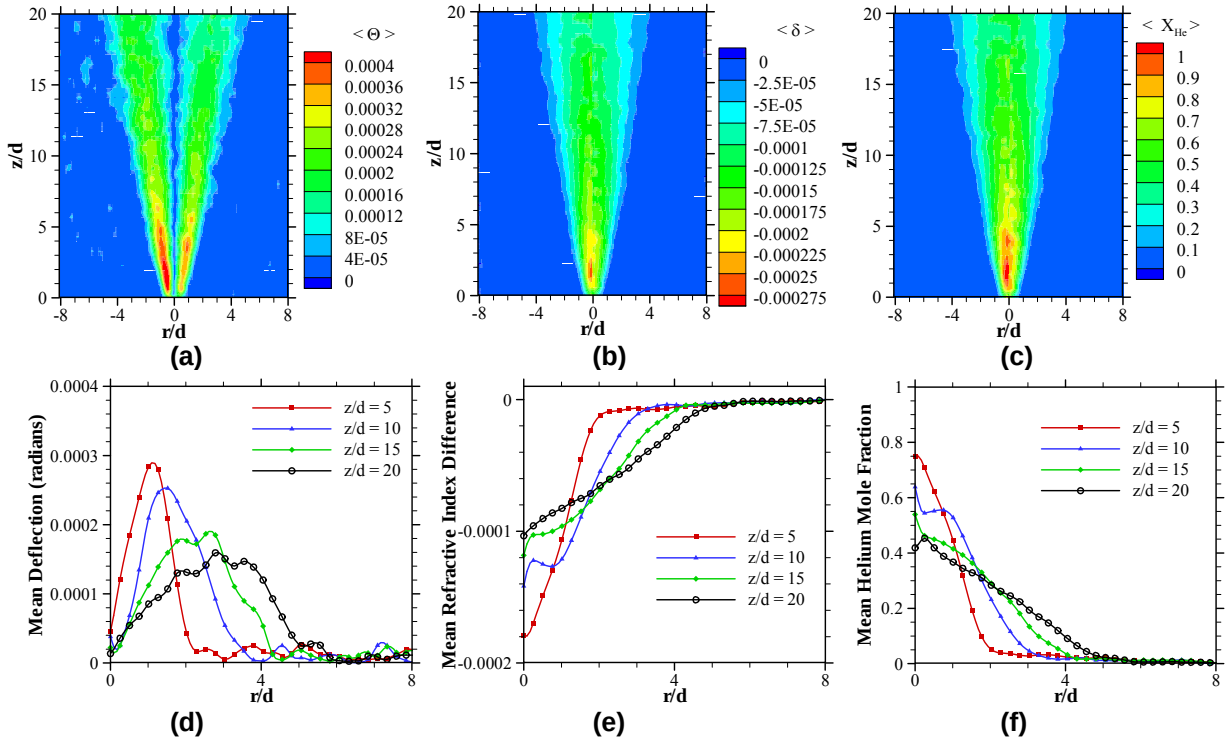

Figure 4: Statistical reconstruction of time averaged local scalar field.
Contour plots for (a) deflection angle, (b) reactive index difference, (c) helium mole fraction; and radial profiles of (d) deflection angle, (e) refractive index difference, and (f) helium mole fraction.

Time averaged axisymmetry allows use of Abel inverse transform on mean deflection angle to estimate mean refractive index difference field (δ), which in turn gives mean helium concentration field (X_{He}) using Equation (4a) {see reference 10 and 24 for further details}. Figure 4(b) and 4(e) shows the contour plots and radial profiles of mean refractive index difference respectively. Abel inversion formula was employed separately on each side of the jet center to obtain these contour plots. This would explain the minor deviation from symmetry in

the contour plots in Figure 4(b). Further, the uncertainty in jet center point location would lead to steeper gradients (or kinks) in reconstructed profiles. Results show that the mean refractive index difference is minimum at the jet center and it increases asymptotically in the radial direction to reach the ambient value at r/d ≈ 6.0. With increasing axial distance, the mean refractive index difference decreases for r/d < 2.0 and increases for r/d > 2.0 indicating improved mixing at downstream locations. Figure 4(c) and 4(f) show the contour plots and radial profiles of the mean helium mole fraction respectively. The mean helium mole fraction is maximum at the jet center and it decreases with the radial coordinate until the ambient condition of zero helium (or pure air) is reached. With the increasing axial distance, the jet spreads in the radial direction and the mean helium mole fraction at the jet center decreases. Between z/d = 5 and 20, the peak mean helium mole fraction decreases from 0.75 to 0.45 and the jet radial boundary changes from r/d = 4.4 to r/d = 6.0. Radial profiles of helium mole fraction are becoming increasingly flat at downstream locations, signifying that the region probed represents transitional flow regime where turbulence is not yet fully developed.

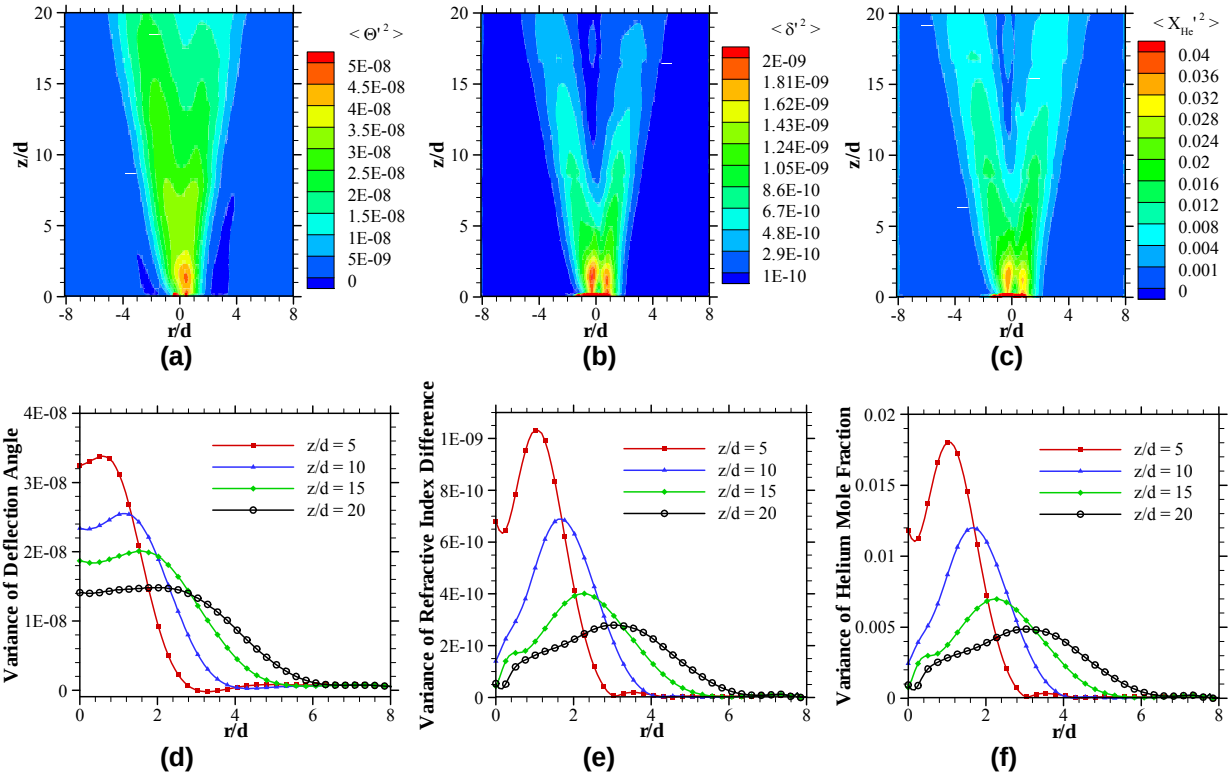

Figure 5: Statistical reconstruction of local scalar field fluctuation intensity (variance). Contour plots for (a) deflection angle, (b) reactive index difference, and (c) helium mole fraction. Radial profiles of (d) deflection angle, (e) refractive index difference, and (f) helium mole fraction.

Figure 5(a) and 5(d) show the variance of transverse deflection angle distribution and radial profiles at selected few selected axial locations of z/d = 5, 10, 15 and 20. Maximum magnitude of fluctuation intensity (variance) of transverse deflection angle is observed to be around 5e-8 sq. radians. From Figure 5(a), it is seen that time averaged second moment statistics of deflection angle shows symmetry with respect to jet centerline even though on instantaneous basis asymmetry and randomness prevails. The peak fluctuation intensity of deflection angle at downstream location is observed to decrease, corroborating observation of reduction in scalar

gradients at downstream locations based on mean deflection angle measurements. Spectral analysis algorithm [24], takes transverse deflection angle data to estimate fluctuation intensity of refractive index difference, which is used to estimate concentration fluctuation intensity using Equation (4b). Figure 5(b) and 5(e) show contour plots and radial profiles of the variance of refractive index difference. Results show the radial spreading of the variance profile with the axial distance. It is observed that variance peak shifts to radially outward direction with gradual reduction at downstream locations. The variance peaks at around r/d = 2, and the peak value decreases at downstream locations. These peak fluctuation intensity locations for local field (refractive index difference) are located radially outwards compared to peak fluctuation intensity in path integrated data (deflection angle). Figure 5(c) and (f) show the contour plots and the radial profiles of the variance of helium mole fraction. The peak variance and hence, the turbulent fluctuation intensity of helium mole fraction decreases with the axial distance. This result can be explained by energy cascading whereby the larger eddies break down into smaller eddies at the downstream locations in a turbulent flow. The reconstruction of helium concentration fluctuation intensity near jet centerline has higher uncertainty and shows unrealistic kinks due to indecisiveness in jet center location at downstream locations. It is evident from Figure 4(a) and Figure 5(a) that the jet centerline for mean and variance of deflection angle is not matching exactly.

5. Velocity Measurement Concept

Statistical correlations indicate similarity in the two signals whether be it spatial or temporal signal. Hence, spatial correlation can be used to find convection velocity of the structures through identification of similarity between the two structures separated in space as well as time. Similarly, temporal correlations between specified two locations would yield the time lag for peak two-point correlation to estimate convection velocity of structures. Shortcomings of the two approaches are: (1) pattern matching through spatial correlations requires structure maintains its characteristics irrespective of the path followed, and time elapsed, and (2) temporal correlations yield resultant velocity for structure to travel between the two locations under consideration as actual path followed would not be accounted for while estimating the convection velocity.

Spatial correlation between $f(x_1,y_1)$ and $g(x_2,y_2)$ computed using Equation (5) as given below,

$$C = \frac{\sum_{x_1}\sum_{y_1}\sum_{x_2}\sum_{y_2}\left(f(x_1,y_1)-\bar{f}\right)\cdot\left(g(x_2,y_2)-\bar{g}\right)}{\sqrt{\sum_{x_1}\sum_{y_1}\left[\left(f(x_1,y_1)-\bar{f}\right)\right]^2\cdot\sum_{x_2}\sum_{y_2}\left[\left(g(x_1,y_1)-\bar{g}\right)\right]^2}} \tag{5}$$

where, $\bar{f}$ and $\bar{g}$ are spatial means of $f(x_1,y_1)$ and $g(x_2,y_2)$. Note that correlation magnitude ranges between +1 and -1. If $f(x_1,y_1)$ and $g(x_2,y_2)$, represent same structure separated in time at two different places, then the spatial correlation identification would yield the velocity of convection between the two spatial locations under consideration. Endeavor is made to develop optimized algorithm for pattern matching based on the spatial correlations. To validate the concept, Matlab program was developed to generate synthetic schlieren images with predefined number of structures with their characteristics and offsets in a set of six images shown in Figure 6. Figure 7 shows the streamlines traced by these structures using the spatial correlation concept utilizing normxcorr2 built-in Matlab function. Figure 7 results indicate the

spatial correlation based pattern matching algorithm works very well. However, in experimental results, unlike synthetic images might undergo changes structures leading to lower correlation values and uncertainty associated with its identification.

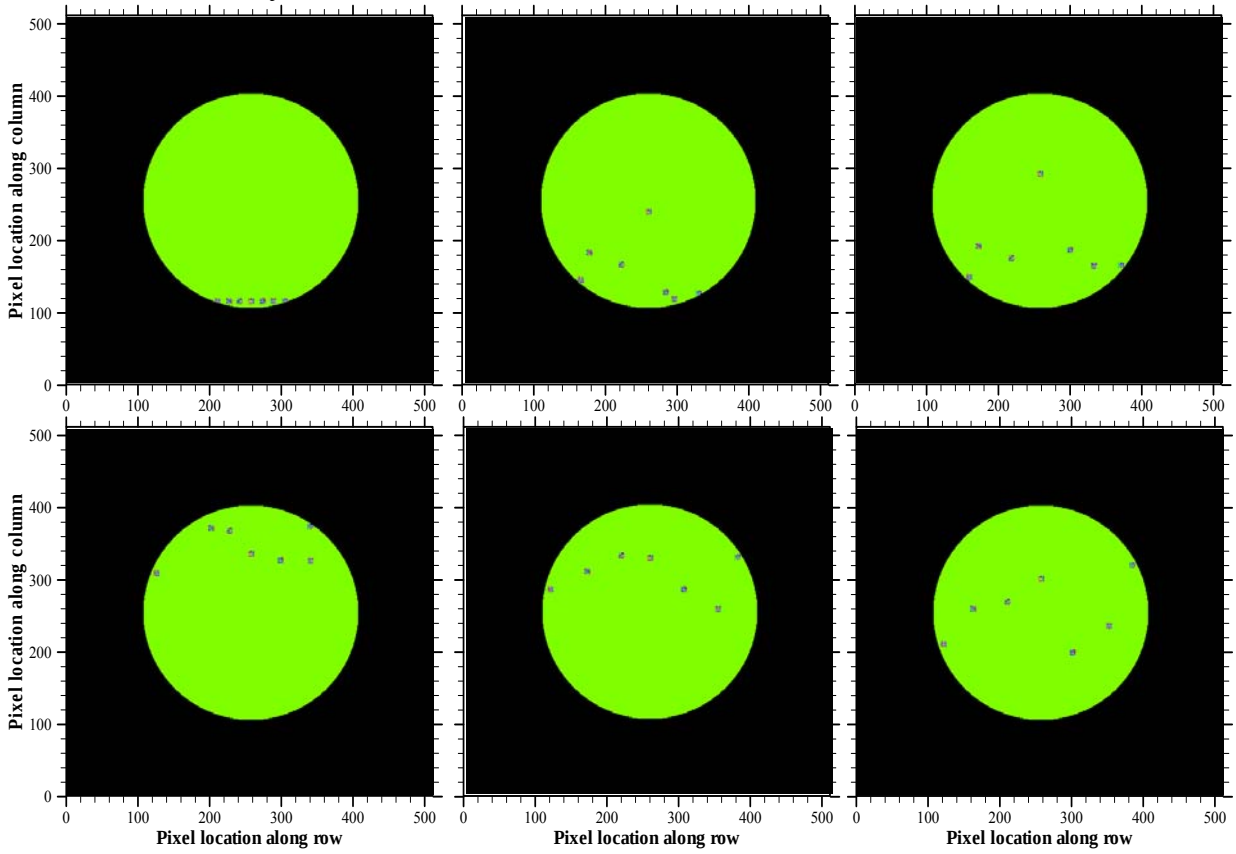

(b)

Figure 6: Synthetic schlieren images with predefined structures and offsets for validation of pattern matching algorithm based on spatial correlations.

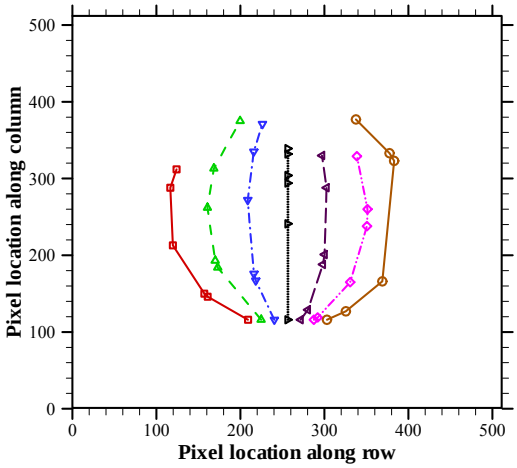

(b)

Figure 7: Streamline movement tracking by cross correlation.

6. Concluding Remarks

Scalar turbulence measurements in a momentum-dominated turbulent helium jet are obtained using the rainbow schlieren deflectometry technique combined with the spectral analysis algorithm. Measurements are obtained at spatial resolution of 300 μm, image sampling rate of 210000 Hz, and image exposure time of 4.76 μs. The turbulent flow is characterized by mean and variance of helium concentration across the whole field of view. Experiments indicate that ultra highspeed imaging is promising and allows carrying out scalar measurements without any adverse impact on the sensitivity or accuracy of measurements. The schlieren apparatus used in this study is relatively inexpensive compared to existing laser-based techniques. Spectral analysis algorithm can be applied to line-of-sight measurements acquired by techniques such as schlieren deflectometry, speckle photography, background oriented schlieren, and shadowgraphy. Ultra high-speed imaging lends RSD capability to do velocity measurements alongwith scalar measurements, making it a complete tool to characterize turbulence non-intrusively even in the near field region of z/d = 0 to 20. Spatial correlation based algorithm for velocity estimation is conceptually evaluated. Future work would involve the development of optimized search algorithm accompanied with spatial correlation concept to allow velocity measurement with presence of strong velocity gradients.

Acknowledgement

This research was supported in part by the Physical Sciences Division of NASA's Office of Biological and Physical research under grant NNC04GA22G.

References

[1] Papanicolaou p. and List E. J. *J. Fluid Mech.*, **195** (1988) 341-391.
[2] Pitts W. M., and Kashiwagi T. *J. Fluid Mech.*, **141** (1984) 391-429.
[3] Bryner N., Richards C. D., and Pitts W. M., *Rev. Sci. Instrum.*, **63** (7) (1992) 3629-3635.
[4] Pitts W. M. *Exp. Fluid*, **11** (1991) 135-141.
[5] Richards C. D. and Pitts W. M. *J. Fluid Mech.*, **254** (1993) 417-435.
[6] Panchapakesan N. R. and Lumley J. L. *J. Fluid Mech.*, **246** (1993) 225-247.
[7] Shabbir A. and George W. K. *J. Fluid Mech.*, **275** (1994) 1-32.
[8] Schefer, R.W., Houf, W.G., & Williams, T.C. *International Journal of Hydrogen Energy*, **33** (2008) 6373-6384.
[9] Stella, A., Guj G., & Giammartini S. *Exp Fluid*, **29** (2000) 1-12.
[10] Al-Ammar, K. N., Agrawal, A. K., Gollahalli, S. R. & Griffin DeVon, *Exp Fluid*, **25** (1998) 89-95.
[11] Agrawal, A. K., Al-Ammar, K. N., & Gollahalli, S. R, *Exp Fluid*, **32** (2002) 689-691.
[12] Uberoi M.S. and Kovasznay L.S.G. *J. Appl. Phys.*, **26** (1955) 19-24.
[13] Erbeck, R., and Merzkirch, W. *Exp. Fluids*, **6** (1988) 89-93.
[14] Winarto, H., & Davis M.R. *Proc. R. Soc. A*, ***395*** (1984) 203-228.
[15] Kalghatgi, G.T., Cousins, J.M., & Bray, K.N.C., *Combust. flame*, ***43*** (1981) 51-67.
[16] Davis M. R., *J. Fluid Mech.*, ***70*** (1975) 463-479.
[17] Davis M.R., *Combust. Sci. Tech.*, ***64*** (1989) 51-65.
[18] Davis, M.R. & Rerkshanandana, P., *Int. J. Heat and Mass Transfer*, ***34***(7) (1991) 1633-1647.
[19] Davis, M.R. & Rerkshanandana, P., *Exp. Therm. Fluid Sci.*, ***6*** (1993) 402-416.
[20] Davis, M. R. & Rerkshanandana, P., *Exp. Therm. Fluid Sci.*, ***8*** (1994) 239-244.
[21] Pellicia-Kraft, B. J., & Watt, D. W. *Exp Fluid*, **29** (2000) 573-581.
[22] Kolhe P. S., Agrawal A. K., *Flow Turbul. Combust.*, **79** (2007) 343–360. DOI: 10.1007/s10494-007-9098-y.
[23] Kolhe P. S., Agrawal A. K. *Flow Turbul. Combust.* **84**(4) (2010) 617-638. DOI:10.1007/s10494-009-9244-9.
[24] Kolhe P. S., Agrawal A. K. *Meas. Sci. Tech.*, **20** (2009) 115402(10 pp) DOI:10.1088/0957-0233/20/11/115402.

[25] Merzkirch W. *Flow Visualization*, revised 2nd ed. Academic Press, Orlando, Florida, 1987.
[26] Thoroddsen, S. T. & Van Atta, C. W., *J. Fluid Mech.*, ***322*** (1996) 383-409.
[27] Miller P.L. and Dimotakis P.E. *Phys. Fluids A*, **3**(5) (1991) 1156-1163.